

ABSTRACT

CARLIN, CONRAD ZACHARY. MOCVD Growth and Modeling of Quantum-well Solar Cells and Tunnel Junctions. (Under the direction of Dr. Salah M. Bedair).

One source of photovoltaic energy is the multijunction (MJ) solar cell, which has given the highest efficiencies of any photovoltaic technology. Typical MJ devices are composed of several pn junctions with materials of differing band gaps. Ideally, each material is lattice matched and current match to each other, requiring the proper choice of semiconductor for each junction. The limited availability of semiconductors with these characteristics has in the past required the either the lattice matching or current matching be violated, reducing the maximum potential efficiency. For terrestrial applications, multijunction structure are cost efficient only when operated at high solar concentrations. One of the main limits to the solar concentration is the maximum current that can be supported by the tunnel junctions (TJ) between multijunction subcells.

Solar cells were grown by metal organic chemical vapor deposition based on a GaAs p-i-n structure with an i-layer containing low band gap InGaAs is grown as thin, compressively strained layers that are compensated with GaAsP layers under tensile strain. The resulting structure is lattice matched to the GaAs substrate and the InGaAs quantum wells (QW) absorb at a lower energy than the GaAs, lowering the effective band gap of the subcell. The bandgap of InGaAs wells were modeled using a modified Kronig-Penney model to include the effects of strain and quantum confinement. However, device external quantum efficiency (EQE) measurements showed that the actual QW absorption energy edge was higher than expected. It was found that this behavior could be modeled as a graded interface between the InGaAs and GaAsP layers. The effect of this grading was found to be strongest for the interface formed during the transition from GaAsP to InGaAs and the effects could be minimized by including a layer of GaAs between the two materials.

Each QW structure used $\text{GaAs}_{1-y}\text{P}_y$ with high phosphorus compositions ($x > 0.65$), requiring transport to occur through tunneling. For this reason reductions in EQE were observed for barriers thicker than 30 Å. These thick barrier devices were useful for investigating the transport through the QW structures. EQE measurement of p-i-n and n-i-p QW structures indicate that carrier transport through the i-layer was limited by electrons. An empirical model was developed to calculate the EQE of both GaAs pn and QW p-i-n devices. Both the tunneling and probability and lifetime were determined, making it possible to find the recombination lifetime in the wells. This was found to be 110 ns for $\text{In}_{0.15}\text{Ga}_{0.85}\text{As}$ and 25 ns for $\text{In}_{0.18}\text{Ga}_{0.82}\text{As}$, close to results found by time resolved photoluminescence.

For a Ge/GaAs/InGaP MJ cell the critical TJ is between the GaAs and InGaP subcells must have a band gap above 1.9 eV to avoid parasitic absorption. It was found that the performance of the n^{++} -InGaP/ p^{++} -AlGaAs TJ was greatly improved by growing a thin ($<50 \text{ \AA}$) GaAs layer at the InGaP-AlGaAs interface, with the peak tunneling current (J_{pk}) increasing from 18 A/cm^2 to $>1000 \text{ A/cm}^2$. The tunneling current has an exponential dependence on the tunneling width and effective mass, so it is very sensitive to doping and material composition near the junction. Neither direct tunneling nor trap assisted tunneling models could adequately explain the observed J_{pk} . However, the high J_{pk} can be explained by either the carryover of In into the GaAs to form InGaAs or by the formation of a highly doped layer at the InGaP-GaAs interface. The success of these models can be explained by the reduction of the tunneling width due to the presence of GaAs (or InGaAs) QW within the tunneling regions.

© Copyright 2015 Conrad Zachary Carlin

All Rights Reserved

MOCVD Growth and Modeling of Quantum-well Solar Cells and Tunnel Junctions

by
Conrad Zachary Carlin

A dissertation submitted to the Graduate Faculty of
North Carolina State University
in partial fulfillment of the
requirements for the degree of
Doctor of Philosophy

Electrical Engineering

Raleigh, North Carolina
2015

APPROVED BY:

Salah. M. Bedair
Committee Chair

Nadia El-Masry

Leda Lunardi

Robert Trew

BIOGRAPHY

Conrad Zachary Carlin was born on October 30, 1981 in Raleigh, North Carolina. His father, Clifford Million Carlin, Jr. and his mother, Lisa Johnston Carlin are both graduates of North Carolina State University with a Ph.D. in chemistry and an M.S in biology, respectively. After the completion of his father's degree, he lived in Austin, Texas; Orono, Maine and Charlotte, North Carolina. He graduated from Harding University High School in 2000 and from the University of North Carolina at Charlotte in 2005 with a B.S. in chemistry. His interests include reading, classical music and Carolina Panthers football. He has two younger brothers, Samuel Jefferson Carlin and Harry Liam Carlin.

ACKNOWLEDGMENTS

The author would like to thank his family for their support and Dr. John Hauser for his assistance with the tunnel junction modeling in Chapter 7.

TABLE OF CONTENTS

LIST OF TABLES	viii
LIST OF FIGURES	ix
1. Comparison of energy sources	1
1.1. Criteria for evaluating energy sources.....	2
1.2. Current energy sources	4
1.3. Future energy sources.....	6
1.4. The potential for photovoltaics.....	7
2. Basics of photovoltaics	9
2.1. Solar irradiance and the solar spectrum.....	9
2.2. Band structure and light absorption.....	10
2.2.1. Origin of band structure.....	10
2.2.2. Charge carriers.....	12
2.2.3. Generation and recombination.....	14
2.3. Fundamentals of pn junctions.....	16
2.3.1. Diode equation.....	16
2.3.2. Diode equation for photovoltaics	17
2.4. Photovoltaic principles	18
2.4.1. Short circuit current.....	18
2.4.2. Open circuit voltage	18
2.4.3. Fill factor	19
2.4.4. Quantum efficiency	19
2.4.5. Efficiency	19
2.4.6. Sources of loss and maximum efficiency	20
2.5. Components of photovoltaic devices.....	20
2.5.1. Emitter and Base.....	21
2.5.2. Window	21
2.5.3. Back surface field	21
2.5.4. Metal contacts.....	22
3. Multijunction photovoltaics, Quantum wells and superlattices, and tunnel junctions	23
3.1. Multijunction photovoltaics.....	23
3.1.1. Advantages and disadvantages of multijunction photovoltaics.....	23
3.1.2. Types of multijunction structures	26
3.1.3. Concentrator solar cells	28

3.2.	Quantum wells and superlattices	29
3.2.1.	Formation of quantum wells and superlattices	30
3.2.2.	Quantum size effect	31
3.2.3.	Strained quantum wells and strain balanced superlattices and their application to multijunction solar cells	32
3.3.	Tunnel junctions	34
3.3.1.	Origin of the tunnel junction	34
3.3.2.	Use of tunnel junctions in multijunction structures	36
4.	MOCVD and device and material characterization	37
4.1.	Metal organic chemical vapor deposition	37
4.1.1.	Components of MOCVD system	38
4.1.1.1.	Bubblers and gas sources	38
4.1.1.2.	Vent/run manifold	39
4.1.1.3.	Reactor	40
4.1.1.4.	Exhaust system	41
4.1.2.	Substrate preparation	41
4.1.3.	MOCVD growth	42
4.1.3.1.	Purge and bake out	42
4.1.3.2.	Nucleation	42
4.1.3.3.	Growth	43
4.2.	Device and material characterization	44
4.2.1.	Hall effect characterization	44
4.2.2.	X-ray diffraction	45
4.2.3.	Photoluminescence	46
4.2.4.	Light JV response	46
4.2.5.	External quantum efficiency	46
5.	Quantum well structures: Modeling and experiment	48
5.1.	Modeling of quantum well states	48
5.1.1.	Kronig-Penny model for superlattices	48
5.1.2.	Effect of strain on energy states in quantum wells	52
5.1.3.	Modified Kronig-Penny model for non-abrupt interfaces	55
5.1.4.	Effect of built-in electric field on energy states in quantum wells	61
5.1.5.	Constraints for quantum well structures: strain-balancing and carrier transport	62
5.1.5.1.	Critical layer thickness	62
5.1.5.2.	Strain balance	64

5.1.5.3.	Carrier transport.....	64
5.1.6.	Optimization of composition and thickness of strain-balanced quantum wells and barriers	65
5.2.	Extension of absorption in quantum well solar cell devices.....	67
5.2.1.	The p-GaAs/i-MQW/n-GaAs solar cell structure.....	68
5.2.2.	The effect of quantum well composition and thickness on absorption extension	69
5.2.3.	The addition of GaAs layers at InGaAs/GaAsP interfaces and the effect on interface grading	72
6.	Effect of barrier width on carrier transport	76
6.1.	Effect of barrier thickness on EQE.....	76
6.1.1.	Effect of device polarity: importance of electron transport.....	76
6.1.2.	Effect of temperature and bias on EQE	79
6.2.	Empirical model for EQE of solar cell devices.	80
6.2.1.	EQE for p-n GaAs structures.....	80
6.2.2.	Calculation of absorption in MQW structures.....	83
6.2.2.1.	Single-carrier absorption	83
6.2.2.2.	Excitonic absorption.....	84
6.2.3.	EQE of MQW solar cell structures.....	84
6.2.4.	Determination of recombination lifetime from EQE modeling.....	85
7.	InGaP/GaAs/AlGaAs tunnel junctions.....	90
7.1.	Growth of highly doped materials	90
7.1.1.	Te doping in InGaP	90
7.1.2.	Te doping in GaAs.....	91
7.1.3.	C doping in AlGaAs	92
7.2.	InGaP/AlGaAs tunnel junctions.....	93
7.3.	The addition of a GaAs interfacial layer to InGaP/AlGaAs tunnel junctions	94
7.3.1.	The effect of GaAs thickness.....	95
7.3.2.	Annealing of InGaP/GaAs/AlGaAs tunnel junctions	96
7.4.	Modeling of tunneling current.....	96
7.4.1.	Kane model.....	97
7.4.2.	Transfer matrix model	99
7.4.2.1.	Direct tunneling	99
7.4.2.2.	Resonant trap assisted tunneling.....	100
7.4.3.	Thermal diffusion of dopants and diffusion barriers	102
7.4.4.	Spike doping at InGaP/GaAs interface.....	105

7.4.5. Indium carryover from InGaP into GaAs	112
REFERENCES	118

LIST OF TABLES

Table 3.1: The ideal band gaps and maximum efficiency for 1, 2 and 3 junction PV cells at one sun and infinite sun concentration of the AM1.5D spectrum.	26
Table 4.1: Summary of metalorganic precursors used in this work.	39
Table 6.1: Calculated tunneling lifetime, transmission probability and recombination lifetime for various device polarities and GaAsP barrier thicknesses.	87
Table 7.1: Efficiency loss from absorption from GaAs in top tunnel junctions.	94
Table 7.2: Comparison between measured and calculated J_{pk} for various GaAs thicknesses using a direct tunneling model.	100

LIST OF FIGURES

Figure 1.1: Distribution of total energy use and renewable energy use by source. The red line highlights renewable energy sources. Photovoltaic and solar thermal energy generation are currently a small portion of both renewable energy use and total energy use.	1
Figure 2.1: Spectral irradiance for the AM0, AM1.5G and AM1.5D standard solar spectra as defined by ASTM.	10
Figure 2.2: Formation of the band structure. The (a) atomic electronic states for a carbon atom form (b) molecular states for the diatomic carbon and the number of quantum states is preserved. The transition from discrete molecules to the (c) periodic diamond structure results in the formation of bands rather than discrete molecular states.	11
Figure 2.3: Simplified band structure for a semiconductor. The valence band minimum is always at $k=0$ and for unstrained materials is composed of two degenerate bands, the light hole band and the heavy hole band. The conduction band minimum is shown to be at $k=0$, but it may be at $k \neq 0$ for other semiconductors.	13
Figure 2.4: Absorption coefficient of silicon and gallium arsenide as a function of photon energy. Since the GaAs is a direct band gap semiconductor, it has a much larger absorption coefficient at most energies.	15
Figure 2.5: Valence and conduction band structure for a typical pn junction.	16
Figure 2.6: J-V response of a photovoltaic cell in the dark (dark current) and under illumination (light current).	18
Figure 3.1: Three possible configurations for incorporating semiconductors of different band gaps into a photovoltaic system: (a) a heterojunction diode with different n-type and p-type materials (b) spatial separation of incoming radiation onto PV cells with different band gaps (c) a multijunction tandem cell with subcells connected materially, optically and electrically in series.	24
Figure 3.2: Plot of band gap versus lattice constant for several III-V semiconductors. The connecting lines represent ternary alloys with black lines for direct semiconductors and red for indirect semiconductors. The two vertical blue lines correspond to materials lattice matched to the common GaAs/Ge and InP substrates The composition dependent band gaps and lattice constants were found from [7].	25
Figure 3.3: Schematic of the lattice matched, metamorphic and inverted metamorphic triple junction PV cells showing typical band gaps for each of the three subcells.	27
Figure 3.4: Physical layout of three reduced dimension semiconductor structures: the quantum well, the quantum wire and the quantum dot. The superlattice is formed from a series of closely spaced quantum wells.	30
Figure 3.5: Demonstration of the quantum size effect in three $\text{In}_{0.15}\text{Ga}_{0.85}\text{As}$ quantum wells. The confined states for electrons and heavy holes are shown for each well, light hole states are omitted for simplicity. Thinner wells show more severe quantum size effects.	32
Figure 3.6: Demonstration of the strained superlattice concept with the substrate in green, the compressively strained material in orange and the tensilely strained material in blue.	

The distortion in the lattice constant for the strained layers in the plane of the substrate results in an opposite distortion in the perpendicular dimension.....	33
Figure 3.7: Tunnel diode mechanism: a) Degenerate doping in both the n and p sides creates a path for tunneling at low bias, b) as the bias increases direct tunneling becomes impossible and the current decreases to a minimum value and c) at a sufficiently large bias the junction behaves like a typical diode.....	35
Figure 4.1: Functional schematic of the Thomas Swan reactor.....	37
Figure 4.2: Photograph of the growth chamber attached to the MOCVD system.....	40
Figure 4.3: Schematics for the GaAs-SLS photovoltaic cell and the InGaP/AlGaAs tunnel junction.	44
Figure 5.1: Wavefunction of the lowest energy state of an electron in a) quantum well and b) superlattice	49
Figure 5.2: E-q dispersion of a 100 Å In _{0.15} Ga _{0.85} As/ 30 Å GaAs _{0.25} P _{0.75} superlattice (red) with the energy states of an equivalent isolated quantum well (black).....	51
Figure 5.3: Schematic showing the effect of compressive and tensile strain on the band structure around k=0	53
Figure 5.4: Effect of strain on the band gap of In _x Ga _{1-x} As for x<0.5	54
Figure 5.5: Effect of strain on the band gap of GaAs _{1-y} P _y for y>0.5. The minimum band gap is the X band of the conduction band for all compositions within the given range.	55
Figure 5.6: Calculated effective band gap for In _x Ga _{1-x} As/GaAs _{0.15} P _{0.85} superlattices showing larger effective band gaps as found from EQE measurements of p-i-n SLS devices.	56
Figure 5.7: Potential sources of effective band gap increase in superlattice structures. There are two modifications of the center well that could give a larger effective band gap: a lower indium fraction (left) and grading the in the P or In composition at interfaces (right).	57
Figure 5.8: Schematic of the conduction band envelope function for superlattices with a) abrupt and b) graded interfaces.	59
Figure 5.9: Effective band gap for In _x Ga _{1-x} As/GaAs _{0.15} P _{0.85} superlattices with and without grading at the InGaAs/GaAsP heterointerface.	61
Figure 5.10: Critical layer thickness for InGaAs and GaAsP on GaAs calculated using the model of Matthews and Blakeslee.	63
Figure 5.11: Effective band gap for an abrupt interface InGaAs/GaAsP SLS. The purple line is the CLT constraint for InGaAs and the solid orange line is the CLT constraint for GaAsP. The dotted orange lines are the 30 Å barrier thickness tunneling constraint for GaAs _{1-y} P _y ranging from y=0.65 to y=0.85.	66
Figure 5.12: Effective band gap for a 20 Å graded interface InGaAs/GaAsP SLS. The purple line is the CLT constraint for InGaAs and the solid orange line is the CLT constraint for GaAsP. The dotted orange lines are the 30 Å barrier thickness tunneling constraint for GaAs _{1-y} P _y ranging from y=0.65 to y=0.85.	67
Figure 5.13: Typical structure for a SLS p-i-n solar cell.....	68

Figure 5.14: EQE showing the extension of absorption due to $\text{In}_{0.17}\text{Ga}_{0.83}\text{As}$ and $\text{In}_{0.23}\text{Ga}_{0.77}\text{As}$ wells with 25\AA $\text{GaAs}_{0.25}\text{P}_{0.75}$ barriers.....	71
Figure 5.15: EQE showing the extension of absorption due to $\text{In}_{0.18}\text{Ga}_{0.83}\text{As}$ and $\text{In}_{0.15}\text{Ga}_{0.77}\text{As}$ wells with 30\AA $\text{GaAs}_{0.22}\text{P}_{0.78}$ barriers.....	72
Figure 5.16: PL response of superlattice showing the effect of increasing the GaAs thickness as both ternary/ternary interfaces.	74
Figure 5.17: EQE of $\text{In}_{0.18}\text{Ga}_{0.82}\text{As}/\text{GaAs}_{0.35}\text{P}_{0.65}$ superlattice devices with 25, 50 and 75 \AA GaAs buffer layers at the P→In interface.	75
Figure 6.1: J-V response for three solar cell devices: 1. A GaAs standard cell, 2. a device with an $\text{In}_{0.18}\text{Ga}_{0.82}\text{As}/\text{GaAs}_{0.21}\text{P}_{0.79}$ superlattice and 30 \AA barrier and 3. the same superlattice with 34 \AA barriers.	77
Figure 6.2: Standard, thin barrier and thick barrier solar cell devices with a) n on p polarity and $\text{In}_{0.18}\text{Ga}_{0.82}\text{As}/\text{GaAs}_{0.21}\text{P}_{0.79}$ superlattices and b) p on n polarity and $\text{In}_{0.15}\text{Ga}_{0.85}\text{As}/\text{GaAs}_{0.20}\text{P}_{0.80}$ superlattices.	78
Figure 6.3: EQE of n on p thick barrier superlattice devices as a function of (a) device temperature and (b) reverse bias. Both higher temperatures and larger reverse bias increase the EQE above 600 nm due to an improvement in carrier transport.....	80
Figure 6.4: Experimental and modeled EQE for a GaAs with a) an n on p polarity and b) a p on n polarity. Also shown are the contributions to the EQE from the emitter, base and depletion region.	85
Figure 6.5: The modeled and measured EQE for thick barrier devices with a) an n on p polarity and b) a p on n polarity. The EQE contributions from the base, emitter and SLS layers are included. P_{tot} was adjusted to give the best fit to the measured EQE.	87
Figure 6.6: Modeled and measured EQEs for the n on p thick barrier device at several temperatures. The value of P_{tot} increases with increasing temperature and is near 1 at 107 °C.	89
Figure 7.1: Hall n-type doping versus DETe flow for GaAs.....	91
Figure 7.2: Hall p-type doping and growth rate versus CBr_4 flow for AlGaAs	92
Figure 7.3: J-V response of an InGaP/AlGaAs tunnel diode	94
Figure 7.4: Peak tunneling current for an n-InGaP/n-GaAs/p-AlGaAs TJ for several GaAs thicknesses	95
Figure 7.5: InGaP/GaAs/InGaP with the quantum well model for a single trap state.....	101
Figure 7.6: Modeled J-V response for a TJ with direct tunneling and TAT for traps with densities of 10^{15} cm^{-3} and 10^{19} cm^{-3}	102
Figure 7.7: Peak current for an annealed InGaP/AlAs/AlGaAs TJ as a function of the AlAs diffusion barrier thickness.....	104
Figure 7.8: Peak current density as a function of InGaP thickness for annealed InGaP/AlGaAs tunnel junctions.....	105
Figure 7.9: Peak current density versus spike doping for various thicknesses of the spike layer in InGaP	106
Figure 7.10: Peak current density versus spike doping for various thicknesses of spike doping in GaAs	107

Figure 7.11: Peak current density versus spike doping for various GaAs thicknesses.....	108
Figure 7.12: Peak current density versus spike doping for various doping levels in GaAs	109
Figure 7.13: Peak current density versus GaAs doping for various GaAs thicknesses and a 4.8×10 ¹⁹ cm ⁻³ InGaP doping spike.	110
Figure 7.14: Band profile for InGaP/GaAs/AlGaAs TJ with low (2.2 x 10 ¹⁸ cm ⁻³) and high (2.2 x 10 ¹⁹ cm ⁻³) doping in GaAs	111
Figure 7.15: Donor doping profile before and after annealing at 650 °C for 30 minutes	112
Figure 7.16: Peak tunneling current versus GaAs for annealed and unannealed TJ with (a) 30 Å doping spike and (b) thick InGaP layers.....	112
Figure 7.17: Peak tunneling current density versus indium composition for an InGaP/InGaAs/AlGaAs TJ for a 15, 30, and 45 Å InGaAs thickness.	114
Figure 7.18: Peak tunneling current versus indium composition for an InGaP/GaAs/AlGaAs TJ with 30 Å GaAs. The indium carryover is modeled as a constant composition region at the InGaP/GaAs interface.	115
Figure 7.19: Peak tunneling current versus indium composition for an InGaP/GaAs/AlGaAs TJ with 45 Å GaAs. The indium carryover is modeled as a constant composition region at the InGaP/GaAs interface.	116
Figure 7.20: Peak tunneling current density versus doping density in the GaAs of a InGaP/GaAs/AlGaAs TJ with a 10 Å In _{0.4} Ga _{0.6} As layer representing the indium carryover.	117

1. Comparison of energy sources

Energy is essential for the existence of modern, industrial civilization. The gross domestic product (GDP) per capita is strongly correlated with the energy use per capita in a country [1]. The growth of a modern economy requires the development of energy resources and must be constantly evaluated if this growth is to continue. The ideal source of energy is plentiful, cheap, reliable, safe, and has a minimal impact on the environment, but there is no single source of energy that fulfills all of these requirements at any particular place and time. This has led to the development of several different energy sources and different methods to harness each of these resources. One particularly large energy resource is the Sun. The total yearly energy transmitted from the Sun to the Earth as radiation is 5.46×10^{18} MJ [2], which is ten thousand times the current world energy use per year. All of the currently exploited energy sources, except for nuclear and geothermal energy, are ultimately the product of solar energy. However, it is also possible to produce electrical energy directly from this solar radiation as photovoltaic energy. To properly evaluate the potential of photovoltaic energy generation, it is necessary to compare it both to current and emerging energy sources.

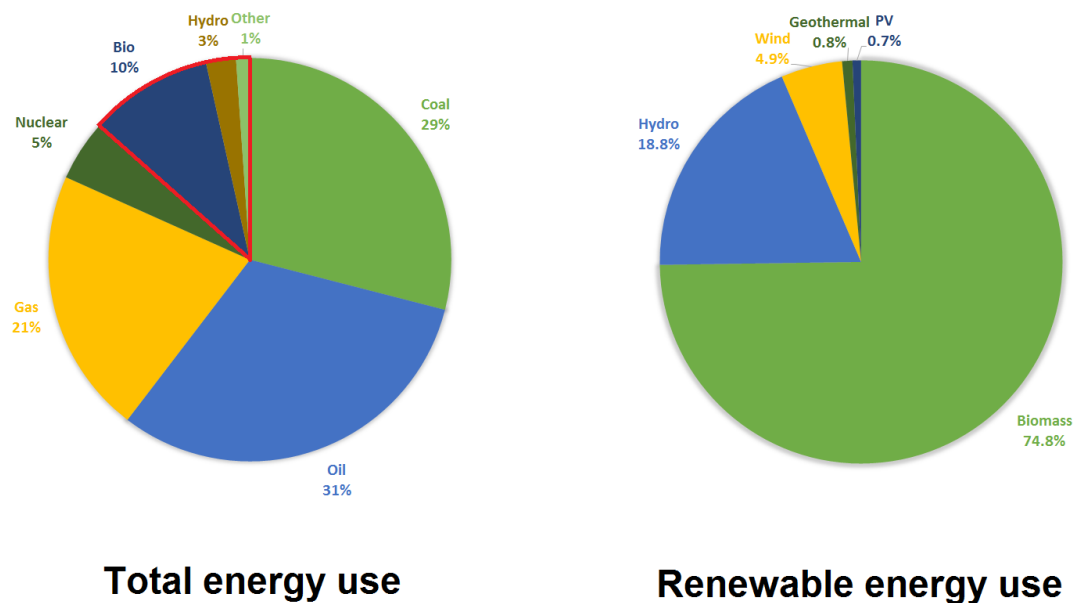


Figure 1.1: Distribution of total energy use and renewable energy use by source. The red line highlights renewable energy sources. Photovoltaic and solar thermal energy generation are currently a small portion of both renewable energy use and total energy use.

1.1. Criteria for evaluating energy sources

Worldwide energy usage totaled 5.61×10^{14} MJ in 2012, the breakdown of which into different sources is shown in figure 1 [1]. The majority of energy production is from coal, oil and natural gas, which are collectively known as fossil fuels since they are produced from the decomposition of marine and terrestrial lifeforms over time periods on the order of millions of years. The primary drawback of fossil fuels is that they are non-renewable, which means that they will be depleted well before they have the chance to regenerate. The other three major sources of energy are nuclear, hydroelectric and biomass. Nuclear fission is a non-renewable energy source that is subject to the depletion of uranium and thorium reserves. Hydroelectric and biomass are renewable sources of energy but they have a limited capacity for growth since efficient generation of hydroelectric energy requires large, swift moving rivers, many of which are already in use [3] and biomass is inefficient in terms of land use and competes with the growth of food sources [4]. To maintain the current rate of energy usage will require the development of other renewable sources of energy.

This chapter will briefly summarize the advantages and disadvantages of various energy resources that are either in use or are in development for use in the near future. Since solar energy is currently an underutilized resource, it will conclude with an evaluation of the role photovoltaics have in as a future energy source in comparison to current and developing resources.

There are several criteria for evaluating an energy resource. Some of these criteria will be more important for particular resources.

1. Cost: Cost is probably the single most important consideration when evaluating the potential for a particular resource [5]. The low cost of fossil fuel sources is responsible for their dominance as the primary energy sources on the planet. The success of any energy source depends upon being able to compete with coal as a source of electricity and oil as a transportation fuel. Technological development of alternative energy sources has often come when the cost of existing energy sources was high [6].
2. Current and potential reserves: One way to categorize energy resources is either as renewable or non-renewable. A renewable resource is one where the rate of usage is lower than the rate of replenishment. This means that the renewable/non-renewable distinction can depend upon how fast it is being utilized. For instance, wood is considered a renewable energy source, but forests can take decades to replenish [7]. This has led to the depletion of the biomass resources in some countries [8].

3. **Environmental impact:** Most energy resources have some environmental impact, although it varies depending upon the source. The burning of fossil fuels releases sulfur dioxide (SO₂), nitrogen oxides (NO_x) and carbon dioxide (CO₂) as waste products. SO₂ and NO₂ are known to produce acid rain [9] and CO₂ is a greenhouse gas and has been shown to be responsible for an increase in global temperatures [10]. The cost of many environmental effects of energy generation are not borne by either the producers or the consumers of energy resources. These effects can be mitigated by requiring energy producers to include technological solutions to minimize the environmental impact of energy generation or to impose fines or issue tradable pollution credits [11] so that the environmental impacts are included in the cost of that particular energy resource.
4. **Reliability:** The demand for energy is not constant over the course of a day or a year. For instance, electrical demand is often higher during the day than the night. Colder climates will require more energy for heating during the winter while in warmer climates more energy is required in the summer for air conditioning. The minimum energy demand is called the *base load* while the maximum energy demand is the *peak load*. Periodic energy sources that do not correlate to the demand cycles must include other sources that can be supplied continuously and can be increased in response to increases in demand.
5. **Scalability:** Some energy sources, such as hydroelectric and geothermal, can be produced more efficiently in particular locations. This leads to the situation where the regions with the lowest cost of generation can be fully exploited, limiting further growth of a particular resource. There is also some concern with the scalability for developing energy resources. Many of the most efficient methods of photovoltaic energy generation use rare elements such as indium and tellurium. The availability of these materials may limit the ability of these technologies to be used for large-scale electrical generation [12].
6. **Political and social impacts:** Energy resources are rarely located in the same place that they are utilized. This often results in trade between energy rich producer countries and energy poor consumer countries. The Organization of Petroleum Exporting Countries (OPEC) was founded in 1960 to serve the interests of the largest oil exporting nations [13]. Wars and social unrest in these countries has resulted in periods with high oil prices. This has encouraged the development of energy resources that are not as vulnerable to supply restrictions due to political issues.

1.2. Current energy sources

These are resources that are currently responsible for the majority of mankind's energy use. As of 2012 they represent 99% of all energy use.

1. Coal

Coal is formed from terrestrial plant matter that has transformed over long periods of time to a material that is comprised primarily of carbon with impurities of hydrogen, oxygen, nitrogen and sulfur. It is the second most important energy source behind oil and is the largest source for electricity generation, with 40% of electricity worldwide produced from coal [4]. While hydroelectric and geothermal resources are the lowest cost sources when available, they are geographically limited to certain locations, which often makes coal the cheapest option for electrical generation. Given the current demand for coal, there are enough proven reserves to last more than one hundred years [14]. The primary drawback of coal is that it is a significant source of particulates, SO₂ and CO₂. Particulates and SO₂ can be removed from the exhaust of power plants with a small increase in electrical prices [15]. To date there is no economically feasible method for removing CO₂, making coal one of the primary sources of greenhouse gases.

2. Oil

Oil, or petroleum, is formed from the decomposition of marine organisms. It is composed of a mixture of hydrocarbons with five or more carbon atoms; lighter hydrocarbons are known as natural gas. Crude oil is almost always processed by distillation, which roughly separates its components by molecular weight. Petroleum distillates are primarily used as transportation fuels due to their high energy density [16], but they are also used as a feedstock for the chemical industry and in the construction of asphalt roadways. It is used less often as a source of electrical generation due to higher costs, but the ability to quickly increase the power from oil burning generators make it useful for periods of peak demand. Oil suffers from many of the same environmental issues as coal as it releases SO₂, NO_x and CO₂ as exhaust products. The remaining reserves of crude oil are less than those of coal, with 35 more years of proven reserves remaining [14].

3. Natural gas

Natural gas is composed of lighter hydrocarbons with between one and four carbon atoms per molecule. It is often found in the same location as crude oil, but also exists as separate gas only deposits. In the past it was often burnt off or otherwise discarded during the extraction of crude oil due to technological difficulties with extraction and transportation, but is now the third largest source of energy behind coal and oil. It does have some environmental benefits relative to the other fossil fuels. Natural gas is almost entirely composed of carbon and hydrogen, meaning that

the only exhaust products are carbon dioxide and water. Also, natural gas produces a larger amount of energy per mole of carbon dioxide released in comparison to coal and petroleum distillates [17]. Current reserves are expected to last 37 years [14].

4. Nuclear fission

Certain isotopes of very heavy elements such as thorium, uranium and plutonium can release large amounts of energy when bombarded with neutrons. The energy released is much larger than from fossil fuels. For instance unenriched uranium can release 500 GJ of energy per kilogram of fuel compared to coal which will release only 25 MJ when one kilogram is burned [18]. Currently nuclear fission is responsible for 4.8% of the energy produced in the world, but it is a major source of electricity in some countries; in France nuclear power is responsible for 73% of all electrical generation [19]. The main drawbacks of nuclear power are the production radioactive waste and the potential for nuclear accidents that can render large areas uninhabitable. The major accidents at Chernobyl in 1986 and Fukushima in 2011 have resulted in a decrease in the construction of new nuclear plants and some countries have even abandoned nuclear power altogether. Despite this, nuclear is promising as it is one of the few mature energy technologies that does not produce any greenhouse gases. Current reserves are capable of providing energy for 78 years [20]. Breeder reactors, which are capable of transmuting non-fissile isotopes into fissile ones could extend the life of nuclear fuels indefinitely [21].

5. Hydroelectric

Hydroelectric generation uses the potential energy in a flowing river to power electrical turbines. Large hydroelectric plants often involve the construction of a dam on a river in order to provide more control over generation. Currently hydroelectric is responsible for 2.4% of the energy produced in the world. It is a renewable resource and produces no greenhouse gases, but does have some downsides. Hydroelectric plants must be built on rivers that have high volumetric flows and large changes in elevations, which limits their geographic distribution. The hydroelectric potential of the world's rivers is about 13.5 PWh of which 2.77 PWh, or 21%, is currently in use [22].

6. Biomass

The burning of wood, peat and agricultural waste was the primary energy source for most of pre-industrial civilization and is still a major source of energy in many economically undeveloped nations. Biomass also includes the more technologically advanced biofuels, which are products such as methanol, ethanol and methane that are produced from the decomposition or fermentation of biological materials. Biomass currently represent 10% of the energy use on earth. Biomass can

be renewable but it can also be non-renewable if it is being exploited faster than it can be replenished. When used renewably it produces no net CO₂ since any CO₂ produced during burning is recaptured by growing plant material. One drawback of biomass is that it is very inefficient in terms of land and water use. One hectare of land produces 72 GJ of biomass energy as ethanol from corn, which would require 77 million hectares, or half of the earth's land area, to supply all current energy use [23].

1.3. Future energy sources

These energy sources currently represent about 1% of the total energy production of the world. Some, such as wind and solar photovoltaic, have been successfully implemented but require further technological development in order to be competitive with other energy sources. All of these sources are renewable or, in the case of nuclear fusion, use a fuel that is practically inexhaustible.

1. Wind

Wind is the result of pressure differences caused by unequal heating by the Sun on the Earth's surface. The total amount of energy available from wind has been estimated to be 2.3×10^{15} MJ, greater than the total world energy use [24]. As with other sources of energy from natural phenomena, some locations, such as mountain and coastal areas, are more conducive to wind generation. These locations have the advantage of having little other economic use, but their remoteness makes it difficult to integrate wind generators into the existing electrical infrastructure.

2. Nuclear fusion

Nuclear fusion is the generation of energy by combining small nuclei into larger ones. It has the capability to provide energy even more efficiently than nuclear fission. Furthermore, the best fission candidates are the isotopes of hydrogen deuterium and tritium, which can be produced from seawater and lithium, respectively. This means that fusion has the potential to provide power for more than 23 million years and indefinitely if other fusion reactions were to be exploited [25]. However, fusion reactions require very high temperatures ($> 10^6$ K) which precludes the use of any material to contain the reaction. Currently all containment methods require more energy than what can be extracted from the fusion reaction.

3. Tidal, wave and ocean current

All of these methods are similar to hydroelectric in that they harness the power of moving water. Tidal uses the change in elevation in the water due to the tides to produce energy. The average displacement between low and high tide is only 4 m, but this can be amplified by the geography in certain locations, such as the Atlantic coast of Canada [26]. Wave and ocean current both

harness the energy of water far from the shore, which creates engineering challenges in installing and maintaining generating systems and transmitting energy from so far offshore.

4. Geothermal

There is a large amount of thermal energy stored in the earth's core and mantle. In some locations there are hot regions close enough to the earth's surface so that either hot water or steam can be extracted in order to power electrical turbines. Like hydroelectric power, there are a limited number of locations where geothermal power is able to produce energy efficiently, but it produces some of the lowest cost electrical power in the world.

5. Solar thermal

Solar thermal is the use of solar radiation to warm a fluid, which can either be used directly or to drive a turbine in order to produce electrical power. The direct use of solar thermal energy can be used either to provide heating or as a source of hot water for a building. In order to provide high enough temperatures for efficient electrical generation requires a larger installation with some method for focusing the solar radiation. Several pilot plants have been built using this concept, the largest with a 392 MW generating capacity [27].

6. Solar photovoltaic

A solar photovoltaic (PV) device is one where solar radiation is directly converted to electricity. There are two facts that make PV a promising technology. The first is the large amount of incident solar radiation on the earth's surface, which is capable of providing all of the energy used on the planet. The second is the very high theoretical efficiencies of PV, as high as 95%. Practical considerations prevent actual devices from coming close to this number, but state-of-the-art photovoltaic devices are capable of efficiencies above 45% [28]. The primary problem with PV currently is the high price for power generation. There are also technical difficulties with integrating PV systems into current electrical distribution systems due to the intermittent nature of solar energy.

1.4. The potential for photovoltaics

As mentioned in the previous section, the primary block on the adaptation of PV generation is the high cost. However, there is some reason to be hopeful concerning the potential of PV. All of the fossil fuel sources are non-renewable resources, which means there will be depleted at some point in the future. Even before they are fully depleted, it will be necessary to access less productive sources, which will raise energy prices from these sources and make photovoltaics more attractive. Nuclear fission has a potentially longer lifetime, but costs associated with disposal of waste and nuclear

accidents may limit its growth. Including the environmental benefits of PV relative to other sources of energy, they may be an attractive source of large scale electrical generation in the near future.

2. Basics of photovoltaics

It is necessary to first introduce the basic principles of photovoltaic devices. Photovoltaic devices depend upon the photovoltaic effect, which is the generation of voltages and electrical currents in a material when exposed to light. The energy distribution of solar energy will be discussed, including the effect of atmospheric absorption. In photovoltaic devices, the band structure of semiconductor materials allows them to absorb solar radiation in order to generate charge carriers which are separated by a pn-junction structure in order to produce electrical power. The various metrics for photovoltaic devices such as short circuit current, open circuit voltage, fill factor and efficiency will be introduced. Finally, the structure of a single junction solar cell will be given including windows, back surface fields and ohmic contacts.

2.1. Solar irradiance and the solar spectrum

The simplest model for solar radiation is a black body radiator with a temperature of 5800 K. This is a reasonably accurate model for the energy distribution for solar radiation in space, and can be used for photovoltaic devices outside of the Earth's atmosphere. While the energy distribution remains constant, the magnitude of the energy flux will depend upon the distance from the Sun. For the solar power density outside the earth's atmosphere, a commonly accepted standard called air-mass zero, or AM0, uses an average value of 1366 W/m^2 [1]. The term 'air-mass' is used to describe the effect of atmospheric absorption on the solar spectrum. A value of air-mass 1 represents the absorption from the atmosphere when the sun is at zenith and will be larger than 1 when the sun forms an angle away from the zenith.

Since the sun is only at zenith at particular times and dates in tropical latitudes, it is standard to use a larger air mass to describe solar radiation. An air mass of 1.5, or AM1.5 corresponds to an angle of 48.2° from the zenith [2]. Additionally there are two methods for describing AM1.5: air mass 1.5 direct, or AM1.5D, which gives the irradiance from the direction of the solar disc and air mass 1.5 ground, or AM1.5G, which is the same as AM1.5D with the scattered light from the celestial hemisphere included. AM1.5G is typically used to characterize flat panel solar cells which collect light from all directions while AM1.5D is used to characterize concentrator solar cells, which are exposed primarily to light that is concentrated from a small area in the direction of the sun. Concentrator systems will be discussed in more detail in the next chapter

Figure 1 shows the ASTM AM0, AM1.5D and AM1.5G spectra between 280 and 2500 nm [1, 2]. The irradiance from the AM1.5 spectrum is lower than that of the AM0 for two reasons: 1) since the sun is at a shallower angle, the light will be spread out over a larger area. 2) As light passes through

the atmosphere, it is absorbed by molecules such as water and carbon dioxide at characteristic wavelengths. This is particularly apparent in the infrared region, which shows several wavelength ranges that have a low irradiance. As a result, the total irradiance from the AM1.5 spectra is lower than that of the AM0, with standard values of 1000 W/m^2 for AM1.5G and 900 W/m^2 for AM1.5D [2].

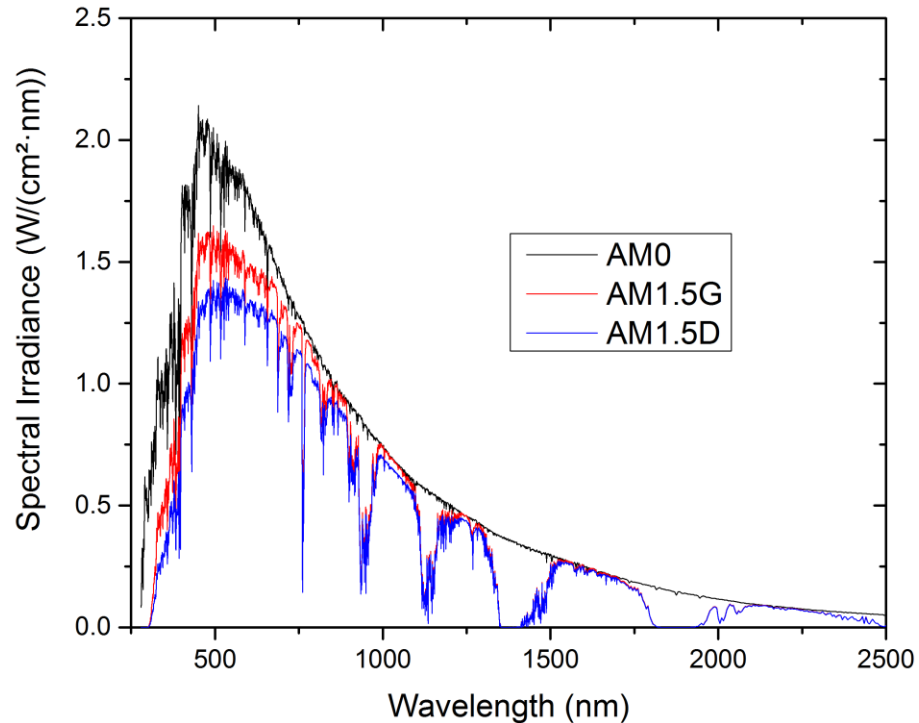


Figure 2.1: Spectral irradiance for the AM0, AM1.5G and AM1.5D standard solar spectra as defined by ASTM.

2.2. Band structure and light absorption

A majority of photovoltaic devices are composed of semiconductor materials. A major advantage of semiconductors is the ability to change their optical and electrical properties through small changes in the semiconductor composition. This makes it possible to construct sophisticated structures that are capable of converting light energy into electrical energy in a highly efficient manner. In order to understand the behavior of semiconductors and design photovoltaic structures, it is first necessary to describe their band structure.

2.2.1. Origin of band structure

In a single atom, electrons are confined to discrete energy states also known as quantum states or orbitals. An electron also possesses two types of angular momentum: one that is a property of the orbital and the other is an inherent angular momentum, also known as spin, which can take on a value

of either $\frac{1}{2}$ or $-\frac{1}{2}$. Since the spin is of half integer order, electrons belong to a class of particles known as Fermions which precludes two electrons from occupying the same quantum state [3]. This means that equilibrium the electrons in an atom will occupy the lowest energy quantum states with two electrons of opposite spin in each state. Higher energy states exist, but can only be occupied when an electron absorbs enough energy to be promoted to the higher energy state.

When atoms combine to form molecules, the total number of electrons and quantum states remains the same but the atomic orbitals will combine to form molecular orbitals. The energy of these orbitals will differ from the energy of the isolated atoms and depends upon the spatial arrangement of the atoms in the molecule. As with the electrons in atoms, the electrons in the molecule occupy the lowest energy states with higher energy states available but typically unoccupied in the absence of some excitation process.

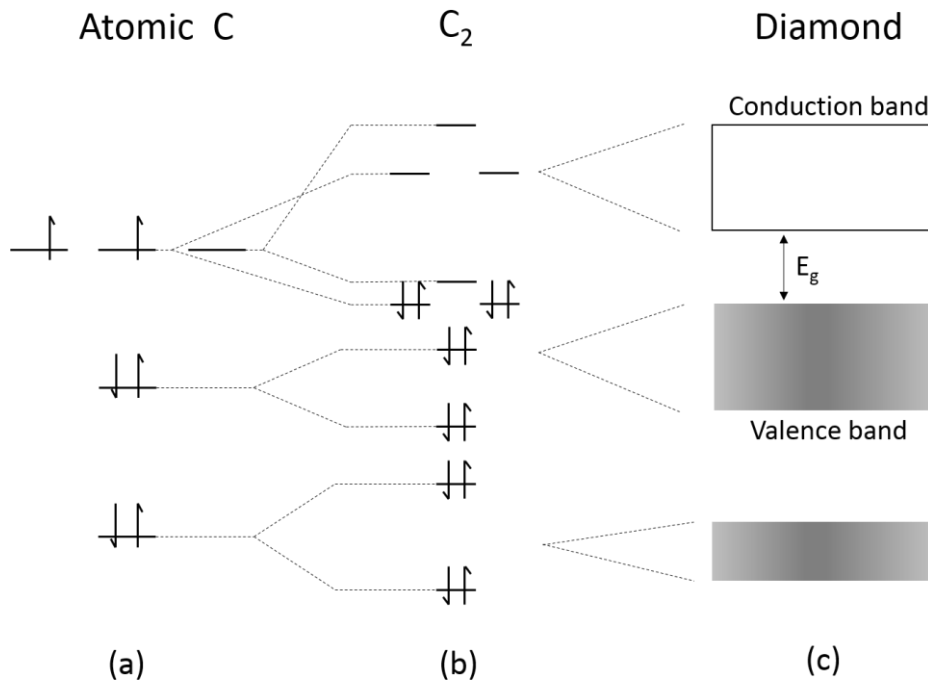


Figure 2.2: Formation of the band structure. The (a) atomic electronic states for a carbon atom form (b) molecular states for the diatomic carbon and the number of quantum states is preserved. The transition from discrete molecules to the (c) periodic diamond structure results in the formation of bands rather than discrete molecular states.

Some materials bond together to form large, periodic structures known as crystals. The smallest repeating unit of a crystal is the unit cell and the dimensions of this unit cell are the lattice constant of the material. For many semiconductors, the unit cell is cubic which means that there is a single lattice constant. When atoms are bound together in a crystal lattice the total number of states can be very

large. For instance, 1 cm^3 of silicon contains 5×10^{22} atoms [4]. For such materials it becomes easier to describe the energy states as bands rather than discrete states. As with molecular states, there are low bands which are typically filled and higher energy bands that are typically unfilled. The highest energy band that is filled is called the valence band (VB) and the lowest energy band that is unfilled is the conduction band (CB). Figure 2 shows the progression from atomic states to molecular states to band states. The energy difference between the valence band and the conduction band is known as the band gap. Materials with a band gap between 0.5 eV and 5 eV are semiconductors. Semiconductors in this work are formed either from elements in group IV of the periodic table (silicon, germanium) or binary compounds from the neighboring groups III and V (gallium arsenide, indium phosphide). Different materials can also be formed with alloys of group IV or III-V semiconductors [5].

2.2.2. Charge carriers

At absolute zero the valence band is entirely filled with electrons, while the conduction band is empty. This means that the semiconductor will have a very large resistance since there is no mechanism for charge conduction: there are no available charges in the conduction band and there are no empty states for electrons to move to in the valence band. For electrons to conduct in either band, an electron must be added to the conduction band or removed from the valence band. One way this can occur is the thermal excitation of an electron from the valence band to the conduction band. At a given temperature the probability of finding an electron at a particular state is given by the Fermi-Dirac distribution [6]:

$$f(E) = \frac{1}{1 + e^{(E - E_f)/kT}} \quad 2.1$$

This distribution is a function of temperature; at higher temperatures more electrons will be present in the conduction band. The quantity E_f is the Fermi energy or Fermi level and it represents the equilibrium energy where a state has a 50% chance of being occupied. For pure semiconductors it is close to midway between the conduction band and valence band edges. The thermal excitation of an electron in the conduction band also leaves an empty state in the valence band. This vacancy can be treated as particle known as a hole which has the same charge as an electron but with the opposite sign. In pure semiconductors there is an intrinsic carrier density that is the same for electrons and holes. This carrier density increases as temperature increases.

It is possible to describe the behavior of electrons in the semiconductor bands by solving the Schrödinger equation using the periodic boundary conditions of the crystal lattice. However in many

cases it is easier to approximate both the valence and conduction bands with a parabolic E-k relationship [7]

$$E(k) = E_0 \pm \frac{\hbar^2 k^2}{2m^*} \quad 2.2$$

$E_{0,c,v}$ is the energy at the vertex of the parabola and the +/- depends upon if the band is the conduction/valence band. The parabolic model of the valence and conduction bands are shown in figure 3. The quantity m^* is known as the effective mass of the band and will differ between bands and depends the composition of the semiconductor. There are two features that should be noted in figure 3. The first is that the conduction band has several local minima: one at $k=0$ and several with $k \neq 0$. When the absolute minimum energy is at $k=0$, the semiconductor is said to have a direct band gap, when it is at $k \neq 0$ it is indirect. This will be important when discussing the absorption of light in semiconductors. The second is that the valence band is always centered at $k=0$, but there are two degenerate bands with different effective masses, one the light hole band and the other the heavy hole band. In semiconductors with cubic symmetry, the two bands are degenerate; that is, they have the same maximum energy. However, in some cases the semiconductor lattice may become strained, breaking the cubic symmetry. This results in one of the hole bands being at a higher energy than the other [8].

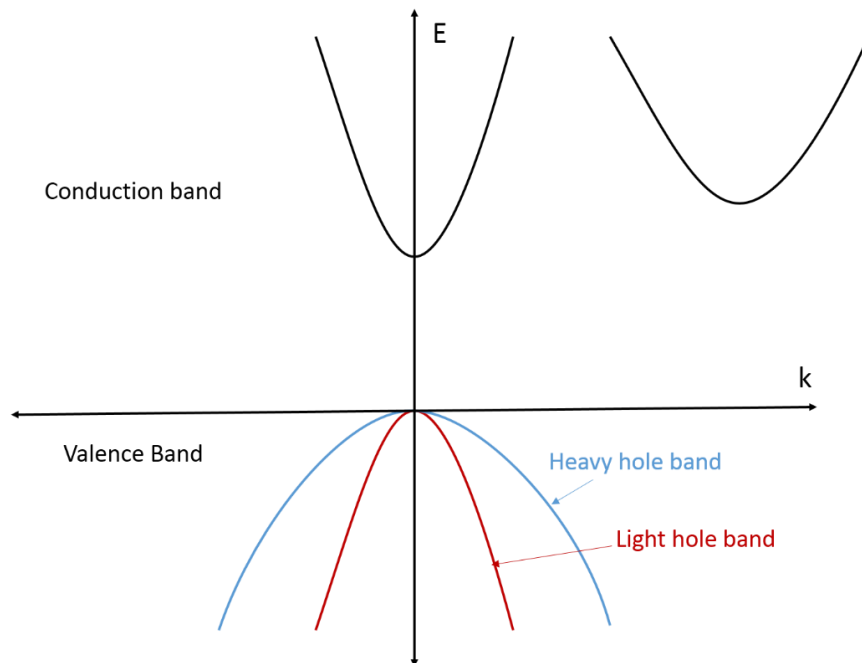


Figure 2.3: Simplified band structure for a semiconductor. The valence band minimum is always at $k=0$ and for unstrained materials is composed of two degenerate bands, the light hole band and the heavy hole band. The conduction band minimum is shown to be at $k=0$, but it may be at $k \neq 0$ for other semiconductors.

Charge carriers can also be generated by the addition of particular impurities known as dopants to the semiconductor lattice [9]. A dopant atom will have either an excess or a deficiency of electrons relative to the atom it is replacing. Those atoms with an extra electron can produce an occupied state close to the conduction band and are known as donors since the electron can be easily promoted to the conduction band. Likewise, an atom with a deficiency of electrons can produce an empty state near the valence band and are called acceptors since they can accept an electron (or donate a hole) from the valence band. Semiconductors with donor dopants are also known as n-type while ones with acceptor dopants are known as p-type.

The addition of dopants to a semiconductor will change the position of the Fermi level. For a semiconductor in equilibrium the Fermi level will move closer to the band that is doped, the conduction band for n-type doping and the valence band for p-type doping. This means that it is impossible to have carrier concentration higher than the intrinsic density in both bands. If donors and acceptors are added to the same material, the Fermi level will be determined by the one dopant that is in excess. Producing a non-equilibrium carrier distribution requires an external input of energy to the semiconductor.

2.2.3. Generation and recombination

It was stated in the previous section that charge carriers can be generated in the CB or VB either from thermal excitation of electrons from the VB and from the addition of shallow donor and acceptor states. If there is no energy input to or output from the system then the semiconductor is in thermodynamic equilibrium and the carrier densities will not change without some net transfer of energy. With a net energy transfer, carriers can be generated with concentrations that deviate from the equilibrium values. When the system is out of equilibrium, the reverse process can occur as well. The transfer of an electron from the conduction band to the valence band can be viewed as the destruction of both an electron and a hole. This process is known as recombination.

There are several methods for generating carriers in non-equilibrium conditions, one of which is through the absorption of photons. Photons with energies greater than the band gap have a chance to be absorbed, generating an electron and a hole. The absorption of multiple low energy photons is possible, but it is not a significant process except at very high light intensities. The chance that a photon is absorbed is given by the absorption coefficient, α , which is a function of the photon energy. A larger absorption coefficient corresponds to a higher probability of a photon being absorbed. Figure 4 shows the absorption coefficients of both silicon and GaAs [10, 11]. The absorption generally increases at energies above the band gap and is significantly larger in direct band gap materials, such

as GaAs, compared to indirect band gap materials, such as Si. As a result solar cells made from indirect band gap materials must be made thicker than those made from direct band gap materials.

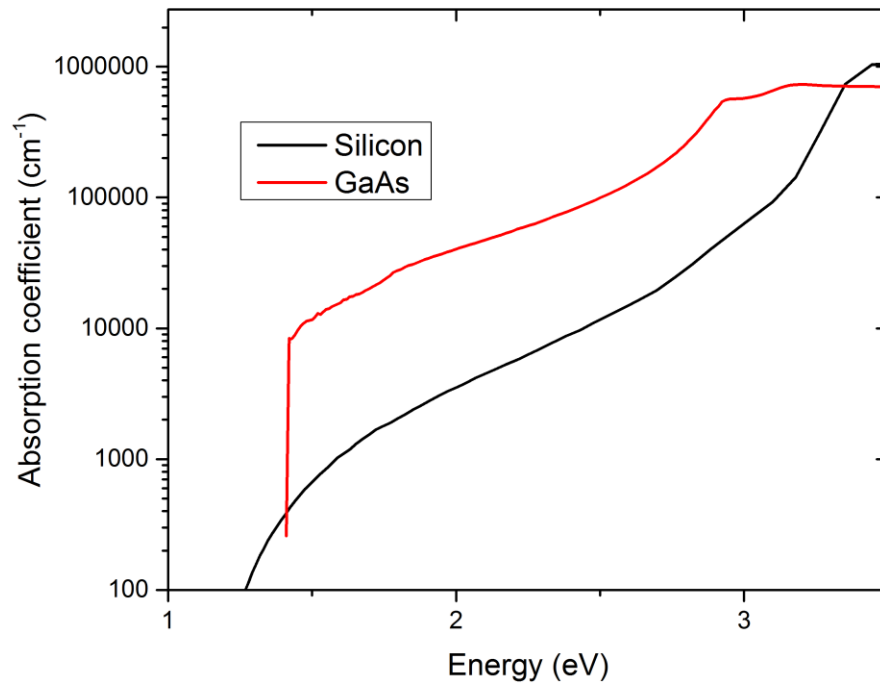


Figure 2.4: Absorption coefficient of silicon and gallium arsenide as a function of photon energy. Since the GaAs is a direct band gap semiconductor, it has a much larger absorption coefficient at most energies.

The inverse of the generation process is recombination, which occurs when the carrier density in one of the bands is higher than equilibrium carrier density. The rate of decay is inversely proportional to τ , the recombination lifetime of the carrier. The value of τ will depend upon the material, temperature and doping level. Irregularities in the crystal lattice form defects which are often sources of increased recombination. Recombination can also occur at any interface between two semiconductors or between a semiconductor and air. Recombination can either be radiative, where a photon is generated in the reverse of the absorption process, or non-radiative, where the energy from the recombination is lost as heat.

The total number of excess carriers in a region of space depends upon the rates of generation, G , recombination, R , and the change in the current density flow. This can be expressed using the continuity equation [4]:

$$\frac{\partial J_n}{\partial t} = \frac{1}{q} \nabla \cdot J + G_n - R_n \quad 2.3$$

The expression is written for electrons, but a similar equation can be given for holes.

2.3. Fundamentals of pn junctions

The purpose of a solar cell is to use the excess carriers generated from photon absorption in a semiconductor to generate a current before they can recombine. One structure that serves this purpose is the pn junction.

2.3.1. Diode equation

A pn junction is created when a p-type semiconductor forms a metallurgical contact with an n-type semiconductor. The two semiconductors are often composed of the same material, which is known as a homojunction, but this is not necessary and can form a heterojunction if the p- and n-type materials are composed of different semiconductors. In the absence of any external excitation, the pn junction is at equilibrium. In such a case, the Fermi level of both the n-type and p-type materials must be at a constant energy. This results in an offset between the conduction and valence band of the two sides of the junction, as shown in figure 5. This offset is the built in potential (V_{bi}) of the junction.

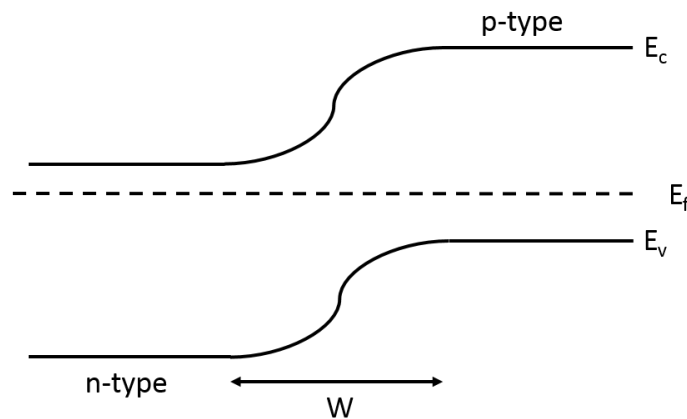


Figure 2.5: Valence and conduction band structure for a typical pn junction.

There are two physical processes that govern the behavior of the pn junction at equilibrium. The first is the diffusion of carriers. Electrons (and holes) will diffuse from regions of high concentration to regions of low concentration. In a pn junction this means that near the junction the carriers will diffuse into the other material, producing a region at the junction that has almost no mobile carriers called the depletion region. There is a net charge in the depletion region due to the presence of ionized donor (and acceptor) atoms without their corresponding mobile carriers. This results in an electric field which opposes the diffusion process. The electric field, \mathcal{E} , and potential of the junction depend upon two equations, the drift-diffusion equation and Poisson's equation, given in one dimension as [4]:

$$J_n = qn\mu_n\mathcal{E} + qD_n \frac{dn}{dx} \quad 2.4$$

$$J_p = qp\mu_p\mathcal{E} - qD_p \frac{dp}{dx} \quad 2.5$$

$$\frac{d^2\phi}{dx^2} = -\frac{d\mathcal{E}}{dx} = -\frac{q}{\epsilon}(p - n + N_d^+ - N_a^-) \quad 2.6$$

μ is the mobility of the electron or hole and depends upon the semiconductor and doping level. D is the diffusion constant and is proportional to the mobility. ϵ is the permittivity of the material. N_d^+ and N_a^- are the density of ionized donors and acceptors. At equilibrium the hole and electron current densities, J_p and J_n , will be zero. These equations, along with equation 2.3 can be used to calculate find the diode equation, which gives the current density of the diode as a function of the applied bias, V_a [12]:

$$J = J_0(e^{qV_a/nkT} - 1) \quad 2.7$$

In reverse bias the current is small and is equal to $-J_0$ where J_0 is the reverse saturation current. In forward bias the diode current increases exponentially. The quantity n is 1 for an ideal diode where recombination is negligible. For real diodes, n is greater than 1 and will depend upon the bias.

2.3.2. Diode equation for photovoltaics

When a pn junction is exposed to light excess carriers will be generated in both the n-type and p-type materials. Both holes and electrons are generated in equal quantities. However, in a particular material, the relative increase in minority carriers (electrons in p-type materials and holes in n-type materials) is much more significant. If these minority carriers can reach the pn junction before they recombine, they are swept across the depletion region by the electric field and become majority carriers. The optically generated current, J_{op} , flows in the opposite direction from the current generated from forward biasing the diode and is a function of the light intensity.

The J-V characteristic of the diode in the dark and exposed to light is shown in figure 6. The optically generated current causes the current to be reduced by J_{op} at all biases. The diode equation can then be written as

$$J = J_0 \left(e^{\frac{qV_a}{nkT}} - 1 \right) - J_{op} \quad 2.8$$

According to figure 6(b), a pn junction exposed to light can be operated in the first, third and fourth quadrants. In the first and third quadrant, the bias and current have the same sign, which means that

there is a net outflow of energy. This means that to perform as a photovoltaic device, the pn junction must operate in the fourth quadrant.

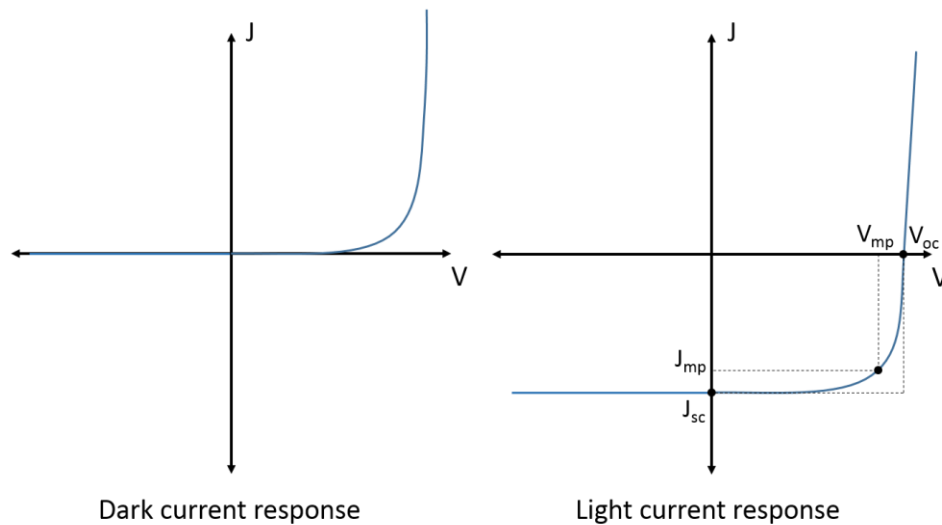


Figure 2.6: J-V response of a photovoltaic cell in the dark (dark current) and under illumination (light current).

2.4. Photovoltaic principles

There are several metrics for characterizing photovoltaics. They are useful in order to compare the relative merits of different structures as well as to determine the quality of a particular device. Most of these metrics will depend upon the intensity and the spectral composition of the incident light. As a result, they are typically given for a particular standard spectrum, such as AM0 or AM1.5G, depending upon the particular application of the solar cell

2.4.1. Short circuit current

The short circuit current, J_{sc} , is the current produced when the photovoltaic device is at zero bias. According to equation 2.8, at zero bias the current density will be $-J_{op}$ and so will only be due to the optical generation of carriers.

2.4.2. Open circuit voltage

The open circuit voltage is the voltage in forward bias where the current density is zero. For an ideal diode, this can be found from equation 2.9:

$$V_{oc} = \frac{kT}{q} \ln \left(\frac{J_{sc}}{J_0} \right) \quad 2.9$$

V_{oc} depends upon both the short circuit current density and the reverse saturation current density. In non-ideal structures V_{oc} will also depend upon n , the series resistance and the shunt resistance. V_{oc} is sensitive to the mobility and carrier lifetime in the photovoltaic cell, due increases the recombination rate and the reverse saturation current [13]. While large recombination rates can cause J_{sc} to decrease, V_{oc} also depends upon n and J_0 both of which will increase as the recombination lifetime decreases.

2.4.3. Fill factor

When the solar cell operates at either J_{sc} or V_{oc} the total power collected is zero. Between these two extremes, there is an operating point where the power output of the cell is the highest. This is the maximum power voltage, V_{mp} , and the maximum power current density, J_{mp} . Both V_{mp} and J_{mp} are less than V_{oc} and J_{sc} , respectively. As this represents a potential loss of power generated by the cell, the difference is expressed by the fill factor (FF) [14]:

$$FF = \frac{J_{mp}V_{mp}}{J_{sc}V_{oc}} \quad 2.10$$

For a particular J_{sc} and V_{oc} , a higher fill factor is more favorable. Fill factor is particularly sensitive to the shunt resistance, R_{sh} and the series resistance R_s . A photovoltaic cell with a large series resistance may have a large V_{oc} as a result. However, such a cell will output a lower maximum power and will have a lower fill factor as well.

2.4.4. Quantum efficiency

J_{sc} , V_{oc} and FF are given for exposure to the full solar spectrum, or in a laboratory setting exposure to a simulated solar spectrum. It can also be useful to determine the response of a photovoltaic device when exposed to light of a particular wavelength. The quantum efficiency of a cell is the probability that a photon of a particular wavelength will produce a carrier that will contribute to the current output of the cell. The ideal quantum efficiency is 1; it can be reduced by factors such as reflection from the surface of the cell, bulk recombination and surface recombination [15].

2.4.5. Efficiency

Efficiency is fraction between the amount of electrical energy generated by a photovoltaic cell and the energy of the photons incident on the cell. It is one of the most important metrics for solar cell efficiency and is often used to evaluate the performance of various photovoltaic technologies and to compare different designs for cells of a particular type [16]. It can be expressed in terms of J_{sc} , V_{oc} and fill factor as well as the incident solar power, P_{solar} :

$$\eta = \frac{FFJ_{sc}V_{oc}}{P_{solar}}$$

2.11

2.4.6. Sources of loss and maximum efficiency

There are several inherent sources of energy loss that limit the maximum efficiency of a single junction photovoltaic cell. While certain parameters such as reflection, series resistance and non-radiative radiation can theoretically be eliminated, there are three sources of energy loss that cannot be avoided. The limit placed by these three sources of loss is known as the Shockley-Queisser limit [17].

A photovoltaic cell can be considered as a heat engine with the hot source as the 5800 K temperature of the sun and the cold sink as the 300 K photovoltaic cell. The maximum efficiency of a heat engine is given by $\eta = (T_h - T_c)/T_h$ so for a photovoltaic cell the efficiency limit due to this source of loss is 95% [18].

The second source of loss is due to radiative recombination in the semiconductor. While non-radiative recombination can theoretically be reduced to zero, radiative recombination will always exist as the converse to the absorption process [19]. There is a fundamental limit on the radiative recombination lifetime based on the balance between absorption and recombination.

The final source of loss is due to the mismatch between the band gap energy and the energy of the incoming light energy. Any photon with an energy below the band gap will pass through the material and not be absorbed. On the other hand, photons with an energy larger than the band gap will lose any excess energy due to the rapid relaxation of any generated electrons and holes to the lowest available energy state in each band. This last source of energy loss results in an ideal band gap for the solar spectrum. Semiconductors with a large band gap will allow too much of the solar spectrum to pass through unabsorbed while those with a small band gap will have too many losses from thermalization. The highest theoretical efficiency for a photovoltaic cell with a single junction is 34% for a band gap of 1.34 eV [17]. Practical cells are below this limit with a record single cell efficiency of 28.8% for a GaAs cell [20].

2.5. Components of photovoltaic devices

The pn junction is the only essential component of a photovoltaic device. However, to maximize the cell efficiency, there are other components that must be included.

2.5.1. Emitter and Base

The pn junction of a photovoltaic cell can be split into two regions that are distinguished by their doping and their position in the cell. The emitter is the topmost portion of the junction which is the first to absorb any incident light. The base below the emitter and absorbs the remaining light, it is doped of the opposite type from the emitter. Since the absorption of a semiconductor generally increases as the wavelength of light decreases, the emitter will absorb almost all of the short wavelength light, allowing the longer wavelengths to pass through to the base. For this reason, the emitter is typically grown thinner than the base to reduce losses from recombination as minority carriers approach the junction. Each layer can be grown as either p-type or n-type, the particular choice will affect the ideal thickness of each layer due to differences in minority carrier lifetime and mobility [21].

2.5.2. Window

The surface recombination velocity is typically higher at a semiconductor-air interface compared to a semiconductor-semiconductor interface [22]. A window layer is a semiconductor that is placed at the top of the cell in order to lower the surface recombination. Since J_{sc} in a photovoltaic cell depends upon the minority carrier current, the window should lower the surface recombination of minority carriers. A good window will prevent minority carriers from reaching the surface of the cell, so there should be a band offset in excess of 0.1 eV (for operation at 300 K) in order to prevent the thermal excitation of carriers into the window material [23]. Since the window is the first layer encountered by an incident photon, it should also be transparent to any photons that are expected to be absorbed by the photovoltaic cell. As a result, window materials typically have a higher band gap than the rest of the cell and/or are made from indirect semiconductors which have significantly lower absorption than direct semiconductors.

2.5.3. Back surface field

The counterpart to the window is the back surface field (BSF) at the bottom of the cell. The BSF is a less critical component since the generation rate is lower in the bottom of the cell. This means that a poor surface recombination at the BSF will have a lower impact than a poor surface recombination at the window. As with the window, the BSF should prevent the escape of minority carriers from the rest of the photovoltaic cell. There is also no transparency requirement for the BSF, at least for single junction cells. This means that BSF can be compositional, where a different semiconductor materials is used as with the window, or formed from doping as a result of the band shift due to the Fermi level change from the low doped to high doped region.

2.5.4. Metal contacts

In order to extract current from a photovoltaic cell, it is necessary to add ohmic contacts to both sides of the junction. These contacts should be designed in order to minimize losses to series resistance. For the back of the cell, which does not receive incident radiation, the semiconductor surface can be fully metallized. The top contact must also allow for light to pass through the cell and cannot fully cover the top surface. Transparent conductors exist and are used for some types of photovoltaic cells, but they have too high of a series resistance for cells that operate with a high J_{sc} . The typical solution is to only partially metalize the top surface using thin metal contacts that are repeated at regular intervals. The thickness and spacing of these contacts are optimized to balance the losses from series resistance and shading due to the reflection of light from the contact metals [24]. The optimal design will depend upon the particular resistance of the metal and emitter layer as well as the operating conditions of the cell.

3. Multijunction photovoltaics, Quantum wells and superlattices, and tunnel junctions

3.1. Multijunction photovoltaics

In chapter 2 it was shown that the maximum efficiency of a photovoltaic cell illuminated by solar radiation is limited to 34% for three reasons: thermodynamic losses due to the transfer of energy from the 5800 K sun to the 300 K cell, losses due to radiative recombination of minority carriers, and thermalization and transmission losses due to the single band gap absorber. The use of a single band gap material is responsible for the largest portion of the efficiency loss, so in order to increase the efficiency it is reasonable to create a cell incorporates multiple absorbing materials.

3.1.1. Advantages and disadvantages of multijunction photovoltaics

A low band gap cell will absorb most of the solar spectrum, but will have large thermalization losses while a high band gap cell will transmit most light but have little thermalization losses. By incorporating two or more semiconductor materials in the same system losses from both transmission and thermalization can be reduced.

There are several ways to use materials with different band gaps in a single photovoltaic system as shown in figure 1. One is incorporate several materials into a single pn junction [1]. Another is to split the solar spectrum spatially and illuminate individual cells with different band gaps [2]. However, the most common method for integrating different semiconductor materials is the tandem multijunction solar cell [3], which is typically called a ‘multijunction cell’. In a multijunction cell each material forms a separate pn junction, or subcell. The junctions are stacked atop one another so that each subcell is illuminated sequentially by the same light source. Each subcell will absorb light that has an energy above the bandgap and will allow lower energy light to pass through to be absorbed by the other subcells. In order to be effective, the subcells must be arranged in order with the highest band gap subcell on top and the lowest band gap subcell on the bottom.

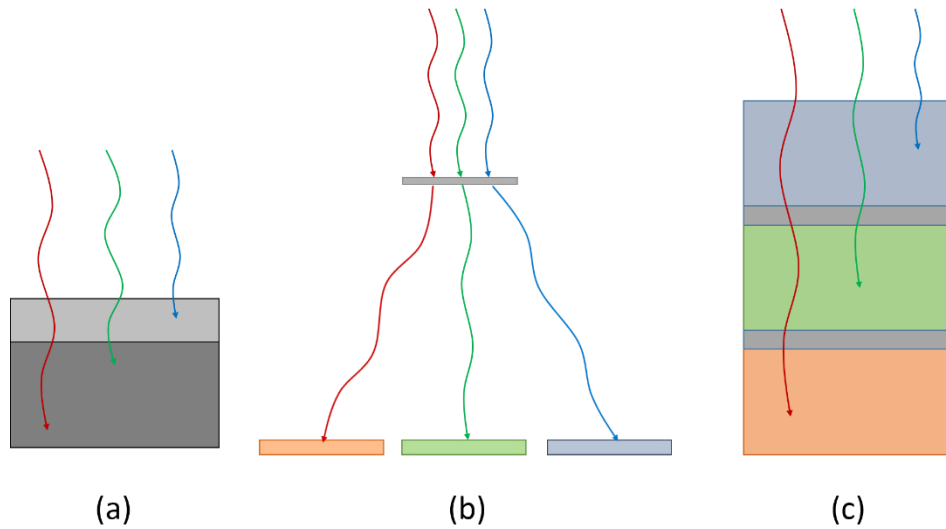


Figure 3.1: Three possible configurations for incorporating semiconductors of different band gaps into a photovoltaic system: (a) a heterojunction diode with different n-type and p-type materials (b) spatial separation of incoming radiation onto PV cells with different band gaps (c) a multijunction tandem cell with subcells connected materially, optically and electrically in series.

The most straightforward method for forming a multijunction cell is to grow all subcells as a monolithic crystalline structure on a semiconductor substrate. Since the purpose of the multijunction structure is to achieve very high efficiencies, the cell must be grown as a single crystal structure in order to avoid non-radiative recombination due to the presence of defects in the crystal lattice [4]. This requires each subcell to have the same lattice constant as the substrate material since the growth of mismatched crystal structures will result in the formation of defects. There are some techniques that can avoid the lattice matching constraint. If the lattice constant of a mismatched material is varied slowly, then fewer defects will form, although there will be more than if a lattice matched layer had been grown [5]. The growth of non-lattice matched materials is referred to as metamorphic growth. It is also possible to grow cells separately on different substrates and to join them together with a conductive adhesive using wafer bonding techniques [6].

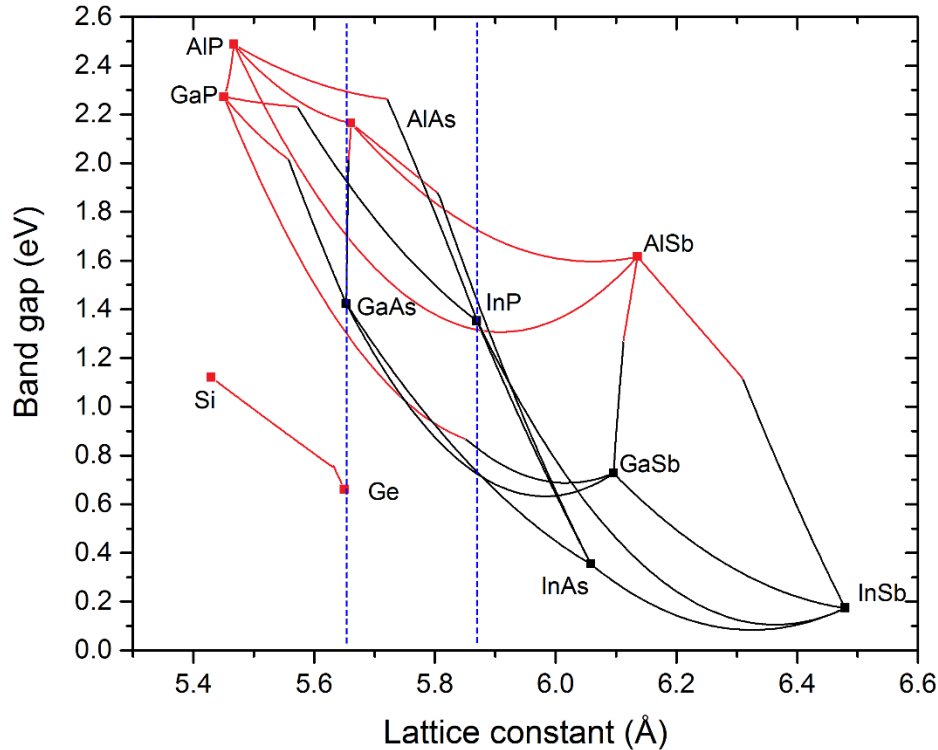


Figure 3.2: Plot of band gap versus lattice constant for several III-V semiconductors. The connecting lines represent ternary alloys with black lines for direct semiconductors and red for indirect semiconductors. The two vertical blue lines correspond to materials lattice matched to the common GaAs/Ge and InP substrates. The composition dependent band gaps and lattice constants were found from [7].

Since each subcell in a multijunction structure is composed of a single pn junction, it is necessary to place an ohmic contact between each subcell. In the absence of these contacts parasitic junctions would form between each subcell, reducing both V_{oc} and the efficiency of the cell. These contacts are typically formed with tunnel junctions (TJ), which are highly doped pn diodes [8]. Tunnel junctions behave as ohmic contacts at low biases and since they are composed of semiconductor materials, they can be transparent within certain wavelength ranges, unlike metals. Tunnel junctions will be discussed in more detail in section 3.3.

The stacked multijunction structure has the potential to achieve higher efficiencies than the single junction photovoltaic cell. The Shockley-Queisser limit under AM1.5D illumination are 32.5%, 44.3%, 50.1% and 65.4% for a 2, 3, 4 and infinite junction cell, respectively [9]. Table 3.1 shows the maximum efficiency and ideal subcell bandgaps for 2,3 and 4 junction cells under AM1.5D illumination and infinite concentration. Solar concentrators use refractive and reflective optics to concentrate the solar radiation into a smaller area, increasing the solar intensity in that area. They will be discussed in more detail in section 3.1.3.

Table 3.1: The ideal band gaps and maximum efficiency for 1, 2 and 3 junction PV cells at one sun and infinite sun concentration of the AM1.5D spectrum. Values in table taken from [9].

# Junctions	Concentration	Junction 1 E_g	Junction 2 E_g	Junction 3 E_g	Max efficiency
1	1 \times	1.13	-	-	32.5%
1	$\infty\times$	0.94	-	-	44.6%
2	1 \times	0.94	1.64	-	44.3%
2	$\infty\times$	0.71	1.41	-	59.7%
3	1 \times	0.71	1.16	1.83	50.1%
3	$\infty\times$	0.69	1.16	1.84	67.0%

While the efficiency can theoretically be increased by adding additional junctions the marginal benefit of adding an additional subcell decreases as the number of subcells increases. Non-ideal sources of loss can limit the number of subcells. For instance, the tunnel junction contact has non-zero resistance, which means there is a voltage drop at each TJ that will reduce V_{oc} and the total efficiency [10]. As each additional cell requires an additional TJ, adding more junctions may not be beneficial at a particular point. As a result, the highest efficiency multijunction cells have contained three junctions, with four junction cells only recently setting efficiency records.

3.1.2. Types of multijunction structures

Growing multijunction cells that are both 1) lattice matched to a substrate material and 2) possess band gaps close to the ideal energies is difficult with the available substrates and semiconductors. As a result one of the two conditions must be relaxed in a particular multijunction structure. The three predominant three junction cell structures are shown in figure 3. The first structure has all three subcells lattice matched to a germanium substrate, and so is called the lattice matched (LM) structure [11]. The bottom junction is formed from germanium, the middle junction is GaAs with a small fraction of indium (1% InAs) and the top junction is $In_{0.49}Ga_{0.51}P$. Other substrate materials, such as InP, do not have any binary or ternary alloys that possess the appropriate band gaps, especially for the top subcell. Even so, the three materials of the lattice matched structure do not have the ideal band gaps for a triple junction cell; E_g is too large for the top two cells and too small for the germanium subcell. As a result, the current through the multijunction stack is determined by the current generated in the top cells, which limits the maximum efficiency of the lattice matched structure to 48% rather than the 54% of an ideal triple junction cell on a Ge substrate [12].

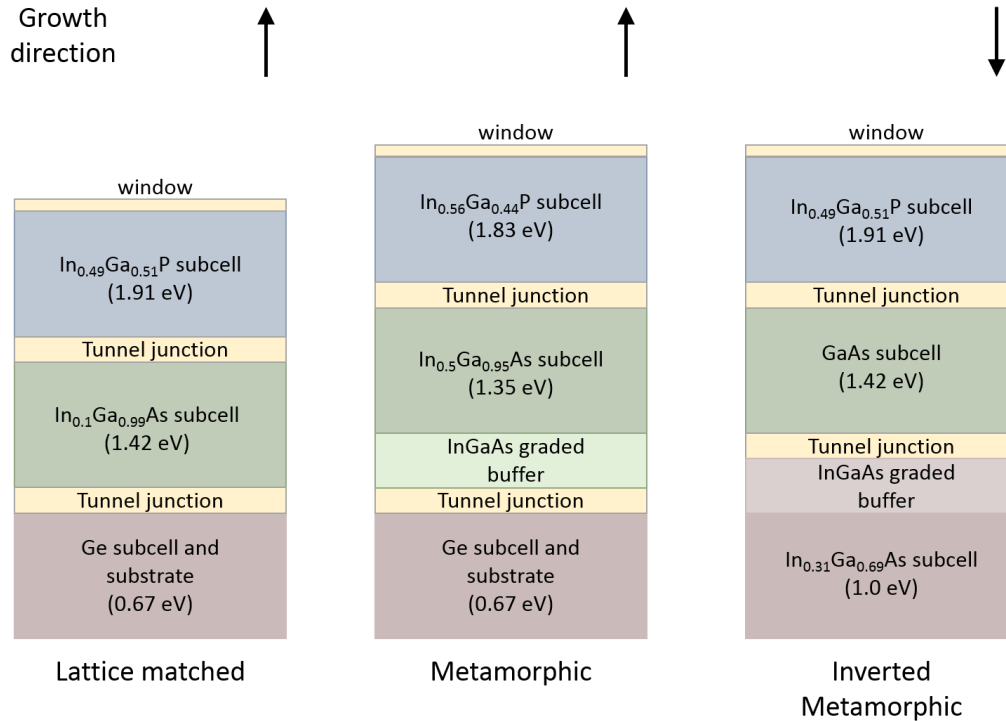


Figure 3.3: Schematic of the lattice matched, metamorphic and inverted metamorphic triple junction PV cells showing typical band gaps for each of the three subcells.

To solve the current matching problem it is necessary to grow subcells that are not lattice matched to the substrate material. A lattice mismatched material can be grown on a substrate to give a strained material, where the crystal lattice distorts in order to match the lattice constant in the two directions parallel to the growth surface. Growing a strained material results in a build-up of energy which is limited to a critical value, after which the material will develop dislocations in order to reduce the energy due to the strain [13]. The layer thickness at which dislocations begin to form is the critical layer thickness (CLT) and is typically too thin to grow subcells that will absorb a significant portion of the solar spectrum. Materials with a high dislocation density cannot be used as they will increase the non-radiative recombination in any subsequently grown layers, which will result in a reduction in V_{oc} and efficiency. In order to minimize the formation of defects, the lattice constant must be changed slowly by grading the composition of a material. Multijunction cells with subcells not lattice matched to the substrate are known as metamorphic cells, of which there are two varieties. The first cell is the upright metamorphic (MM) cell, as shown in figure 3. In order to reduce the band gap of the top two cells, a graded InGaAs layer is grown after the Ge cell. The InGaAs and InGaP cell generate more current than the top two cells of the lattice matched structure, increasing the maximum efficiency to 54% [14]. While the graded buffer layer reduces the number of defects, the defect density is higher

than that of lattice matched materials. As a result, practical metamorphic MJ cells do not have an appreciably higher efficiency than the best lattice matched MJ cells [14].

Higher band gap subcells are particularly susceptible to defect induced recombination. In order to reduce the effect of defects in metamorphic cells, the bottom junction can be grown metamorphically with the top two cells lattice matched to GaAs. Such a structure is known as an inverted metamorphic (IMM) multijunction cell. A metamorphic InGaAs bottom cell with a band gap of 1 eV improves the current balancing between the cells relative to the lattice matched structure, giving a maximum efficiency of 54% [15]. In order to grow a metamorphic bottom cell, the entire multijunction stack must be grown upside down and transferred to another substrate before the cell can be used. This additional processing step increases the expense of inverted multijunction cells.

Other 3- and 4- junction structures have been developed that have efficiencies that are close to those of the LM, MM and IMM structures. One three junction cell places reduces the current mismatch of the lattice matched structure by replacing the germanium cell with a 1.0 eV InGaAsN junction [16]. The InGaAsN is known as a dilute nitride since a small fraction (0-3%) of nitrogen causes a significant decrease in the band gap of a III-V semiconductor without the need to use a material with a larger lattice constant such as InGaAs. Another method is to grow InGaP and GaAs subcells on a GaAs substrate and InGaAs and InGaAsP subcells on a InP substrate. The GaAs substrate is then bound with a conductive and transparent adhesive to the the InP substrate and the GaAs substrate is removed. This structure has produced the highest efficiency for a multijunction cell, 46.0% [6, 17].

3.1.3. Concentrator solar cells

While multijunction cells are capable of producing the highest efficiencies of any solar cell structure, they are also significantly more expensive than single junction cells. There are two applications where the high efficiency of MJ cells is advantageous despite the cost. The first is for space applications where it is necessary to minimize the weight per watt generated since it is expensive to launch massive objects into orbit [18]. The second application is in terrestrial concentrator systems where reflective and refractive elements are used to concentrate solar radiation over a large area onto a much smaller photovoltaic cell. If there is no efficiency loss at higher concentration, the smaller cell should be able to generate the same power as a larger flat panel photovoltaic array. For instance, if a 1000 cm² array that generates 15 A is replaced with a system that concentrates a thousand times (1000×) onto a 1 cm² cell, this smaller cell should be able to also generate 15 A of current. Since a concentrator system allows for much smaller cells to be used, the cell cost is a smaller portion of the

total system cost compared to flat panel cells. This allows multijunction cells to be cost competitive with silicon and thin film technologies [19].

The design of space and concentrator multijunction cells will differ due to several factors. Since there is no atmospheric absorption in space, AM0 is used as the standard solar spectrum. For concentrator cells, the AM1.5D is used rather than AM1.5G since only a small portion of the scattered light is concentrated. The different solar spectra will change the current generated in each subcell, which means that there are different ideal band gaps for space and concentrator cells [9]. Concentrator cells must also be able to support much larger currents than space cells, this effects the design of the metal contacts, top cell emitter and tunnel junctions. The two types of cells must also be designed with different environmental factors in mind. Space cells are subject to much higher levels of ionizing radiation while concentrator cells are subject to fouling and thermal fluctuations due to the day/night cycle. This dissertation will focus on the use of multijunction cells in concentrator applications.

3.2. Quantum wells and superlattices

The materials in the multijunction cells discussed in the previous section were three dimensional, or bulk semiconductors. In these subcells each junction is formed from a single semiconductors with interfaces between different materials occurring only at the boundaries of each subcell. One location in the crystal lattice is indistinguishable from any other so properties such as the band gap, mobility, effective mass, etc. are consistent throughout the material. However, if a material of low bandgap is surrounded by a material with a higher band gap, the behavior of electrons and holes in this region can depend upon the material geometry as a well as the material composition. The dimensions of these structures must typically be less than 100 nm in order to exhibit behavior that differs from the bulk material. Figure 4 shows three such structures which differ in the number of confined dimensions. A structure with one confined dimension is a quantum well, with two confined dimensions is a quantum wire and with three confined dimensions is a quantum dot. The focus here will be on quantum wells and a structure that is formed from closely spaced quantum wells, the superlattice.

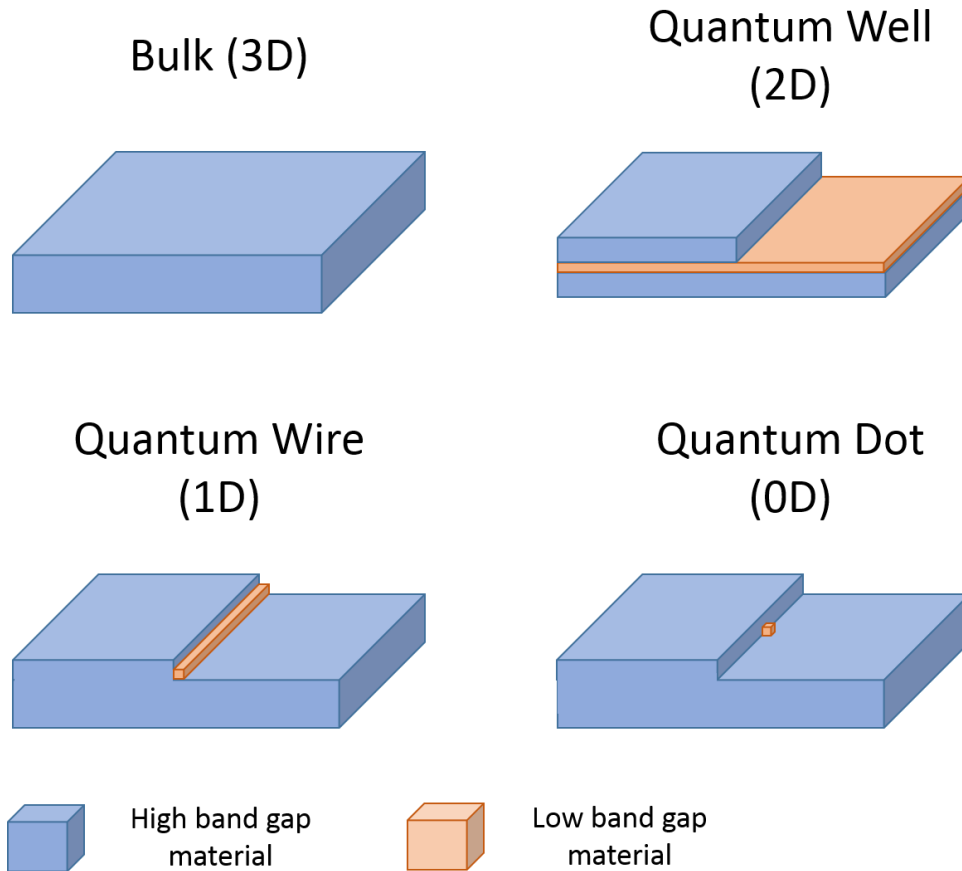


Figure 3.4: Physical layout of three reduced dimension semiconductor structures: the quantum well, the quantum wire and the quantum dot. The superlattice is formed from a series of closely spaced quantum wells.

3.2.1. Formation of quantum wells and superlattices

The basis of the quantum well and superlattice is the heterojunction, the metallurgical junction between two semiconductor materials. These two materials can differ in both band gap and electron affinity, the latter of which is the difference in potential between the conduction band edge and the vacuum potential of an electron. This means that in most cases there is an offset in both the valence and conduction band energies of the two materials. The magnitude of the band offsets depends upon the composition of the two semiconductors and has been either calculated or measured experimentally for many semiconductor pairs. Heterointerfaces that are of particular interest are InGaAs/GaAsP, InGaAs/GaAs, InGaP/GaAs and GaAs/AlGaAs.

It is possible to create a thin low band gap region surrounded by the high band gap material on both sides. The regions where the surrounding material is at a higher potential in the conduction band (or a lower potential in the conduction band) are quantum wells. In these regions the carriers are confined

to the well with two exceptions: a portion of the wavefunction of the confined carrier is present in the high band gap region and if a carrier can acquire enough energy it can pass over into the high band gap region. Confinement also results in the formation of discrete energy levels rather than the continuous bands in the bulk material. One advantage of quantum wells relative to bulk semiconductors is the ability to control the band structure of the structure by changing the composition and thickness of the quantum well.

It is possible to form multiple quantum wells by growing alternating layers of low band gap and high band gap materials. In such structures the high band gap material forms a barrier between adjacent wells. As mentioned before, a portion of the wavefunction for each confined carrier is present in the barrier region. If these barriers are made sufficiently thin, the wavefunction of adjacent wells can overlap, resulting in a structure known as a superlattice [20]. A superlattice differs from isolated quantum wells in several ways. When a large number of wells are present, the discrete states of the quantum wells form bands, similar to the process of band formation from atomic states in the crystal lattice. The thin barriers also allow carriers to move between adjacent wells without having to acquire enough energy to pass over the barrier, a process is known as tunneling [21].

3.2.2. Quantum size effect

An important assumption when finding the energy levels in a quantum well or a superlattice is the envelope approximation [22]. The envelope approximation assumes that the properties of carriers in the quantum wells depends upon the variation in the one dimensional band potential of the materials in the direction of confinement and not the three dimensional crystal potential, which simplifies modeling of the quantum well. The approximation is reasonable for quantum well and superlattice structures that do not have any layers shorter than 20 Å, which applies to all of the structures in this dissertation.

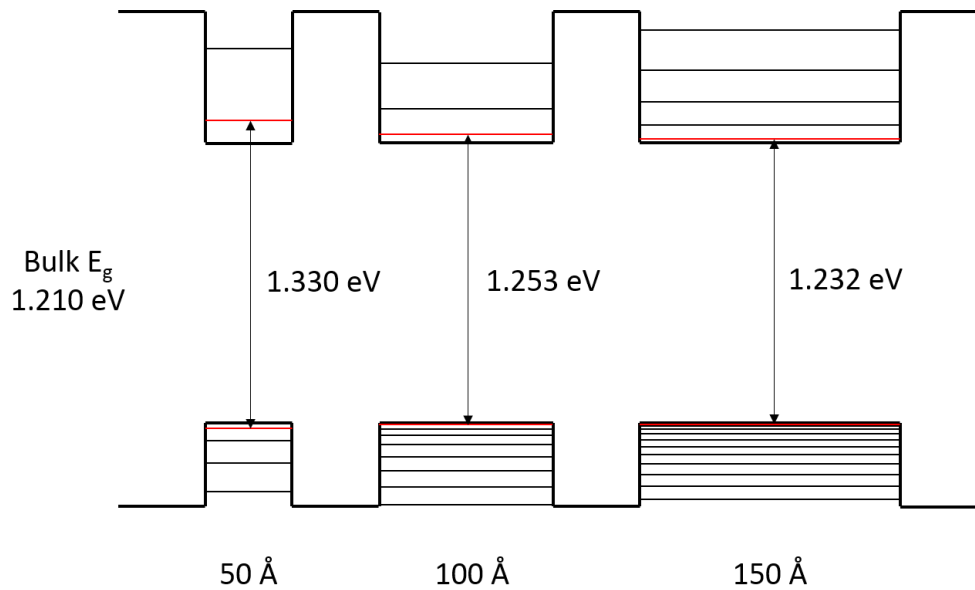


Figure 3.5: Demonstration of the quantum size effect in three $\text{In}_{0.15}\text{Ga}_{0.85}\text{As}$ quantum wells. The confined states for electrons and heavy holes are shown for each well, light hole states are omitted for simplicity. Thinner wells show more severe quantum size effects.

For a single quantum well, the energy states can be modeled using the classical solution for a particle in a finite well, which will be given fully in chapter 5. An important result of this model is that the lowest energy states for both the holes and electrons are higher than the envelope function energy. This lowest energy state increases as the well thickness or carrier effective mass decreases. As a result the effective band gap in a quantum well will be higher than that of the bulk material, a phenomenon known as the quantum size effect (QSE). This can be seen in figure 5, which shows the electron and heavy hole energy states for 50, 100 and 150 Å $\text{In}_{0.15}\text{Ga}_{0.85}\text{As}$ quantum wells with $\text{GaAs}_{0.25}\text{P}_{0.75}$ barriers. The increase in the bandgap from QSE is largely the result of the electron states due to the lower effective mass of electron in the InGaAs relative to heavy holes. The QSE is also more severe for thinner InGaAs wells for both holes and electrons.

3.2.3. Strained quantum wells and strain balanced superlattices and their application to multijunction solar cells

There are two methods for growing triple junction photovoltaic cells on Ge or GaAs substrates: 1) use subcells that are lattice matched to Ge, which results in a loss in efficiency due to poor current matching between cells or 2) use graded buffer layers to grow metamorphic materials which reduces, but does not eliminate, the defect density. Each of these methods, either fundamentally or in practice, limits the maximum efficiency that can be achieved from a triple junction cell. A method that incorporates non lattice matched semiconductors without the need for graded buffer layers could

potentially increase the efficiency of the triple junction cell. This can be done with the strained layer superlattice (SLS), also called the strain balanced superlattice (SBS) [23]. These structures can be added to either the GaAs or InGaP subcells which will reduce the absorption energy in the subcell and increase the current that can be generated by the multijunction cell.

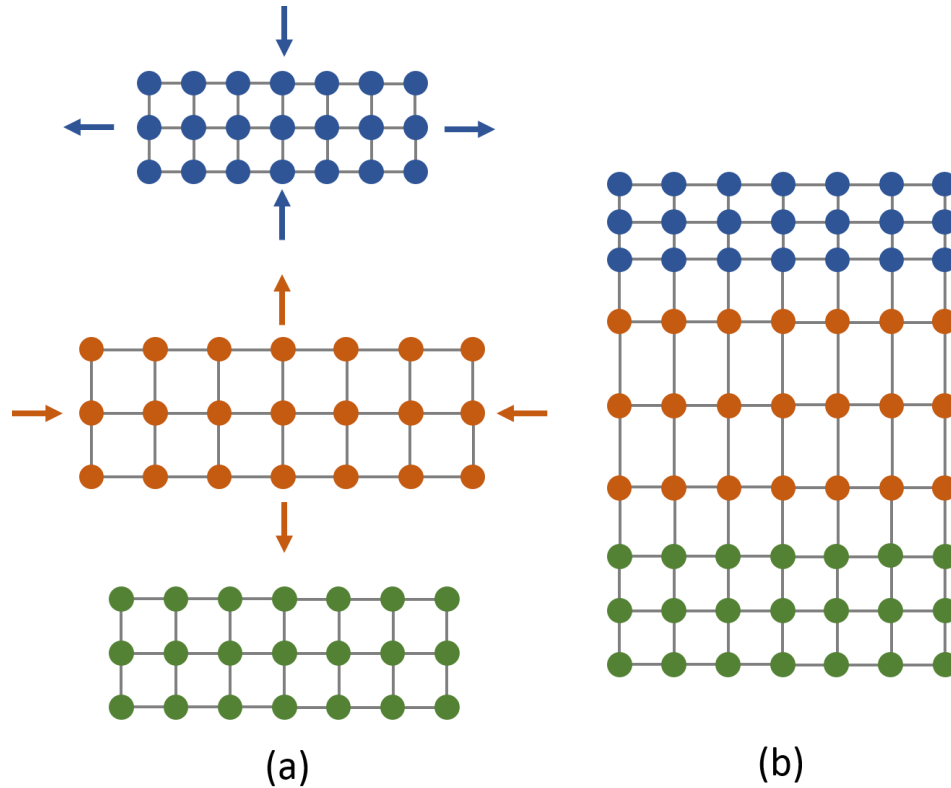


Figure 3.6: Demonstration of the strained superlattice concept with the substrate in green, the compressively strained material in orange and the tensilely strained material in blue. The distortion in the lattice constant for the strained layers in the plane of the substrate results in an opposite distortion in the perpendicular dimension.

The SLS is formed from two materials, one with a larger lattice constant than the substrate and another with a smaller lattice constant than the substrate, as shown in figure 6(a). When grown below the critical thickness, the two materials will become strained in order to match the lattice constant of the substrate. The lattice spacing of the larger lattice constant material will decrease, giving a compressively strained layer while the lattice spacing of the smaller lattice constant material will increase, giving a tensilely strained layer. This strain is biaxial and only occurs in the two directions parallel to the substrate surface. The third dimension will distort in the opposite direction (increase for compressive layers, decrease for tensile layers). This strained structure is shown in figure 6(b). If the thickness of the compressive and tensile layers are chosen properly, the total energy due to strain will be zero [24]. If the layer thicknesses are properly balanced, then the compressive/tensile pair can be

grown for as many periods as needed. Typically, the compressive layer will have a lower band gap than the tensile layer. As a result the strained layers will form a superlattice or multiple quantum well structure with the compressive layers as the well and the tensile layers as the barriers.

For the GaAs subcell the most common superlattice for absorption extension is composed of compressive InGaAs layers with tensile GaAsP layers. The InGaAs has a lower band gap than the GaAs and so forms the quantum wells in which absorption will occur. One design constraint arises due to the poor transport through the superlattice relative to bulk semiconductors. The superlattice must be placed in the high field region of the pn junction where carrier drift is the dominant transport mechanism [25]. In order to maximize the superlattice thickness, it is not doped and used as the intrinsic layer of a p-i-n structure. In order to maximize the efficiency of the multijunction cell the GaAs-SLS p-i-n subcell must balance the need for a low effective band gap in the wells, which requires InGaAs with a large InAs fraction and thick wells to minimize QSE, with the need for effective carrier transport and the strain balancing constraint.

3.3. Tunnel junctions

Tunnel junctions fulfill the need for a transparent, low resistance ohmic contact between the subcells of a multijunction solar cell structure [26]. They are formed when a pn junction is grown with highly doped n and p-type layers. Unlike a typical diode, they can conduct current at very low forward biases where they behave more like a resistor than a diode. The transparency requirement is important in multijunction structures as any absorption in the tunnel junction will reduce the efficiency of the cell. The growth of the tunnel junction between the top and middle cell is a particular issue as it is more difficult to achieve large doping levels in high band gap materials.

3.3.1. Origin of the tunnel junction

A tunnel junction, or tunnel diode, has a similar structure to the standard abrupt pn diode, the only difference being the very large doping levels ($>10^{19} \text{ cm}^{-3}$) in both the n-type and p-type layers near the junction. The high doping is required as the Fermi level must be within the conduction band of the n-type layer and the valence band of the p-type layer. Semiconductors with the Fermi level near or within the valence or conduction band edge are also known as degenerate semiconductors. In such cases the Boltzmann approximation is no longer valid and the full Fermi-Dirac distribution must be used when finding the band structure of the tunnel junction [27].

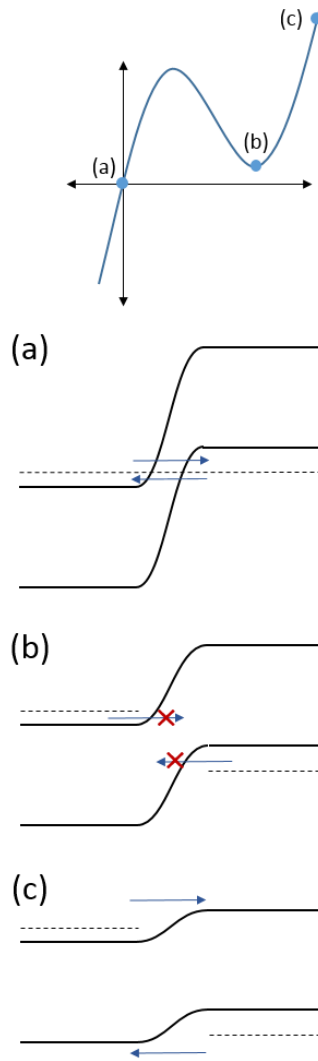


Figure 3.7: Tunnel diode mechanism: a) Degenerate doping in both the n and p sides creates a path for tunneling at low bias, b) as the bias increases direct tunneling becomes impossible and the current decreases to a minimum value and c) at a sufficiently large bias the junction behaves like a typical diode.

The I-V response and band structure of the tunnel junction and is shown in figure 3.7 [27]. Part (a) shows the band structure at zero bias. For energies between the conduction band edge of the n-type material and the valence band of the n-type material carrier can tunnel to the opposite band. 3.7(a) shows the secondary importance of the high doping levels, which is to minimize the tunneling distance since the tunneling probability will be strongly dependent on the distance that a carrier must tunnel. At zero bias, the tunneling current will be zero as there is no net tunneling in either direction in equilibrium. However with a small forward bias, the current increases rapidly eventually reaching the peak tunneling current (J_{pk}) which will occur at a particular voltage (V_{pk}). At a sufficiently large forward bias, the tunneling path between the valence and conduction bands will be cutoff (Fig.

3.7(b)), and the current will decrease to a minimum value. This minimum current does not decrease to zero since there is still some indirect tunneling mechanisms present. At larger forward biases the tunnel junction has the behavior of a typical pn junction.

3.3.2. Use of tunnel junctions in multijunction structures

In a multijunction structure the tunnel junctions are placed between individual subcells in order to prevent the formation of any parasitic diodes, the bottom layer of the tunnel junction must be the same type as the emitter of the lower cell while the top layer of the tunnel junction is the same type as the base of the upper cell. As a result, the tunnel junction will be biased in the opposite direction from the multijunction subcells. When a current is flowing through the multijunction structure, a small voltage will develop in each tunnel junction which will oppose the forward voltage, resulting in a small reduction in V_{oc} . A more serious issue occurs when the current exceeds J_{pk} of the tunnel junction. In this case the forward bias of the tunnel junction will increase significantly as the operational point will shift to point c in figure 3.7 and the efficiency of the cell will decrease dramatically [28]. As a result J_{pk} places a maximum limit on the solar concentration that can be used for a particular multijunction cell.

Low band gap semiconductors have two advantages when forming tunnel junctions. It is typically easier to dope low band gap semiconductors (GaAs) to higher levels than high band gap semiconductors (AlGaAs and InGaP), especially for n-type materials. Also, even for a given doping level the lower effective mass of carriers in GaAs relative to AlGaAs and InGaP will give a higher J_{pk} due to the strong mass dependence on the tunneling probability. This makes it difficult to form the high band gap tunnel junction with materials such as AlGaAs or InGaP, requiring the use of GaAs for multijunction cells that operate above $1000\times$ concentration. Since the GaAs will absorb light below 1.42 eV, the current generated in the middle cell will decrease, reducing the maximum efficiency. These GaAs layers in the TJ should be made as thin as possible in order to minimize the absorption [29].

Another factor arises from the growth of the top cell, which for InGaP is performed at temperatures above $650\text{ }^{\circ}\text{C}$ for growth times of 30 minutes or more. During this growth step, the dopants in the tunnel junction can diffuse into adjoining layers [30]. This can result in compensation in the adjacent p and n type layers or reduce the total doping due to outdiffusion when thin GaAs layers are used. As a result, dopants with very low diffusion coefficients such as C for p-type materials [31] and Se and Te for n-type materials [32] are used.

4. MOCVD and device and material characterization

4.1. Metal organic chemical vapor deposition

The technique used for the growth of both photovoltaic cell and tunnel junction cells was metal organic chemical vapor deposition (MOCVD). In MOCVD organometallic precursors which contain the desired element are delivered to a reactor using a carrier gas, typically hydrogen or nitrogen. These precursors are passed over a heated substrate, which results in the decomposition of the precursor and the growth of a crystalline material of a particular composition given the proper choice of pressure, temperature and precursor flow [1]. While MOCVD is uncommon in the production of silicon based electronics, it is extensively used in the production of III-V devices such as LEDs [2], solar cells [3] and photodetectors [4].

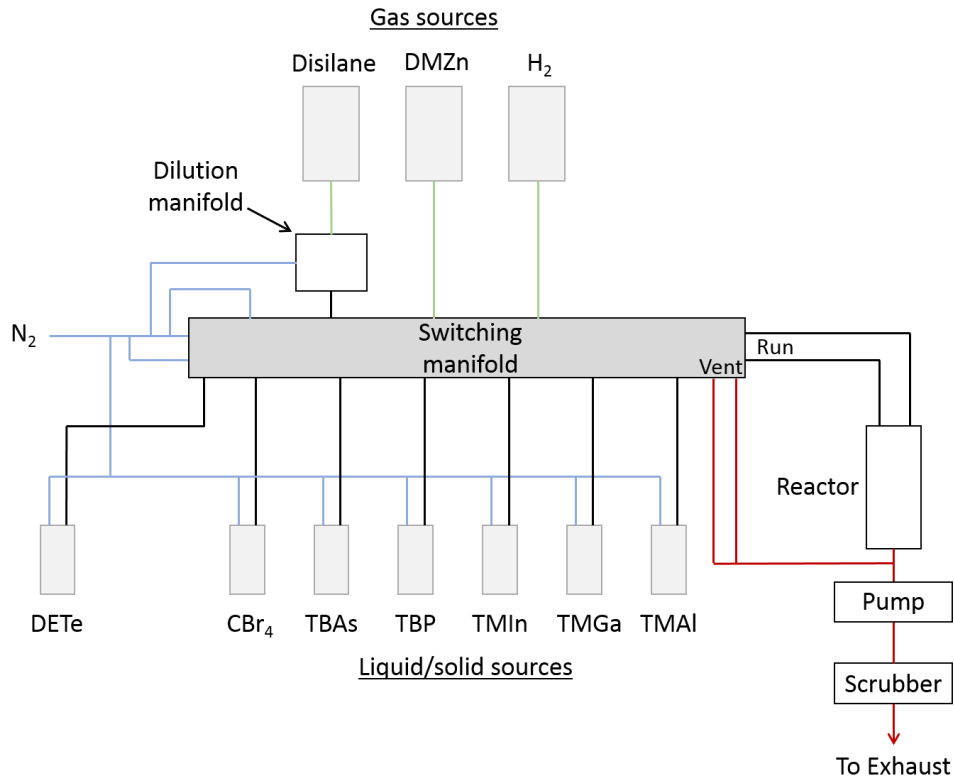


Figure 4.1: Functional schematic of the Thomas Swan reactor showing the layout of the major components. The blue lines are from the N₂ source, green lines are from the H₂ source or doping precursors dissolved in H₂ and the red lines are waste gases.

4.1.1. Components of MOCVD system

Due to the large number of precursor and gas sources, the structure of an MOCVD system can be very complicated. However it is possible to break the system into several important components which will be summarized here. The MOCVD system used for this dissertation is based on a commercial system created by Thomas Swan with several modifications made during the current project or by previous students in the laboratory. A basic schematic of the MOCVD system is shown in figure 1.

4.1.1.1. Bubblers and gas sources

In order to grow semiconductor materials with particular compositions and growth rates, it is necessary to introduce the metalorganic precursors into the growth chamber at a controllable flow rate. This can be done either by introducing the precursor as a premade gas solution or by forming the gas solution from liquid or solid sources.

Gas and solid sources are obtained from the manufacturers in stainless steel cylinders called bubblers. Two tubes feed into the bubbler: the inlet tube ends below the level of the liquid while the outlet tube begins above the liquid level. When a carrier gas flows through the bubbler, the liquid will become saturated with the precursor species with a partial pressure given by [5]:

$$\ln\left(\frac{P}{P_{ref}}\right) = -\frac{\Delta H_{vap}}{R}\left(\frac{1}{T} - \frac{1}{T_{ref}}\right) \quad 4.1$$

$$\ln(P_2) = B - \frac{A}{T_2}, \quad A = \frac{\Delta H_{vap}}{R}, \quad B = \ln(P_{ref}) + \frac{\Delta H_{vap}}{RT_{ref}} \quad 4.2$$

where ΔH_{vap} is the enthalpy of vaporization for the precursor and R is the gas constant. The parameters A and B in equation 4.2 are given by the bubbler manufacturers for each precursor in order to calculate the partial pressure of the over a range of temperatures. Since control of the bubbler temperature is important, recirculating chillers are used with a water/ethylene glycol mixture which can provide cooling down to -20 °C. The flow through the bubbler and the pressure in the bubbler are controlled using a mass flow controller (MFC) and a pressure controller respectively. The mass flow controller is placed at the inlet of the bubbler and is capable of controlling the flow within 5-95% of the maximum flow, which can vary from 10 standard cubic centimeters per minute to 5 standard liters per minute depending upon the source. The pressure controller is placed at the outlet of the bubbler and is generally not changed during normal operation.

The silicon and zinc precursors disilane and dimethyl zinc (DMZn) are used as gaseous solutions in hydrogen. Unlike the bubbler sources, the molar fraction of the gaseous precursors does not depend upon temperature, which limits the control of the molar flow to the dynamic range of the MFC. For this reason, a dilution manifold is used for the gas sources. This manifold uses two MFCs to control the flow of the precursor source and the nitrogen dilution. A needle valve in the exhaust line is used to control the pressure in the manifold.

A summary of the precursors used in this project is given in table 4.1.

Table 4.1: Summary of metalorganic precursors used in this work.

Precursor	Abbreviation	Purpose	Solid/liquid/gas
tert-Butylarsine	TBAs, TBA	group V source	liquid
tert-Butylphosphine	TBP	group V source	liquid
Trimethylaluminum	TMAI	group III source	liquid
Trimethylgallium	TMGa, TMG	group III source	liquid
Trimethylindium	TMIIn	group III source	solid
Carbon tetrabromide	CBr ₄	p-type dopant	liquid
Diethyltellurium	DETe	n-type dopant	liquid
Disilane	-	n-type dopant	gas
Dimethylzinc	DMZn	p-type dopant	gas

4.1.1.2. Vent/run manifold

While the bubbler manifolds control the flow rate of each precursor, it is also necessary to control whether or not a particular precursor is being fed into the reaction chamber at a particular time. This is particularly important during the growth of superlattices, which require the growth of semiconductor layers as thin as 30 Å with abrupt changes in composition.

The vent/run manifold introduces the carrier gas (in this case nitrogen) in four lines. There are two lines for both the group III and the group V precursors, one that runs to the growth chamber (the run line) and one that is fed directly into the exhaust (the vent line). The group III and group V precursors are handled separately to prevent gas phase reactions from occurring outside the growth chamber. The manifold is composed of a series of valves which allow each precursor to flow either to the run line or the vent line. Each manifold has one valve for hydrogen; hydrogen is necessary for the decomposition of the organometallic precursors before growth. Additionally, there are two makeup valves that flow

nitrogen. These are used to prevent pressure surges during the switching of precursors between the vent and run lines. This is particularly important for the switching of TMI_n during the superlattice growth.

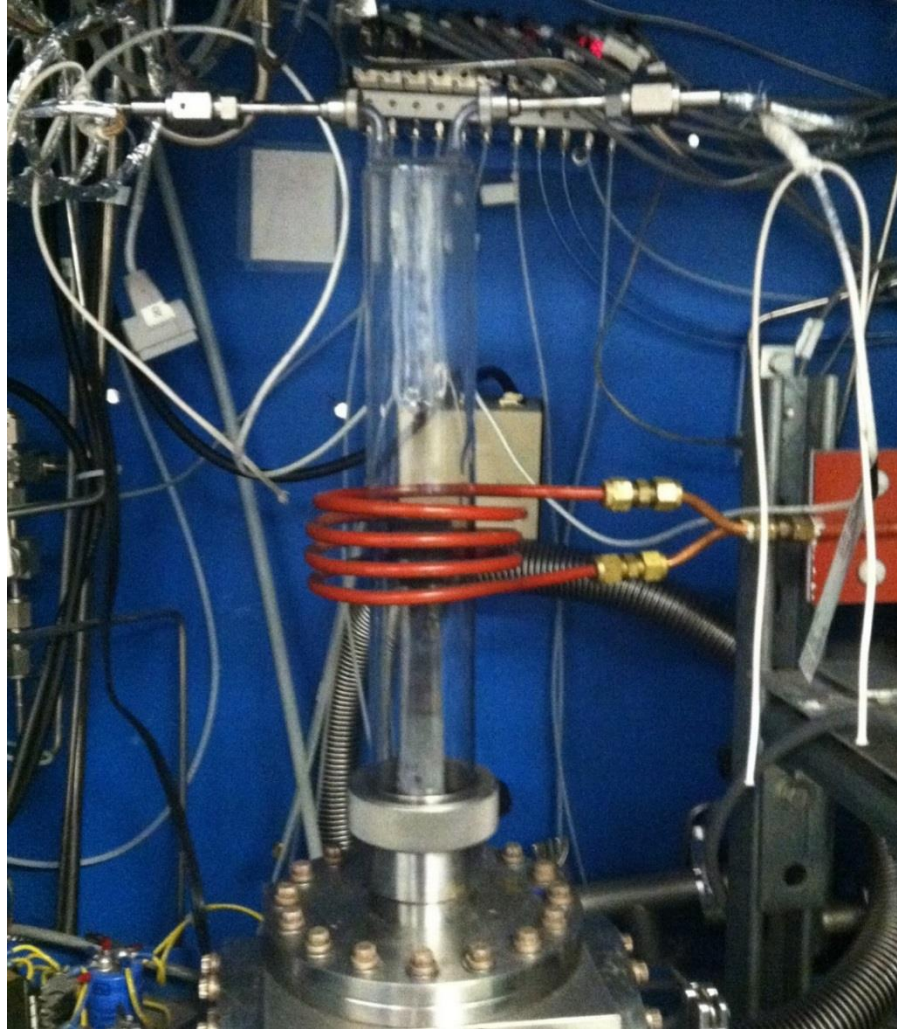


Figure 4.2: Photograph of the growth chamber attached to the MOCVD system. The two connections at the top of the chamber are used to introduce group III and V precursors as well as dopants and carrier gases. The exhaust flows from the larger opening at the bottom of the chamber. The red coil is the inductive heating solenoid.

4.1.1.3. Reactor

The growth reactor is custom built glass chamber, as shown in figure 2. The diameter of the chamber is 5 cm and the length is 32 cm, which is smaller than most commercially available reactors. The small inlet tubes on the top of the chamber allow for the introduction of group III and group V precursors. A glass separator is included between the two inlet lines to prevent gas phase reactions. The GaAs substrates are placed on a SiC coated graphite susceptor which is rotated at 167 rpm during

growth. A 7500 W Ameritherm inductive power source is capable of heating the susceptor to temperatures as high as 900 °C. Waste gases flow to the bottom of the chamber and is processed by the gas system.

4.1.1.4. Exhaust system

The exhaust system controls the pressure in the growth chamber and removes unused precursors and waste from the growth process. An Alcatel 2033 rotary vane pump and an MKS Type 653B exhaust throttle valve is used to control the pressure in the reaction chamber. Growth is typically carried out at 200 torr in order to reduce gas phase reactions that are more frequent at higher pressure.

The first component after the pump is a 400 °C pyrolysis furnace which is used to decompose any unused precursors from the vent waste. This is followed by a particle filter to remove any solid waste products. Most of the waste components are innocuous when converted into unreactive products, however arsenic containing compounds are toxic in any form. A Novapure S200 effluent gas scrubber is used to remove any arsenic containing products by passing the exhaust through an absorptive resin. These products must be periodically oxidized by passing dry air through the scrubber.

4.1.2. Substrate preparation

The GaAs substrates are purchased as 2 inch or 3 inch wafers with a thickness of 350 µm. They are either undoped, doped p-type with Zn or doped n-type with Si. Due to the shape of the growth reactor and susceptor, a 14 mm by 14 mm square must be cleaved using a diamond scribe. The cleaving process introduces particles and other contaminants which are removed through the following procedure.

1. Rinse in isopropanol followed by hexanes
2. Sonicate for 2 minutes
3. Rinse in acetone, isopropanol and methanol
4. Sonicate for 2 minute
5. Rinse 10 times with DI water
6. 2 minute metal removal with concentrated sulfuric acid
7. Rinse 10 times with DI water
8. 30 second etch with 5:1:1 solution of water/aqueous ammonia/hydrogen peroxide
9. Rinse 10 times with DI water
10. 1 minute oxide removal with hydrochloric acid
11. Rinse 10 times with DI water

12. Remove water with nitrogen gun, and load onto susceptor

Once the sample is loaded, the growth chamber is attached to the vent and group III and group V lines.

4.1.3. MOCVD growth

Once the sample is cleaned and loaded, the epitaxial growth can proceed. The growth procedures are controlled with software provided by Thomas Swan. The software can control the pressure in the reactor, the susceptor temperature and the flow and vent/run valve setting of each source line. The particular growth process will vary between samples, but there are several steps that are common to each run.

4.1.3.1. Purge and bake out

Before growth can proceed it is necessary to remove any oxygen or water vapor that remains in the growth chamber from the loading process. The first step in any run is a pump/purge cycle where the throttle valve on the pump is cycled between 1 torr and 400 torr. During the purge cycle the chamber is backfilled with nitrogen gas. A similar cycle occurs at the end of the run to remove toxic gases that may still be present in the chamber. The initial pump/purge is followed by a 900 second purge at 200 torr.

After the purge, the GaAs surface still contains arsenic oxides which can interfere with the growth process. These oxides can be removed by baking the substrate at 700 °C for 5 minutes. At this temperature the arsenic is more volatile than the gallium and will evaporate leaving gallium droplets on the surface of the substrate. It is necessary to flow an overpressure of TBAs in order to balance the evaporation and deposition of arsenic on the surface [6]. The temperature is lowered to 640 °C before growth is initiated.

4.1.3.2. Nucleation

For all the structures grown in this work, the growth should occur at a constant rate at all locations on the surface to produce a flat, two dimensional surface. The growth of three dimensional structures can lead to defect formation and decreased device performance.

The substrates used in this work are oriented in the (100) direction but are tilted, or offcut, 2° in the (110) direction. This produces a series of steps on the growth surface that are important for the growth process since they provide locations for atoms to nucleate uniformly across the surface [7].

During nucleation the TMGa is introduced with a low growth rate (1 \AA/s) for five minutes along with any necessary dopant precursor. After the nucleation growth can proceed to the desired structure.

4.1.3.3. Growth

There were two broad categories of structures grown in the MOCVD reactor: samples for material calibration and electrical devices. Material calibration includes compositional calibration of ternary semiconductors, doping calibrations and isolated superlattice structures. Electrical devices include photovoltaic cells and tunnel diode structures.

Before electrical devices can be grown, it is necessary to perform material calibrations in order to develop growth procedures for each material present in the device. The only binary semiconductor used is GaAs, for each of the ternary semiconductors used it is necessary to calibrate the material composition. This included calibrations for AlGaAs, InGaAs, GaAsP and InGaP. The temperature, growth rate and relative precursor flows were varied in order to give a material with a smooth growth surface and the proper composition. The growth morphology was determined using a stereoscopic microscope immediately after growth and the material composition was found using x-ray diffraction. A similar procedure was carried out for doping calibrations, which used tellurium and silicon as n-type dopants and carbon and zinc as p-type dopants. The active dopant concentration was determined using Hall effect measurements. For the superlattice structures alternating layers of InGaAs and GaAsP were grown using the calibrated compositions for the two materials. Calibrations for the superlattice structures was carried out with Joshua Samberg; the results of these experiments are given in his dissertation. The doping calibrations for the tunnel junction structures are given in chapter 7.

Once the material calibrations are complete, the next step is to grow electrical devices. The device structure for the superlattice photovoltaic cells and the tunnel junctions are shown in figure 3. Standard GaAs cells were also grown; these used the same structure as shown in fig. 3(a) but did not include the undoped superlattice region. The MOCVD reactor was also used to simulate top cell growth for the tunnel junction structures. This was carried out by heating the previously grown device, or a portion of the device, at temperatures between 650 and 700 °C. TBAs was also flowed into the reactor to prevent the formation of gallium droplets during this process.

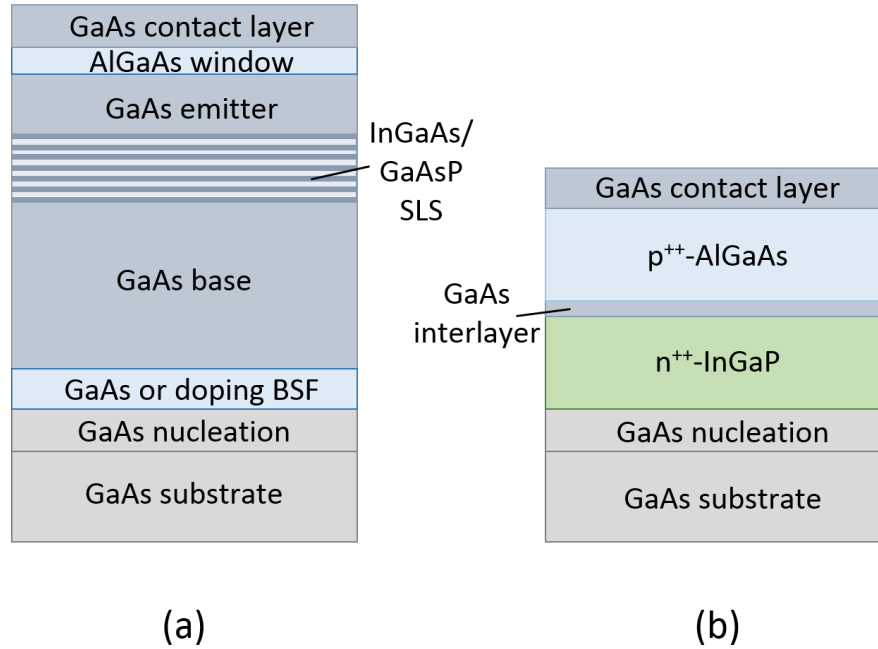


Figure 4.3: Schematics for the (a) GaAs-SLS photovoltaics cell and (b) InGaP/AlGaAs tunnel junction. The doping for the PV cell is not shown as the structure was grown in both the p on n and n on p configuration.

4.2. Device and material characterization

Several analytical techniques were used to analyze calibration and device samples. X-ray diffraction and photoluminescence can be carried out immediately after sample growth while the Hall effect measurements required minor sample processing. The IV response and external quantum efficiency measurements require full device processing using standard fabrication techniques.

4.2.1. Hall effect characterization

Hall effect measurements can give the doping concentration, doping type, mobility and sheet resistance for an epitaxial materials of known thickness [8]. Hall effect measurements were carried out on films grown on semi-insulating substrates in order to limit conduction to the epitaxial layer. Growth samples were typically cleaved into 5 mm × 5 mm squares, but smaller or larger portions were also fabricated.

The measurements were carried out on a custom built instrument using the van der Pauw method [9]. Contacts to the GaAs top layer were made with indium that was then annealed at 400 °C under nitrogen ambient. For non-GaAs calibrations, a GaAs was still used in order to form reliable contacts. For these samples the GaAs was removed by a wet etch so that the cap did not interfere with the

measurement. For AlGaAs samples the cap was removed with a citric acid/hydrogen peroxide etch while the InGaP samples an ammonia/peroxide etch was used.

4.2.2. X-ray diffraction

X-ray diffraction (XRD) was used to determine the composition of ternary semiconductor materials and to characterize superlattice structures. The diffraction angle, θ , from a crystal plane by and x-ray with the wavelength, λ , is related to the distance between the planes, d , by the Bragg relation [10]

$$2d \sin \theta = n\lambda \quad 4.3$$

where n is a positive integer. For the (400) plane d is equal to one-half of the lattice constant and has a first order Bragg angle of 33.02° for GaAs. This peak can be used as a reference for all XRD measurements as GaAs is present in all samples as the substrate. For epitaxial materials with a lattice constant different than that of GaAs, a second peak is present at an angle that is a function of the material composition. The position of this peak can be used to determine the composition of InGaAs, GaAsP, AlGaAs layers and to determine if InGaP layers are lattice matched to the GaAs substrate.

For superlattices, multiple peaks are present in the vicinity of the GaAs substrate peak. This is due to Bragg diffraction from the superlattice, but with a closer spacing between the higher order peaks due to the superlattice period, Λ , being much larger crystal lattice constant. The average spacing of these peaks, $\delta\theta$, can be used to find the superlattice period [11]:

$$\Lambda = \frac{\lambda}{2(\cos \theta)\delta\theta} \quad 4.4$$

Where θ is the angle of the GaAs substrate peak. If the growth rate and composition of superlattice is known, the thickness of the individual layers can be found from the period. XRD is also useful for stress balancing as the $m=0$ peak should be slightly to the left of the substrate peak in balanced systems. The particular position of the $m=0$ peak depends upon the composition of the InGaAs and GaAsP layers. It is not coincident with the substrate peak due to the different elastic parameters of the two superlattice components.

Measurements were carried out on a Rigaku Geigerflex single crystal diffractometer and a Philips X'Pert PANalytical triple crystal diffractometer using Cu $K\alpha$ sources. The triple crystal diffractometer included a Ge monochromator to select only the Cu $K\alpha_1$ emission and was used when a higher resolution was needed to identify closely spaced diffraction peaks.

4.2.3. Photoluminescence

Photoluminescence (PL) is a technique that measures the light emitted from a sample excited by another light source. It can be used in conjunction with XRD to determine the band gap, and hence composition of bulk semiconductor materials. It can also be used to determine the effective band gap in two dimensional structures, like quantum wells and superlattices, which are subject to quantum confinement effects. Since the PL intensity is due to radiative recombination of excited carriers it gives an indication of the material quality as a small nonradiative recombination lifetime will result in a weak PL intensity.

The PL excitation source was a frequency doubled Nd:YAG laser pumped by a GaAs diode laser to give a output wavelength of 532 nm. A chopper/lock-in amplifier system was used to minimize interference from external light sources. In order to minimize the effect of surface recombination a high band gap blocking layer, typically AlGaAs, was grown near the surface of each PL sample.

4.2.4. Light JV response

Chapter 2 introduced V_{oc} , J_{sc} and fill factor as metrics for photovoltaic cell performance. The illumination for these measurements was provided by an Oriel 1000W solar simulator. The simulator used a xenon arc lamp to generate the 5800 K blackbody spectrum and an AM1.5G filter was used to simulate atmospheric absorption. A GaAs standard cell with a known J_{sc} was used to calibrate the power output of the solar simulator to 1 sun concentration. The JV response was found using a four wire probe measurement of the PV cells with a Keithley 2400 sourcemeter.

Dark current measurements were carried out using the same methods as the light measurements, but without the solar simulator. These were performed both for the PV cells and the TJ devices. The Keithley 2400 sourcemeter is capable of measuring currents as high as 1 A which was sufficient for the highest peak tunneling currents in the TJ devices.

4.2.5. External quantum efficiency

The external quantum efficiency (EQE) is the ratio between the number of charge carriers collected by the solar cell and the number of photons incident upon the cell. The EQE will vary as a function of the wavelength of the incident light. It can be used to evaluate the performance of each layer in the PV structure. A more thorough analysis of EQE is given in chapter 6.

The EQE measurements were carried out using a Newport ¼m monochromator as the illumination source. The monochromator output was varied between 300 and 1100 nanometers. A chopper and

lock-in amplifier were used to reduce noise. Calibration of the monochromator output was carried out using a silicon photodiode reference with a known EQE.

5. Quantum well structures: Modeling and experiment

5.1. Modeling of quantum well states

5.1.1. Kronig-Penny model for superlattices

Chapter 3 introduced the concept of quantum wells and superlattices. There it was shown that the electrons and holes in alternating layers of semiconductor materials can be treated separately from the crystal wavefunction so that the energy states in a superlattice or quantum well will depend upon the band structure of the semiconductor materials instead. This assumption is known as the envelope function approximation and is valuable for analyzing quantum wells and superlattices as it transforms the calculation of band state energies of a superlattice or quantum well from a three dimensional problem into a one dimensional problem [1]. Using the envelope approximation, the energy states in a single well can be found either from the infinite well model, or more accurately, from the finite well model. These models work well for a single quantum well or for a series of quantum wells that are sufficiently separated so that the wavefunction from one well does not have a significant overlap in neighboring wells. However, for the InGaAs wells that are used in the solar cells structures, the thickness of the GaAsP barriers varies from 20 to 40 Å, thin enough for overlap of the wavefunction between adjacent wells. Instead, the quantum wells should be treated as a periodic superlattice structure and the subband energy levels in the wells can be found using a modified Kronig-Penny model that can be used for an arbitrary periodic structure.

The two primary assumptions that are made when calculating the conduction and valence band energies are the previously mentioned envelope function approximation and the effective mass approximation. The latter assumes that the electron (or hole) can be treated as a free electron with an effective mass that will depend upon the particular material. These assumptions are given in the general expression for the Schrödinger equation for the wavefunction, ψ , a one dimensional quantum structure [2]:

$$-\frac{\hbar^2}{2m^*(z)} \frac{d^2\psi}{dz^2} + V_z(z) = E_z\psi \quad 5.1$$

It can be seen that the effective mass, m^* , and the band potential, V_z , are a function of the dimension z , which is also the direction of crystal growth for the InGaAs/GaAsP superlattices.

There are two ways to express V_z for the InGaAs/GaAsP structure, which are shown in figure 1. Figure 5.1(a) represents a single quantum well of length L_{qw} , cladded with a barrier material at a potential higher by the quantity V_0 . The superlattice in figure 5.1 (b) has the same well structure, but

instead of a single well with infinitely thick barrier layers it consists of an infinite number of wells separated by a barrier of thickness L_b .

The solution to eq. 5.1 has the same form for both the quantum well and the superlattice. In the well, ψ is given by:

$$\psi_w(z) = A \sin(k_w z) + B \cos(k_w z) \quad 5.2$$

where k_w is the wave vector in the well and has the form:

$$k_w = \sqrt{\frac{2m_w^* E}{\hbar^2}} \quad 5.3$$

Where E is the energy relative to the bottom of the well. A similar expression can be written for the barrier region:

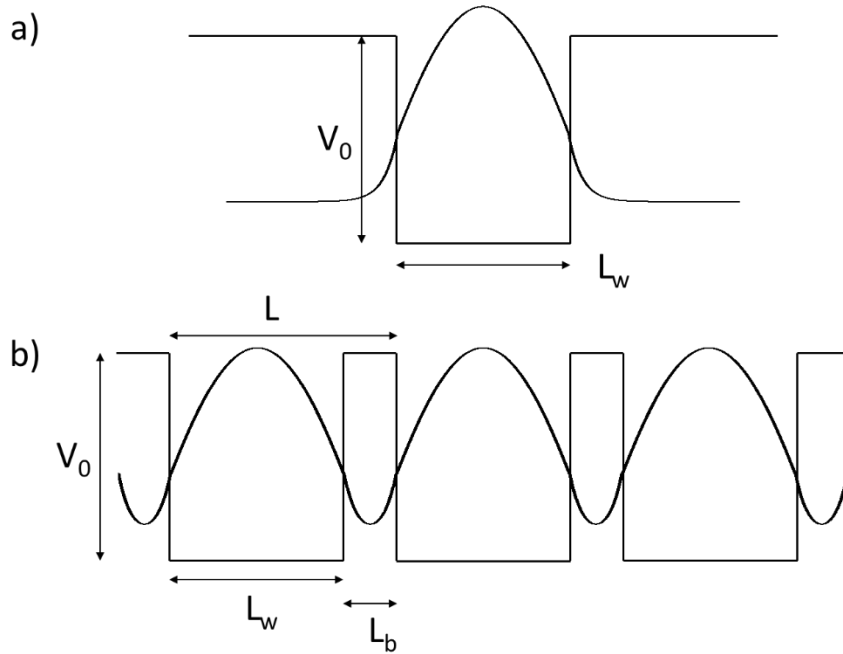


Figure 5.1: Wavefunction of the lowest energy state of an electron in a) quantum well and b) superlattice

$$\psi_b(z) = C' \sin(k_b z) + D' \cos(k_b z) \quad 5.4$$

with k_b given as:

$$k_b = \sqrt{\frac{2m_b^*(E - qV_0)}{\hbar^2}} \quad 5.5$$

When $E < V_0$, k_b will be imaginary so eqns. 5.3 and 5.4 can be rewritten as:

$$\psi_b(z) = Ce^{\kappa_b z} + De^{-\kappa_b z}, \kappa_b = \sqrt{\frac{2m_b^*(qV_0 - E)}{\hbar^2}} \quad 5.6$$

The appropriate boundary conditions are required in order to find the constants A, B, C and D. The first two are common between the quantum well and the superlattice. The wavefunction and probability current must be continuous, so at some interface point z_i , the boundary conditions are [3]:

$$\psi_w(z_i) = \psi_b(z_i) \quad 5.7$$

$$\frac{1}{m_w^*} \frac{\partial}{\partial x} \psi_w(z_i) = \frac{\partial}{m_b^*} \frac{\partial}{\partial x} \psi_b(z_i) \quad 5.8$$

The third boundary condition is what distinguishes the quantum well and the superlattice. For a quantum well the normalization condition requires that the wavefunction be bounded at infinity.

$$\lim_{z \rightarrow \pm\infty} \psi_b(z_i) = 0 \quad 5.9$$

On the other hand, the superlattice has a periodic boundary condition since the potential is repeated over the period $L=L_w+L_b$ [4].

$$\psi(z + L) = \psi(z)e^{iqL} \quad 5.10$$

q is the wavevector for the superlattice, which is periodic over the interval from $-\pi/L$ to π/L . This means that a superlattice will form bands rather than the discrete states found in quantum wells. It will be shown that these bands are very narrow for typical InGaAs/GaAsP superlattices, especially for the lowest energy states in the quantum well, which means that the methods for obtaining the energy states in superlattices will also apply to quantum wells.

Consider a quantum well structure with a 100 Å In_{0.15}Ga_{0.85}As wells cladded with GaAs_{0.25}P_{0.75}. The effective mass is 0.060 m_0 and 0.114 m_0 in the InGaAs and GaAsP respectively and the conduction band offset between the two materials is 563 meV [5]. Applying the boundary conditions in eqns 5.7, 5.8 and 5.9 gives two transcendental equations for the confined energy states:

$$\frac{k_w}{m_w^*} \tan\left(\frac{k_w L}{2}\right) = \frac{\kappa_b}{m_b^*} \quad 5.11$$

$$\frac{k_w}{m_w^*} \cot\left(\frac{k_w L}{2}\right) = -\frac{\kappa_b}{m_b^*} \quad 5.12$$

Eqn 5.11 gives the solutions with odd symmetry while 5.12 gives the solutions with even symmetry. For this particular quantum well structure there are three confined states in the conduction band at 37.4, 151.3 and 342.3 meV.

The superlattice energy states can be found by using the boundary conditions in eqns 5.7, 5.8 and 5.10 to give the well-known Kronig-Penney equation [6]. This gives a dispersion relationship in terms of the superlattice wavevector, q , rather than the discrete energy levels of the quantum well.

$$\cos(qL) = \cos(k_w L_w) \cosh(\kappa_b L_b) - \left(\frac{\kappa_w m_b^*}{\kappa_b m_w^*} - \frac{\kappa_b m_w^*}{\kappa_w m_b^*} \right) \sin(k_w L_w) \sinh(\kappa_b L_b) \quad 5.13$$

In order for the $\cos(qL)$ term to give real values, the right hand side of eqn 5.13 is limited to values between -1 and 1. The superlattice forms bands defined by the one dimensional wavevector q . These are typically referred to as minibands to distinguish them from the three dimensional band structure of the crystal lattice.

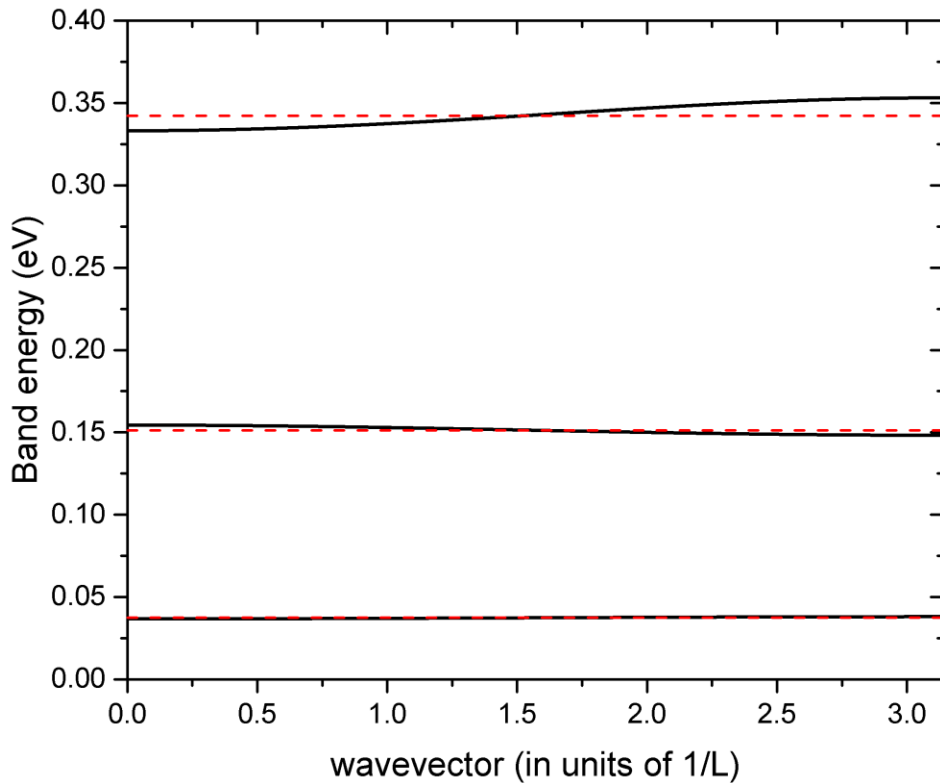


Figure 5.2: E-q dispersion of a 100 Å $\text{In}_{0.15}\text{Ga}_{0.85}\text{As}$ / 30 Å $\text{GaAs}_{0.25}\text{P}_{0.75}$ superlattice (red) with the energy states of an equivalent isolated quantum well (black).

The superlattice dispersion was calculated for an infinitely periodic structure of 100 Å $\text{In}_{0.15}\text{Ga}_{0.85}\text{As}$ and 30 Å $\text{GaAs}_{0.25}\text{P}_{0.75}$. This structure has the same dimensions and material composition as the quantum well given above. Figure 5.2 shows the superlattice dispersion relationship along with the discrete energy of the corresponding quantum well states. There are two features of figure 5.2 that should be emphasized. First, the quantum well energy state passes through the center of each superlattice miniband. Second, the minibands are very narrow, especially for the lowest energy state.

For the quantum well/superlattice in figure 2, the quantum well state is at 37.4 meV while the bottom of the superlattice miniband is at 36.8 meV, a difference of less than 1 meV. Thus, the eqns. 5.11 and 5.12 can be used interchangeably with eqn. 5.13 in order to calculate the absorption edge for superlattice devices. While the results are given for the conduction band, the eqns. 5.11-13 apply to the valence band as well. For the valence band separate states exist for the heavy holes and light holes with the heavy holes being at lower energies due to the larger heavy hole mass. This means that the lowest energy transition in the wells will be between the electron and heavy hole states.

5.1.2. Effect of strain on energy states in quantum wells

In a strain-balanced InGaAs/GaAsP grown on GaAs, each InGaAs layer will be compressively strained while each GaAsP layer is under tensile strain. As a result, the cubic lattice of each material undergoes a tetragonal distortion with biaxial strain in perpendicular to the growth direction (x and y axis) and uniaxial strain in the growth direction (z axis). The compressive strain in the InGaAs results in a reduction of the crystal lattice spacing in the growth direction while the opposite occurs for the tensile GaAsP, with an increase in the lattice spacing in the growth direction. Since the band structure of a material is the result of the symmetry and dimensions of the crystal lattice, it is expected that the band gap and band structure will be altered by the tetragonal distortion of the lattice.

Figure 5.3 shows the band structure for an unstrained material and the same semiconductor under compressive and tensile strain. The strain has two effects on the band gap. The first is a change in the relative energy of the conduction and valence band energy. The magnitude of this difference depends upon the strain, ϵ , the elastic stiffness coefficients, C_{11} and C_{12} , and the hydrostatic deformation potential, a , all of which will depend upon the composition of the strained layer [7].

$$\Delta E = -2a \left(\frac{C_{11} - C_{12}}{C_{11}} \right) \epsilon \quad 5.14$$

This will result in a larger band gap for a material under compressive strain and a smaller band gap for a material under tensile strain.

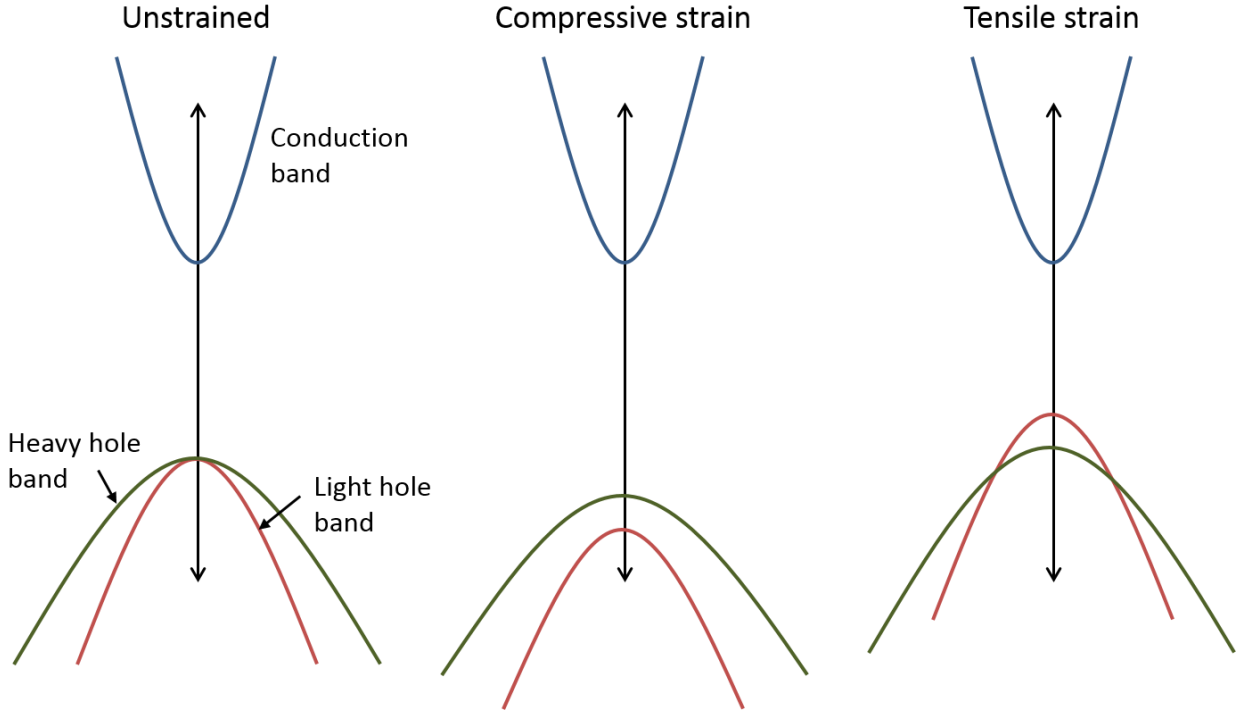


Figure 5.3: Schematic showing the effect of compressive and tensile strain on the band structure around $k=0$

The second effect is the splitting of the heavy hole and light hole degeneracy. For a compressive material the heavy hole will move to a higher energy while for a tensile material the light hole will be at a higher energy. The magnitude of this splitting depends upon the shear deformation potential, b [6]:

$$\Delta E_{hh} = b \left(\frac{c_{11} + 2c_{12}}{c_{11}} \right) \varepsilon \quad \Delta E_{lh} = -b \left(\frac{c_{11} + 2c_{12}}{c_{11}} \right) \varepsilon \quad 5.15$$

The effective band gap for $\text{In}_x\text{Ga}_{1-x}\text{As}$ with $x < 0.5$ is shown in figure 5.4 for the unstrained material and strained heavy and light hole bands. This gives the band gap for a thick InGaAs layer in the absence of quantum confinement. The elastic stiffness coefficients and deformation potentials were calculated using a linear interpolation of the published values for InAs and GaAs [8]. As a result of the compressive strain in the InGaAs, the extension of the absorption in superlattice solar cells will be less than what would be found in a bulk InGaAs cell, but this is largely unavoidable since strained layers are required to avoid the formation of defects. It can be seen from figure 5.4 that the band gap decreases monotonically with an increasing indium fraction, meaning that there is no optimal indium composition for minimizing the band gap under strain.

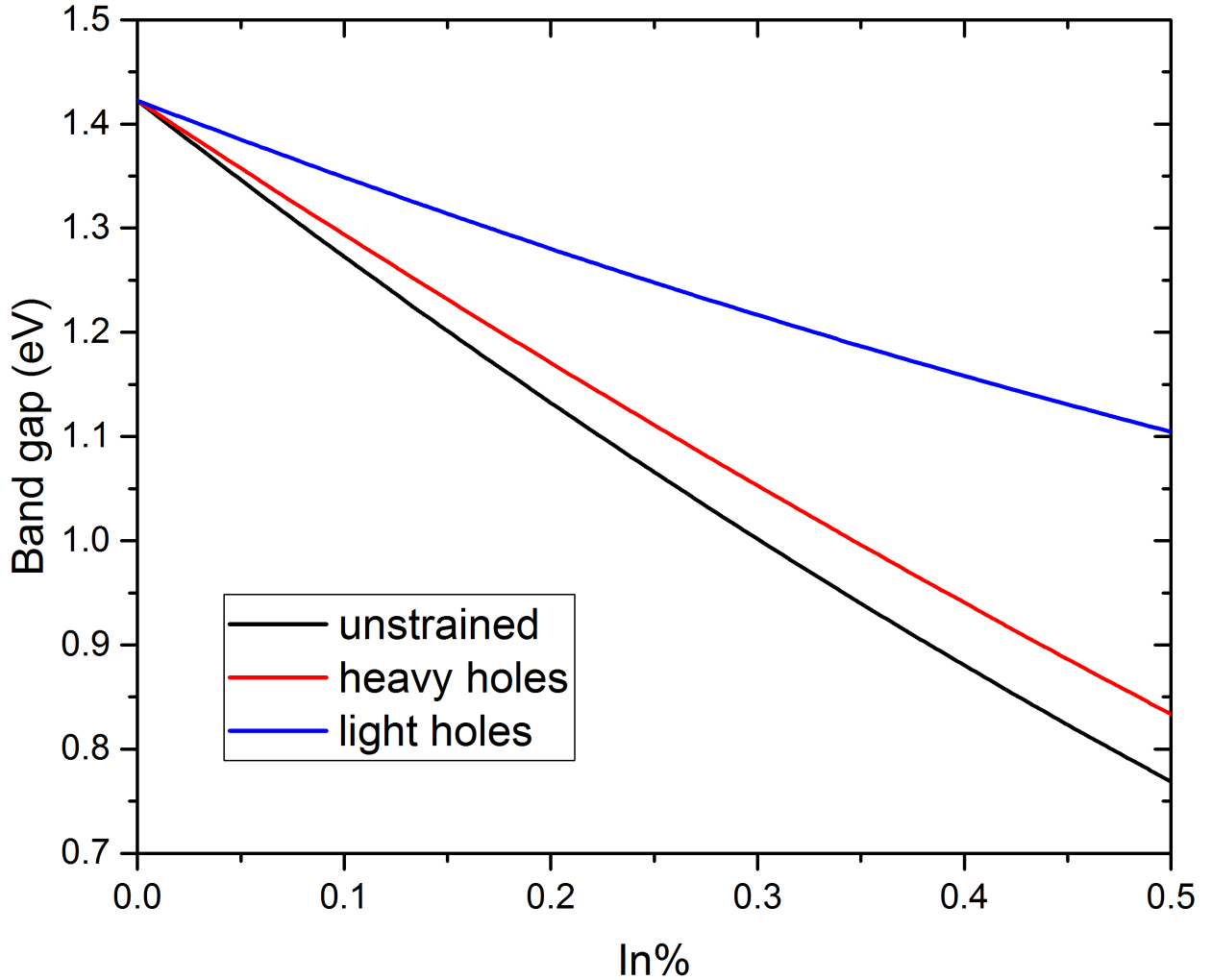


Figure 5.4: Effect of strain on the band gap of $\text{In}_x\text{Ga}_{1-x}\text{As}$ for $x < 0.5$

Figure 5.5 shows the effective band gap for $\text{GaAs}_{1-y}\text{P}_y$ for $y > 0.5$, which is the region over which the band gap is determined by the X band. The GaAsP band gap has less of an effect on the absorption band edge, but is still necessary in order to find the energy of the confined states in the InGaAs wells. For compositions with $y > 0.5$, GaAsP is an indirect band gap material with the conduction band minimum corresponding to the X band. There has been little research into measuring the hydrostatic deformation potential for the X band of either GaP or GaAs. Theoretical models for these two materials have found that the sign of the deformation potential is opposite that of the direct band material meaning that the tensilely strained GaAsP will actually have a smaller band gap than the unstrained material [9]. However, the magnitude of the deformation potential is small and will not have a major impact on the energy levels in the quantum well.

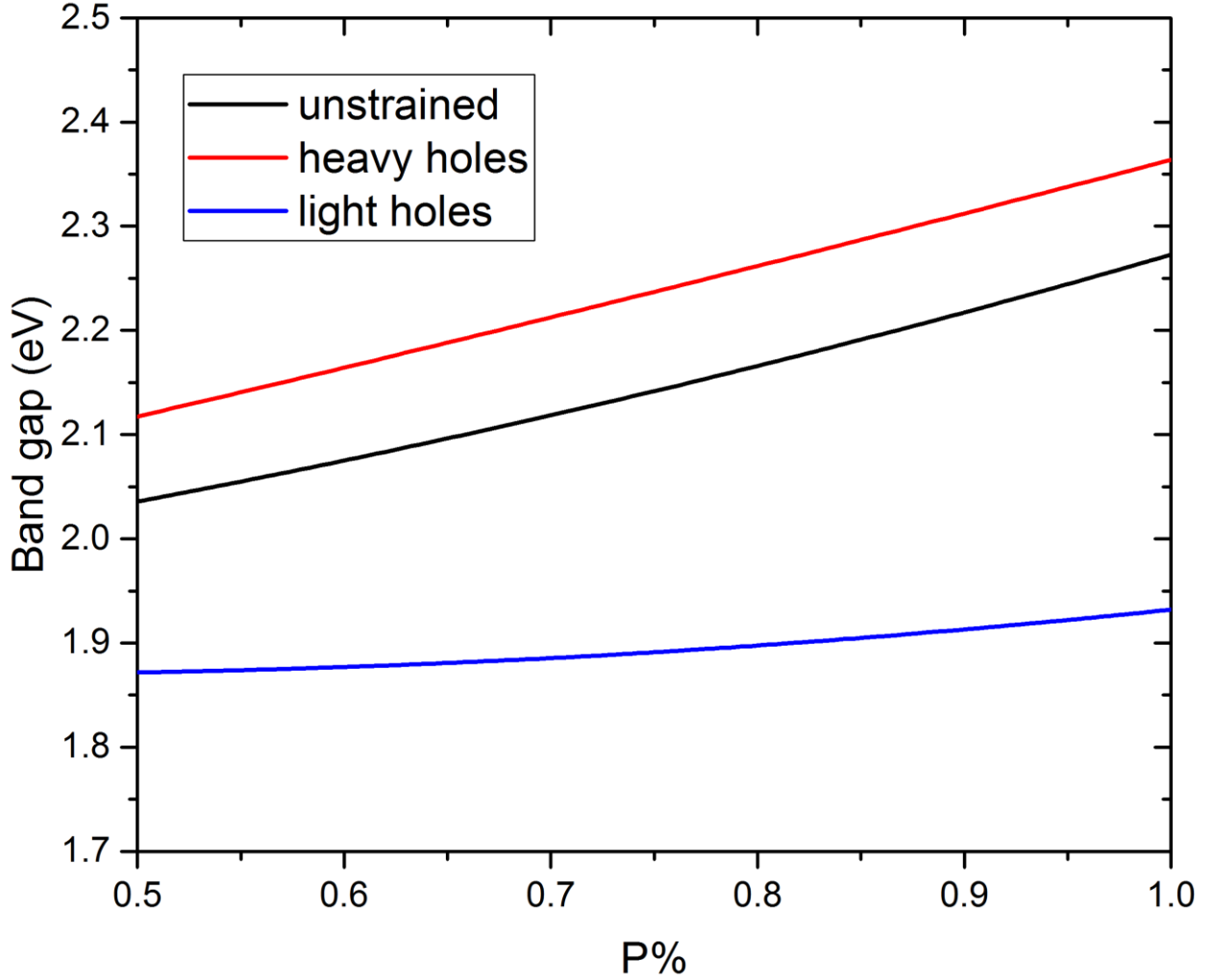


Figure 5.5: Effect of strain on the band gap of GaAs_{1-y}P_y for y>0.5. The minimum band gap is the X band of the conduction band for all compositions within the given range.

5.1.3. Modified Kronig-Penny model for non-abrupt interfaces

Figure 5.6 shows the effective band gap in InGaAs wells as a function of well thickness. The effective band gap is defined as:

$$E_{g,eff} = E_{g,bulk} + \Delta E_{hh} + \Delta E_e \quad 5.16$$

Where ΔE_{hh} and ΔE_e are the n=1 states as found from eqn. 5.13, including the effects of strain. In every case the barrier is composed of GaAs_{0.25}P_{0.75} that is 30 Å thick. By calculating $E_{g,eff}$ as a function of barrier thickness, it was found that the barrier thickness only begins to affect the effective band gap when it is on the order of 10 Å or less. The thinnest GaAsP that was grown in actual

superlattices was 25 Å. The GaAsP thickness will affect strain balancing and tunneling, but the barrier thickness is not of any practical concern for modeling the well energy states.

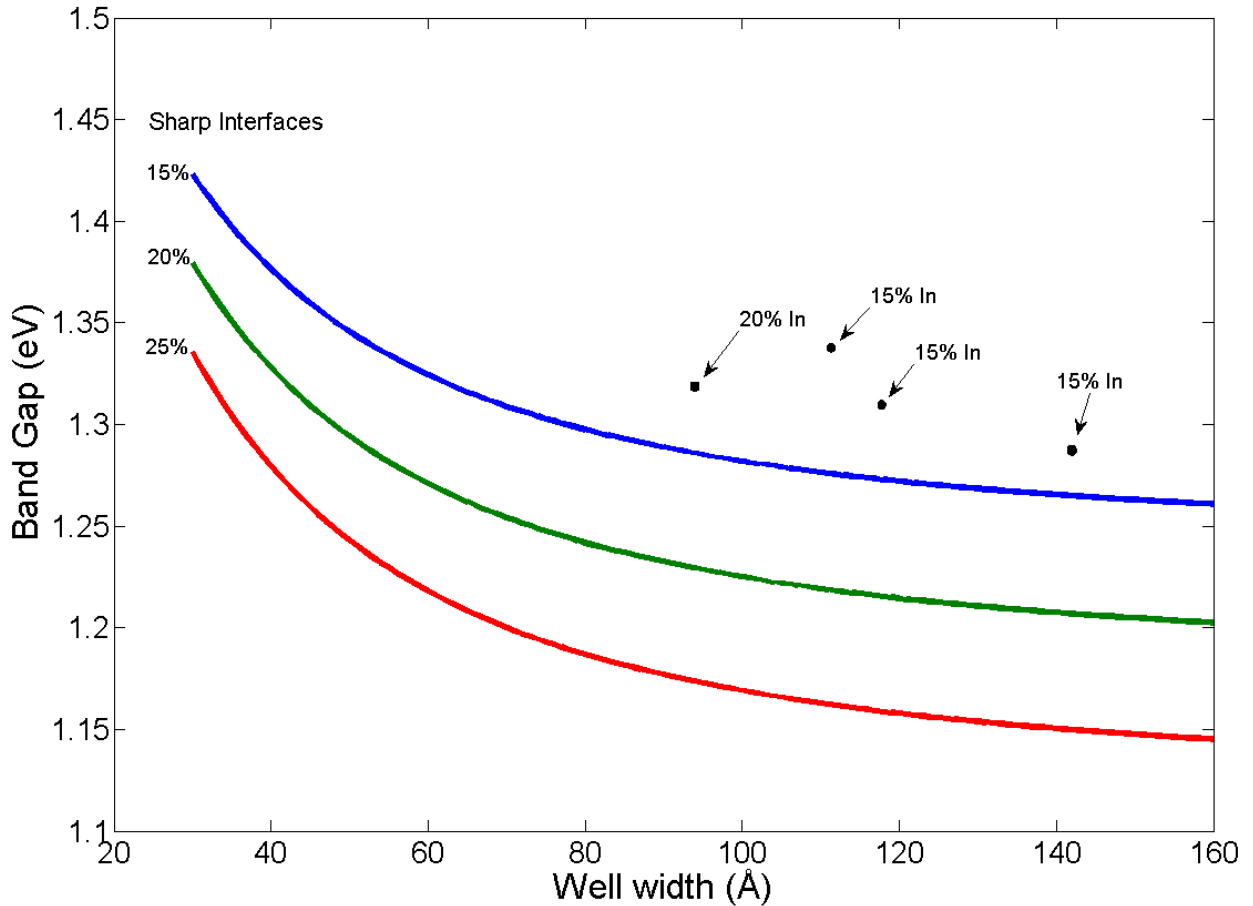


Figure 5.6: Calculated effective band gap for $\text{In}_x\text{Ga}_{1-x}\text{As}/\text{GaAs}_{0.15}\text{P}_{0.85}$ superlattices showing larger effective band gaps as found from EQE measurements of p-i-n SLS devices.

The points on figure 5.6 represent the measured effective band gap from actual superlattice solar cell devices. The effective band gap is found from EQE and PL measurements of the device while the well and barrier widths were found from x-ray diffraction. It can be seen that the band gap is higher in each case in comparison to the calculated band gap. This could be due to a lower indium composition in the wells in comparison to what is found in calibrations for bulk layers. Another possibility is that interface between the GaAsP and InGaAs is not completely abrupt. Figure 5.7 shows these two possible causes of the increased effective band gap.

The Kronig-Penney model as given in eqn. 5.13 is valid for a superlattice composed of two materials with a uniform composition in each layer. This can be modified to account for the band gap shift due to the compressive strain in the InGaAs layers as discussed in section 5.1.2. However, this does not

account for the discrepancy between the calculated and measured effective band gap. This means that the some of the assumptions that were made when calculating the energy levels in the superlattice are not accurate. One possibility is that the composition of the strained layers in the superlattice are not the same as those measured from x-ray analysis of thicker relaxed layers in calibration runs. Another possibility, which will be investigated in this section, is that the interfaces between the InGaAs and GaAsP layers are not completely abrupt.

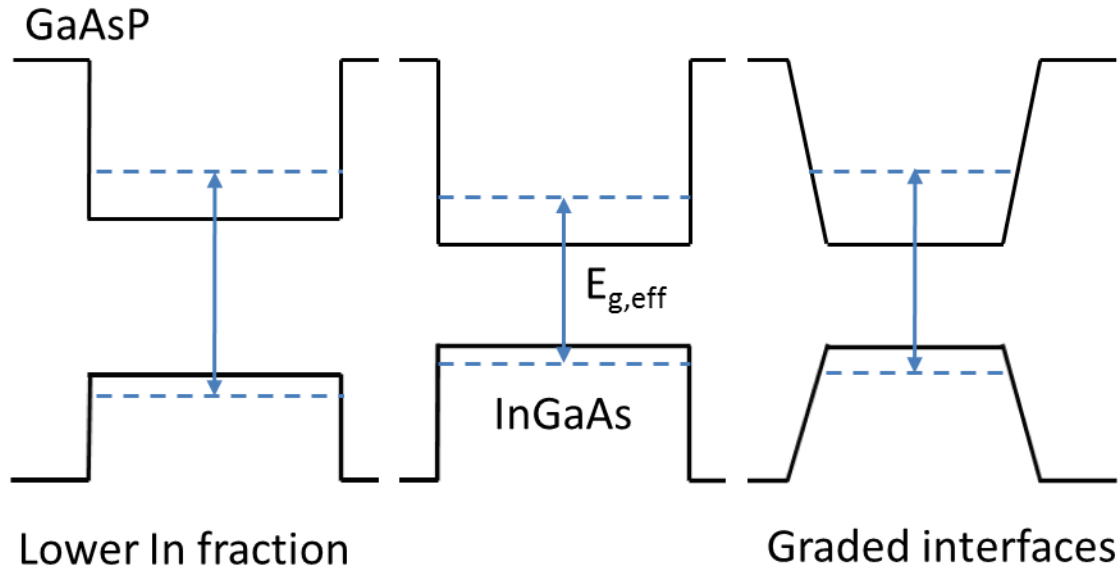


Figure 5.7: Potential sources of effective band gap increase in superlattice structures. There are two modifications of the center well that could give a larger effective band gap: a lower indium fraction (left) and grading the in the P or In composition at interfaces (right).

In order to calculate the effective band gap with a non-abrupt interface requires a more general solution to eqn. 5.1. To do this the transfer matrix method of Yuh and Wang is used [10], which will be summarized below and applied to a superlattice with graded interfaces. The wavefunction vector, Γ , at a point z' in the superlattice structure will be related to Γ at an initial point z through the transfer matrix, S :

$$\Gamma(z') = S\Gamma(z) \quad 5.17$$

Since the boundary conditions apply to both the wavefunction and its derivative, Γ is a 2×1 vector with $\Gamma_1(z) = \psi(z)$ and $\Gamma_2(z) = \psi'(z)/m^*$. Γ_2 is written in this form in order to satisfy the boundary condition in eqn. 5.8.

Since the wavefunction vector has a length of two, S will be a 2×2 matrix. Since the superlattice is periodic it is only necessary to find the transfer matrix over a single period. For a superlattice with n layers this is done by multiplying the transfer matrix for each individual layer to find $S = S_n S_{n-1} \dots S_2 S_1$. The periodic boundary condition of eqn. 5.10 will apply over any number of periods, m :

$$\Gamma(z + mL) = S^m \Gamma(z) \quad 5.18$$

Since S^m must be bounded for $m \rightarrow \infty$, the eigenvalues of S must satisfy $|\lambda| = 1$ [9]. They can be written in the same form as in eqn. 5.10 with $\lambda = e^{\pm iqL}$. The solution to the eigenvalue equation $\det(S - \lambda I) = 0$ gives the dispersion relationship for the superlattice:

$$\frac{1}{2}(e^{iqL} + e^{-iqL}) = \cos(qL) = \frac{1}{2}(S_{11} + S_{12}) \quad 5.19$$

This has the same form as eqn. 5.13. As before, the superlattice energy of the superlattice minibands can be determined by finding where the term $\cos(qL)$ is real.

For regions of constant potential the transfer matrix has the form:

$$S = \begin{bmatrix} \cos(kz) & \frac{m^*}{k} \sin(kz) \\ -\frac{k}{m^*} \sin(kz) & \cos(kz) \end{bmatrix} \quad 5.20$$

Where k is the wavevector as defined in section 5.1.1. When the energy is below the envelope function potential, which will typically be the case in the barrier region, the substitution $k = i\kappa$ can be made to give:

$$S = \begin{bmatrix} \cosh(\kappa z) & \frac{im^*}{\kappa} \sin(\kappa z) \\ -\frac{i\kappa}{m^*} \sin(\kappa z) & \cosh(\kappa z) \end{bmatrix} \quad 5.21$$

For states confined in the well for a simple superlattice with abrupt barriers, as seen in figure 5.8a, the superlattice dispersion can be obtained by multiplying together eqn. 5.20 for the well by eqn. 5.21 for the barrier.

$$S = S_w S_b = \begin{bmatrix} \cos(k_w L_w) & \frac{m^*}{k_w} \sin(k_w L_w) \\ -\frac{k_w}{m^*} \sin(k_w L_w) & \cos(k_w L_w) \end{bmatrix} \begin{bmatrix} \cosh(\kappa_b L_b) & \frac{im^*}{\kappa_b} \sin(\kappa_b L_b) \\ -\frac{i\kappa_b}{m^*} \sin(\kappa_b L_b) & \cosh(\kappa_b L_b) \end{bmatrix} \quad 5.22$$

Substituting S_{11} and S_{22} into eqn. 5.19 will give the typical expression for the Kronig-Penney model. This expression will apply to both the electron and light and heavy hole states.

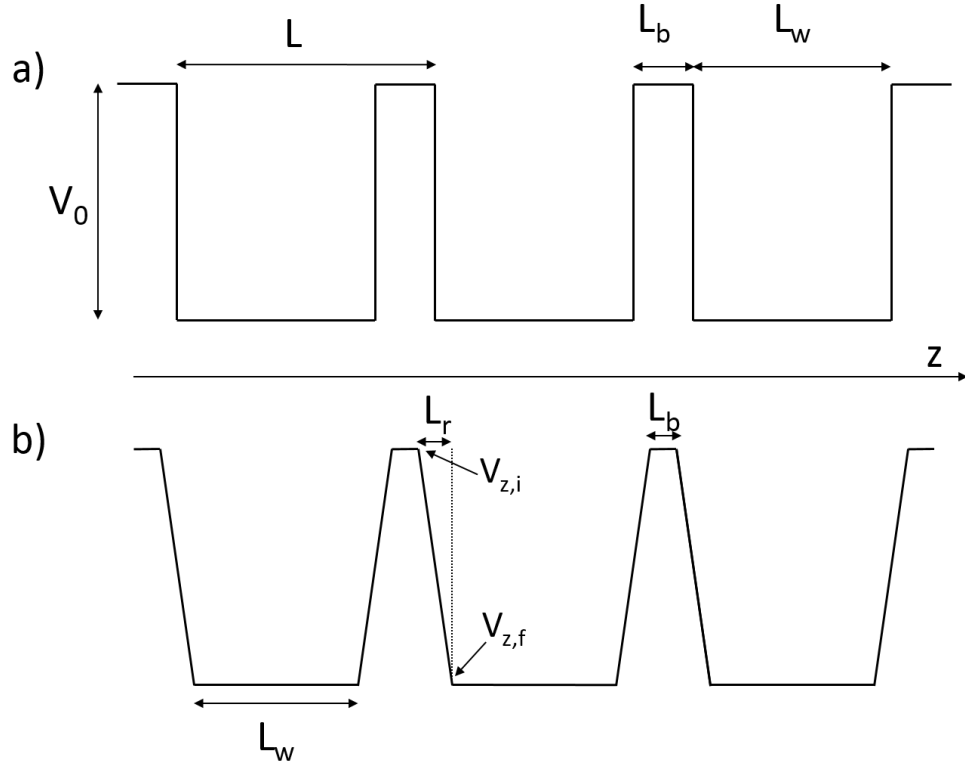


Figure 5.8: Schematic of the conduction band envelope function for superlattices with a) abrupt and b) graded interfaces.

Figure 5.8b shows the envelope function for a superlattice that has compositionally graded interfaces. For simplicity, the envelope function is assumed to vary linearly, but it should be possible to use any band profile as long as the transfer matrix can be properly constructed. One method is to approximate the graded region as a series of steps of constant energy. As the width of each step is reduced, the approximation will approach the actual doping profile, but this may require a large number of steps. Since the graded region is taken to be a linear function, it is also possible to use an exact solution. Consider a linearly graded region of length L_r with an initial potential of $V_{z,i}$ and a final potential of $V_{z,f}$. If the Schrödinger equation for the graded region:

$$-\frac{\hbar^2}{2m^*(z)} \frac{d^2\psi}{dz^2} + \left[V_{z,i} + z \frac{(V_{z,f} - V_{z,i})}{L_r} \right] \psi = E_z \psi \quad 5.23$$

Can be written in the form

$$\psi''(\zeta) - \zeta\psi(\zeta) = 0 \quad 5.24$$

then the solutions will be a linear combination of the two Airy functions, $\text{Ai}(z)$ and $\text{Bi}(z)$ [11]. The Airy function solution has been used to analyze quantum wells and superlattices in an electric field, but it is necessary to derive the results for a compositionally graded region.

If eqn. 5.23 can be rearranged as $\psi''(z) - az\psi(z) = 0$, then it can be transformed into eqn. 5.24 through the change in variable $\zeta = a^{1/3}z$ [11]. Rearranging eqn. 5.23 will give:

$$\frac{d^2\psi}{dz^2} - \frac{2m^*(z)}{\hbar^2} \left[(V_{z,i} - E_z) + z \frac{V_{z,f} - V_{z,i}}{L_r} \right] \psi = 0 \quad 5.25$$

The effective mass is still given as a function of position since it depends upon the semiconductor composition. One assumption that will be made is that the spatially dependent effective mass can be replaced by the average effective mass, m_{av}^* . This means that ζ is:

$$\zeta = \left[\frac{2m_{av}^*(V_{z,f} - V_{z,i})/L_r}{\hbar^2} \right]^{1/3} \left(z + \frac{V_{z,i} - E_z}{(V_{z,f} - V_{z,i})/L_r} \right) \quad 5.26$$

The same boundary conditions apply to the graded potential layers as they do to the constant potential layers. The transfer matrix for graded layer between the points ζ_i and ζ_f is:

$$K = \left[\frac{2((V_{z,f} - V_{z,i})/L_r)}{(m_{av}^*\hbar)^2} \right]^{1/3} \quad 5.27$$

$$S_{11} = \pi [Bi'(\zeta_i)Ai(\zeta_f) - Ai'(\zeta_i)Bi(\zeta_f)]$$

$$S_{12} = \pi K^{-1} [Bi(\zeta_i)Ai(\zeta_f) - Ai(\zeta_i)Bi(\zeta_f)]$$

$$S_{21} = -\pi K [Bi'(\zeta_i)Ai'(\zeta_f) - Ai'(\zeta_i)Bi'(\zeta_f)]$$

$$S_{22} = -\pi [Bi(\zeta_i)Ai'(\zeta_f) - Ai(\zeta_i)Bi'(\zeta_f)]$$

Using these expressions the dispersion expression for the graded interface superlattice can be found.

There are a few assumptions that were made when investigating the effect of graded barrier layers since the shape of the envelope function is not known. The graded portion is assumed to vary linearly from GaAs (0% phosphorus) to the maximum phosphorus composition and the same grading is present on both sides of the GaAsP barrier. Also, the total amount of phosphorus is the same in the graded and the abrupt barriers. Since the average composition in the graded portion is half that of the maximum phosphorus composition this means that the barrier layer thicknesses are set to satisfy $L_b = L_f + 2L_r$ where L_b is the thickness of the abrupt interface barrier, L_r is the thickness of the graded portions and L_f is the constant potential portion of the graded interface barrier.

Since the magnitude of the grading is unknown, $E_{g,eff}$ was found for several values of L_r . Figure 5.9 shows the same results as figure 5.6 for the observed absorption energy in quantum well solar cells, but now includes modeling for a graded barrier. The graded barrier has a larger effect on thinner wells

since the grading reduces the thickness of a larger fraction of the well when it is already thin. The thickness for the graded layer that fits the experimental data the closest is for an L_r of 20 Å. L_f for the same barrier would be 10 Å, which indicates that there could large compositional variation in the GaAsP barriers. Section 5.2.2 will discuss experimental results that show that this is the case.

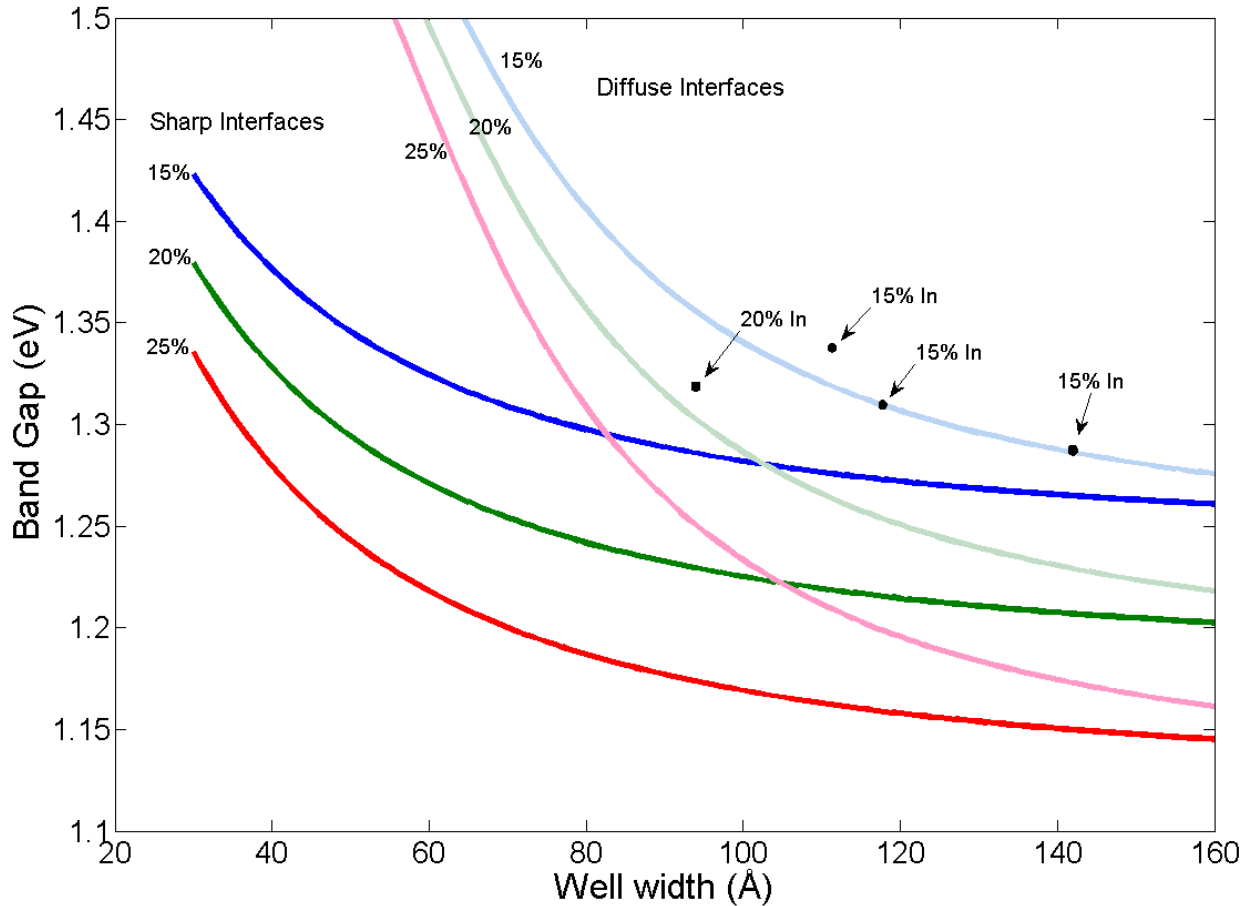


Figure 5.9: Effective band gap for $\text{In}_x\text{Ga}_{1-x}\text{As}/\text{GaAs}_{0.15}\text{P}_{0.85}$ superlattices with and without grading at the InGaAs/GaAsP heterointerface.

5.1.4. Effect of built-in electric field on energy states in quantum wells

There are two structures in which the InGaAs/GaAsP superlattice was grown. The first was used to determine the growth parameters in order to balance the superlattice. It is composed of an undoped GaAs nucleation layer, followed by the superlattice structure and ends with an undoped GaAs capping layer. In some instances a thin AlGaAs window was grown after the superlattice in order to trap photogenerated carriers to improve the photoluminescence intensity. The other structure is a p-i-n diode with the superlattice in the intrinsic region. Since the superlattice is in the depletion region of the diode, it will be within the built-in electric field of the diode. Typical devices had an i-layer

thickness that varied from 0.5 to 1.0 microns and p- and n-type doping levels in GaAs of 2×10^{18} and $2 \times 10^{17} \text{ cm}^{-3}$, respectively. This would result in an electric field in the i-layer of 14-28 kV/cm. The flat band assumption used in the Kronig-Penney analysis is no longer valid in this case. As a result of this field there will be a shift in the energy levels in the quantum wells, a phenomenon known as the Stark effect.

To estimate the magnitude of the Stark effect, the Stark shift, the variational calculation of Bastard can be used [12]. At low electric fields the variational calculation only depends upon the quadratic term, as long as the following inequality is satisfied:

$$qFL_q < \frac{\hbar^2 \kappa_b^3 L_w}{2m_b^*} \quad 5.28$$

The same quantum well material parameters will be used as in section 5.1.1, a 100 \AA $\text{In}_{0.15}\text{Ga}_{0.85}\text{As}$ well cladded with $\text{GaAs}_{0.25}\text{P}_{0.75}$. Assuming an extreme value for the electric field of 30 kV/cm, the total change in the potential due to the electric field is 30 meV. The right hand side gives 6.6 eV, so the quantum wells are easily in the low field regime.

The Stark shift can then be approximated as:

$$\Delta E = -\frac{\Omega^2 m_w^* F^2 L^4}{8\hbar^2} \quad 5.29$$

where Ω is a function of the wavevectors in the barrier and well and the well thickness. For the well described above, this results in a reduction in the band gap of 4 meV. This represents the largest electric field that is expected at zero bias for any of the p-i-n superlattice devices. Consequently, the Stark effect shift will not be included in any subsequent calculations of the effective band gap in the InGaAs wells.

5.1.5. Constraints for quantum well structures: strain-balancing and carrier transport

For an InGaAs/GaAsP superlattice there are several factors that constrain the thickness and composition of the well and barrier layers. They are 1. The critical layer thickness 2. the strain balance condition and 3. the carrier transport condition.

5.1.5.1. Critical layer thickness

In section 5.1.2 it was mentioned that when an epitaxial layer with cubic symmetry is grown on a substrate with a different lattice constant, it will undergo a tetragonal distortion of the lattice. This distorted lattice is at a higher potential energy relative to the usual cubic structure and the energy stored is larger for thicker layers. Eventually the energy due to the strain will reach a critical value,

causing the material to relax to its equilibrium lattice constant. This relaxation results in the formation of dislocations in the strained layer and any subsequent epitaxial layers. The thickness at which the material reaches the critical energy is known as the *critical layer thickness* (CLT) and its value will depend upon the lattice mismatch between the substrate and the epitaxial layer and the elastic parameters of the strained material.

There are several models for finding the critical layer thickness including those of People and Bean [13] and Matthews and Blakeslee [14]. The latter model has the best agreement with experimental results for III-V semiconductors. For a strained material the CLT, h_c , is given by the transcendental equation:

$$h_c = \frac{b(1-\nu/4)}{2\pi f(1+\nu)} \ln\left(\frac{h_c}{b} + 1\right) \quad 5.30$$

where ν is Poisson's ratio for the strained material, b is the magnitude of Burger's vector and f is the mismatch between the strained layer and substrate. Figure 5.10 shows the CLT calculated for InGaAs and GaAsP over the range of compositions at which they were grown.

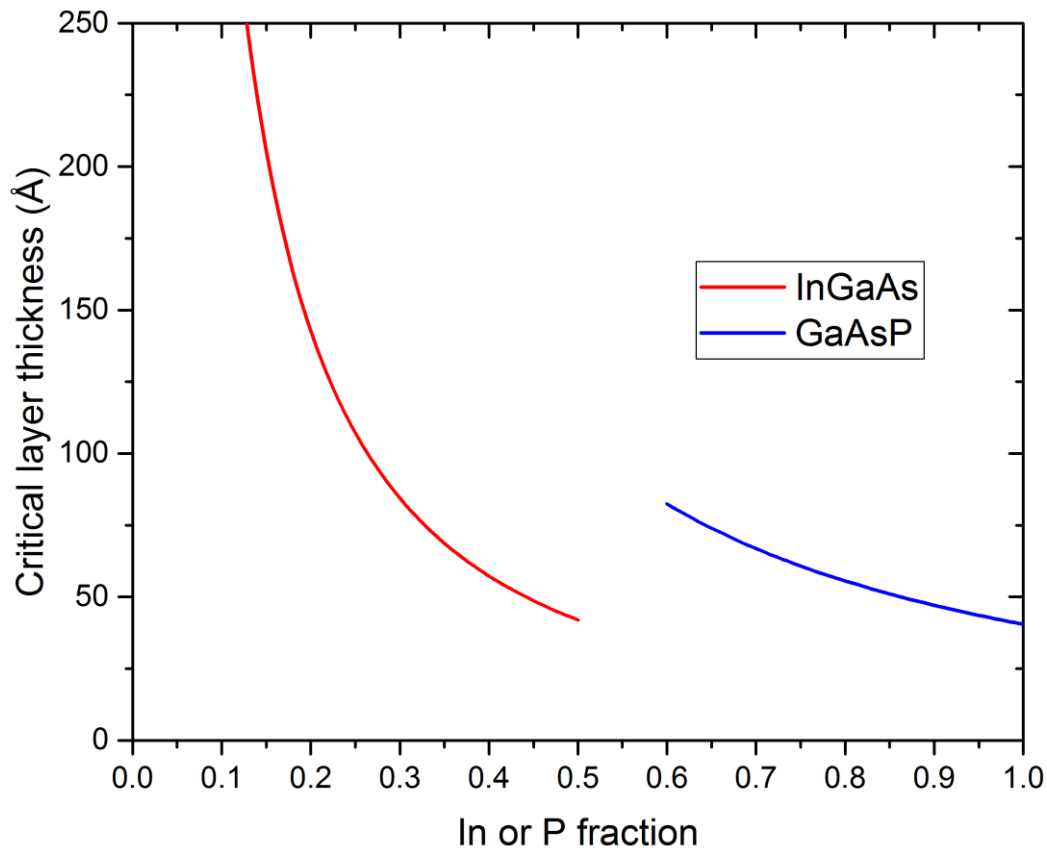


Figure 5.10: Critical layer thickness for InGaAs and GaAsP on GaAs calculated using the model of Matthews and Blakeslee.

5.1.5.2. Strain balance

Even if the individual layers are below the CLT it is still possible for the superlattice to relax if the strain balance condition is not met. If the strain from the tensile and compressive layers is not balanced, then there will be a net accumulation of one type of strain in the structure. As when the CLT is exceeded, an excess of net strain will result in the relaxation of the strained layers and the formation of defects. This is particularly important when there are a large number of periods. The growth of non-uniform layers has been observed for when the strain mismatch is high and a large number of periods are grown.

There are four parameters that can be controlled during the InGaAs/GaAsP superlattice growth: the indium fraction and thickness of the InGaAs layers and the phosphorus fraction and thickness of the GaAsP layers. For any three of these parameters chosen, the fourth will be constrained by the strain balance condition. For a given composition for the InGaAs and GaAsP layers, the thickness of the GaAsP was set to the maximum thickness that did not hinder carrier transport through the superlattice. Hence, the balancing was done by changing the thickness of the InGaAs layer. Mismatched superlattices exhibited crosshatching on the surface, which was visible at 100× magnification as viewed through a stereomicroscope. Furthermore, the type of crosshatching indicated the direction of the mismatch: superlattices with excessive compressive strain (InGaAs layer too thick) showed crosshatching in two orthogonal directions while superlattices with excessive tensile strain (InGaAs layer too thin) was crosshatched primarily in a single direction.

The simplest method for balancing the superlattice is to find the thicknesses of the two layers that result in an average lattice constant that is the same of the substrate layers. However, this does not account for the difference in the elastic parameters between GaAsP and InGaAs. A superlattice that balanced through the average lattice constant method is expected to have a zero order (n_0) peak in the x-ray diffraction at the same position as the GaAs substrate. Instead these structures exhibit tensile crosshatching which disappears only when the InGaAs layer thickness is increased. A more accurate balancing method is to find the thickness of each layer where the net stress from the tensile and compressive layers is zero [15].

5.1.5.3. Carrier transport

The necessity of tunneling through the GaAsP barrier layers will place limits on their thickness. Due to the high phosphorus composition of the barriers ($\text{GaAs}_{1-x}\text{P}_x$ with $0.65 < x < 0.85$), the conduction band offsets are in excess of 500 meV and the valence band offsets are above 300 meV [16]. This eliminates the possibility of thermionic emission over the barriers at 300 K, making tunneling the

primary transport mechanism for both electrons and holes. Since the tunneling probability has an exponential dependence on the barrier thickness, resulting a reduction in solar cell device performance for devices with superlattices with barriers thicker than 30 Å. The problem of carrier transport will be expanded upon more thoroughly in chapter 6.

5.1.6. Optimization of composition and thickness of strain-balanced quantum wells and barriers

In order to maximize the absorption from the superlattice, it is useful to determine the ideal composition and thickness of the InGaAs and GaAsP while still fulfilling the strain balance and carrier transport conditions. The optimization of the superlattice structure must also take into account any non-abrupt interfaces between the two ternary materials. This will help in the design of a superlattice structure that minimizes the impact of non-abrupt interfaces.

Figure 5.11 is a modified version of figure 6 to include the CLT, transport and strain balance constraints. The range of $\text{In}_x\text{Ga}_{1-x}\text{As}$ compositions has also been extended to a minimum of $x=0.10$ and a maximum of $x=0.3$. The solid purple line shows the critical layer thickness limit for the InGaAs layers, while the solid orange line is the limit for an InGaAs layer strain balanced to a critically strained $\text{GaAs}_{0.15}\text{P}_{0.85}$ layer. Since the CLT decreases as the lattice mismatch increases, wells with high InGaAs compositions must be made thinner. The critical layer thickness limits are close for the two materials. GaAsP is the limiting layer for low indium fractions and InGaAs is the limiting layer for high indium fractions, with a crossover near 20% In.

A more severe restraint is created by the requirement that the GaAsP barrier be limited to 30 Å in order to ensure for complete tunneling through the SLS structure. The dotted orange lines in figure 11 show the maximum thickness for an InGaAs layer that is lattice matched to a 30 Å $\text{GaAs}_{1-y}\text{P}_y$ with y equal to 0.65, 0.70, 0.75, 0.80 and 0.85. Higher phosphorus compositions allow for thicker InGaAs layers, but even for $y=0.85$ the tunneling constraint requires InGaAs layers that are well below the CLT for both InGaAs and GaAsP. For every barrier composition the lowest effective band gap occurs for $\text{In}_{0.3}\text{Ga}_{0.7}\text{As}$ wells. With abrupt 30 Å $\text{GaAs}_{0.15}\text{P}_{0.82}$ barriers an SLS p-i-n device could be expected to have an absorption extension to 1052 nm for $\text{In}_{0.3}\text{Ga}_{0.7}\text{As}$ wells and an extension to 996 nm for $\text{In}_{0.2}\text{Ga}_{0.8}\text{As}$ wells.

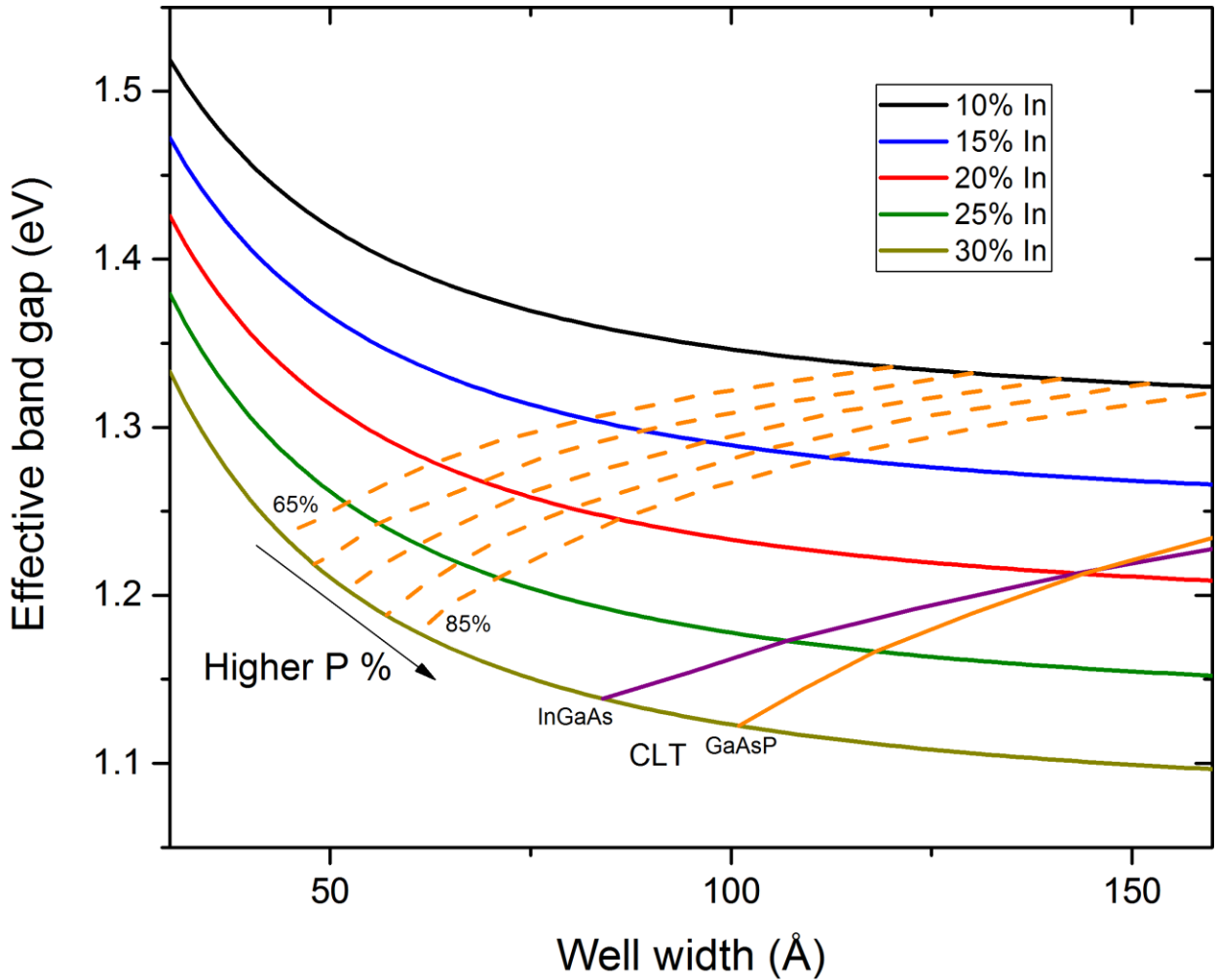


Figure 5.11: Effective band gap for an abrupt interface InGaAs/GaAsP SLS. The purple line is the CLT constraint for InGaAs and the solid orange line is the CLT constraint for GaAsP. The dotted orange lines are the 30 Å barrier thickness tunneling constraint for $\text{GaAs}_{1-y}\text{P}_y$ ranging from $y=0.65$ to $y=0.85$.

Figure 5.12 shows the same results as figure 5.11 except that it includes a 20 Å grading of the GaAsP barrier layer at both interfaces. As with the abrupt interface SLS, the carrier transport constraint is more severe than the critical layer thickness constraint for all compositions of the InGaAs and GaAsP within the given range. The significant difference is in the tunneling transport constraint since the quantum size effects are severe for InGaAs layers less than 100 Å with graded barriers. Since higher indium compositions require thinner layers to maintain strain balance, the minimum effective band gap is for $\text{In}_x\text{Ga}_{1-x}\text{As}$ with $x < 0.3$, unlike the abrupt interface SLS. For a $\text{GaAs}_{0.35}\text{P}_{0.65}$, the minimum effective band gap is 1.363 eV (or 910 nm) for an $\text{In}_{0.1}\text{Ga}_{0.9}\text{As}$ well. The higher phosphorus $\text{GaAs}_{0.15}\text{P}_{0.85}$ barrier has a somewhat lower minimum effective band gap of 1.317 eV (941 nm) for an $\text{In}_{0.2}\text{Ga}_{0.8}\text{As}$.

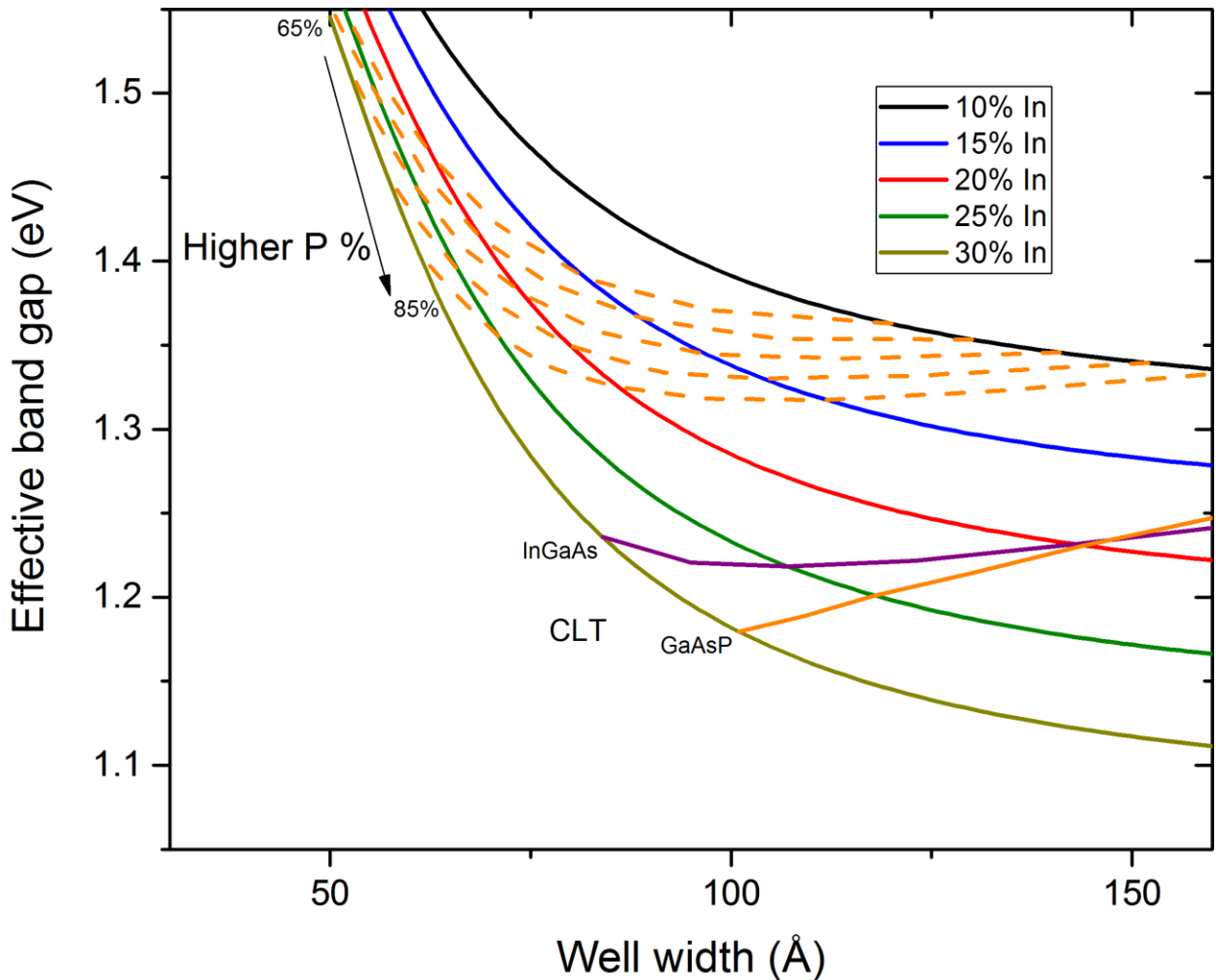


Figure 5.12: Effective band gap for a 20 Å graded interface InGaAs/GaAsP SLS. The purple line is the CLT constraint for InGaAs and the solid orange line is the CLT constraint for GaAsP. The dotted orange lines are the 30 Å barrier thickness tunneling constraint for $\text{GaAs}_{1-y}\text{P}_y$ ranging from $y=0.65$ to $y=0.85$.

The presence of interfacial grading places several limits on the type of SLS structures that can be effectively grown. Barriers with low phosphorus compositions are impractical since the 910 nm extension for a $\text{GaAs}_{0.35}\text{P}_{0.65}$ is barely beyond the absorption edge of GaAs. Grading also precludes the use of high indium compositions since the minimum effective band gap occurs at lower compositions. The next section will discuss experimental investigations of interface grading and address attempts made to minimize its influence on the absorption band edge of SLS devices.

5.2. Extension of absorption in quantum well solar cell devices

There are two purposes for modeling of the effective band gap in InGaAs/GaAsP superlattices. The first is to explain the results from MOCVD grown superlattices and superlattice devices. The second

is to use these results to design quantum well structure that maximizes the gains in efficiency and short circuit current.

5.2.1. The p-GaAs/i-MQW/n-GaAs solar cell structure

Before the addressing the problem of SLS absorption extension, the structure of the SLS p-i-n solar cell devices must be discussed. Figure 5.13 shows the structure of a typical device. This structure was used both for the results in this in this chapter and those in chapter 6. Devices have been grown with a p-type base and an n-type emitter and with an n-type base and a p-type emitter. Devices without the SLS intrinsic layer were also grown, in which case the doping in the dopant precursor was abruptly switched from the base dopant to the emitter dopant without the growth of a GaAs i-layer.

Typical doping levels were $2 \times 10^{17} \text{ cm}^{-3}$ in the emitter and $2 \times 10^{18} \text{ cm}^{-3}$ in the base, irrespective of the particular dopants. Silicon was used as an n-type dopant while both zinc and carbon were used as p-type dopants. The window layer was composed of $\text{Al}_x\text{Ga}_{1-x}\text{As}$ with x ranging from 0.75 to 0.9. It was doped with the same type as the emitter layer. Window thicknesses ranged from 200 to 300 Å. Thinner windows absorbed less light at low wavelengths but were more susceptible to being removed during device processing .The back surface field was grown either with as a low aluminum composition $\text{Al}_x\text{Ga}_{1-x}\text{As}$ (x=0.2-0.3) or as a GaAs layer doped to $2 \times 10^{18} \text{ cm}^{-3}$

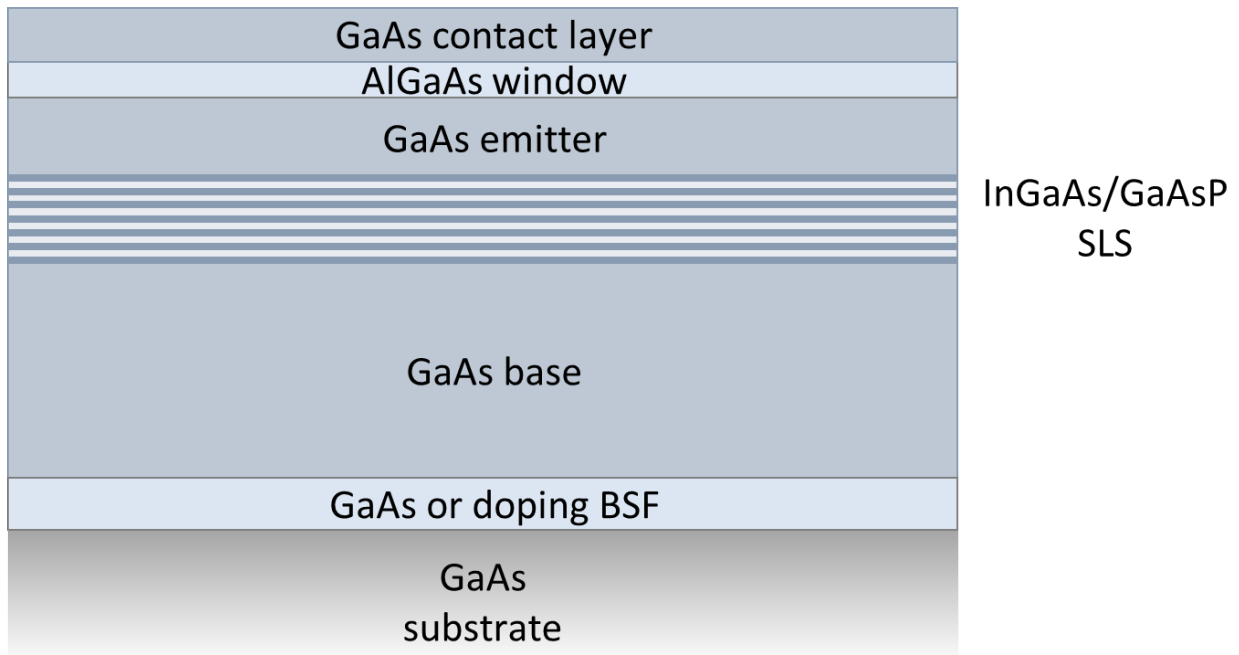


Figure 5.13: Typical structure for a SLS p-i-n solar cell

The superlattices were grown as alternating layers of InGaAs and GaAsP. Both the TMGa and TBAs were held to a constant flow throughout the superlattice. Initially the two ternary semiconductors were grown sequentially: the TMIn was switched to the run line at the same time the TBP was switched to the vent line, and vice versa. However, this resulted in a rough surface morphology. It was found that the surface morphology could be improved by including a 2 second (7.5 Å) layer of GaAs at both ternary-ternary interfaces. The SLS was grown without dopant precursors. However, there is an unintentional p-type background doping primarily due to carbon from the TMGa. GaAs layers grown under similar conditions to the superlattice were found to have a background doping of $3 \times 10^{15} \text{cm}^{-3}$ from Hall effect measurements. This limits the thickness of SLS to less than 1 µm in order to ensure that is within the depletion region. Refer to chapter 4 for more details on the MOCVD growth process.

5.2.2. The effect of quantum well composition and thickness on absorption extension

The current produced by a solar cell is a function of the quantum efficiency of the cell and the spectral distribution of the light incident upon the cell. This means that the quantum efficiency of a particular cell is a good metric for determining the short circuit current. If a cell has a higher quantum efficiency at all wavelengths relative to another cell, then it is expected that the short circuit current will be higher in this cell, regardless of the particular solar irradiance spectrum.

In a typical solar cell device that is composed of a single absorbing semiconductor material, the quantum efficiency drops to zero at energies below the band gap. The addition of a quantum wells composed of a lower band gap material to such a cell makes it possible to extend the quantum efficiency to energies below the band gap of the bulk semiconductor material, which 1.424 eV or 871 nm for GaAs. This extension of the quantum efficiency can be improved in two ways: 1) by decreasing in the energy cutoff of the solar cell absorption by using a quantum well with an effective band gap below that of the GaAs and 2) by improving the absorption in the quantum well region so that the quantum efficiency extension is increased. The focus of this chapter is to maximize the improvement from the first scenario.

Figures 5.14 and 5.15 show two sets of quantum well devices that have reduced extension due to quantum confinement. The superlattices in figure 5.14 both have 25 Å GaAs_{0.25}P_{0.75} barriers. The well thickness for the superlattice containing In_{0.23}Ga_{0.77}As wells is 56 Å while that for the superlattice with In_{0.17}Ga_{0.83}As wells is 77 Å. The extension is below 900 nm for both structures. This shows the importance of maximizing the barrier thickness. Thinner barrier layers will require thinner well layers in order to maintain the strain balance condition. It also demonstrates that this problem cannot be

addressed by increasing the indium fraction in the well. Since the $\text{In}_{0.23}\text{Ga}_{0.77}\text{As}$ must be made thinner, it is subject to a more severe quantum confinement, which results in a higher effective band gap compared to the $\text{In}_{0.17}\text{Ga}_{0.83}\text{As}$ well.

Figure 5.15 shows another set of quantum well devices. The thicker barriers (30 \AA) and higher phosphorus compositions ($\text{GaAs}_{0.22}\text{P}_{0.78}$) result in a much larger extension in the EQE. However, like the devices in figure 5.14, the higher indium composition in the well does not result in a decrease in the effective band gap. The 935 nm extension for the $\text{In}_{0.15}\text{Ga}_{0.85}\text{As}$ well device corresponds to an effective band gap of 1.326 eV, which is close to the 1.328 eV that is given from the curve in figure 5.12. The 916 nm (1.353 eV) extension for the $\text{In}_{0.15}\text{Ga}_{0.85}\text{As}$ well is somewhat less than expected, since the graded potential model gives an effective band gap of 1.331 eV.

These results indicate that it is likely that the interface between the InGaAs and GaAsP is not abrupt. As a result, the extension in the EQE is being reduced by the severe quantum confinement in the wells. This reduces the increase in short circuit current from quantum well devices. It also limits the composition of the superlattice layers to $x < 0.2$ for $\text{In}_x\text{Ga}_{1-x}\text{As}$ and $y > 0.75$ for $\text{GaAs}_{1-y}\text{P}_y$.

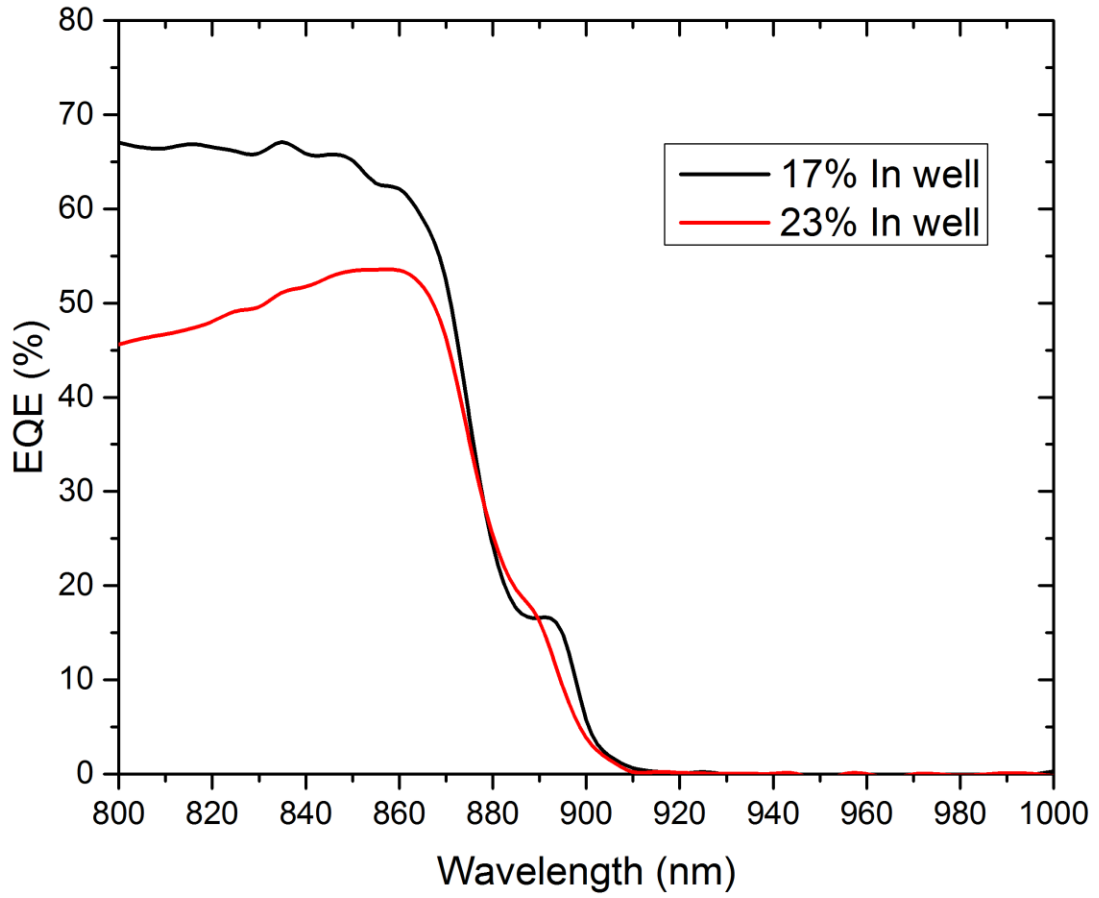


Figure 5.14: EQE showing the extension of absorption due to $\text{In}_{0.17}\text{Ga}_{0.83}\text{As}$ and $\text{In}_{0.23}\text{Ga}_{0.77}\text{As}$ wells with 25\AA $\text{GaAs}_{0.25}\text{P}_{0.75}$ barriers.

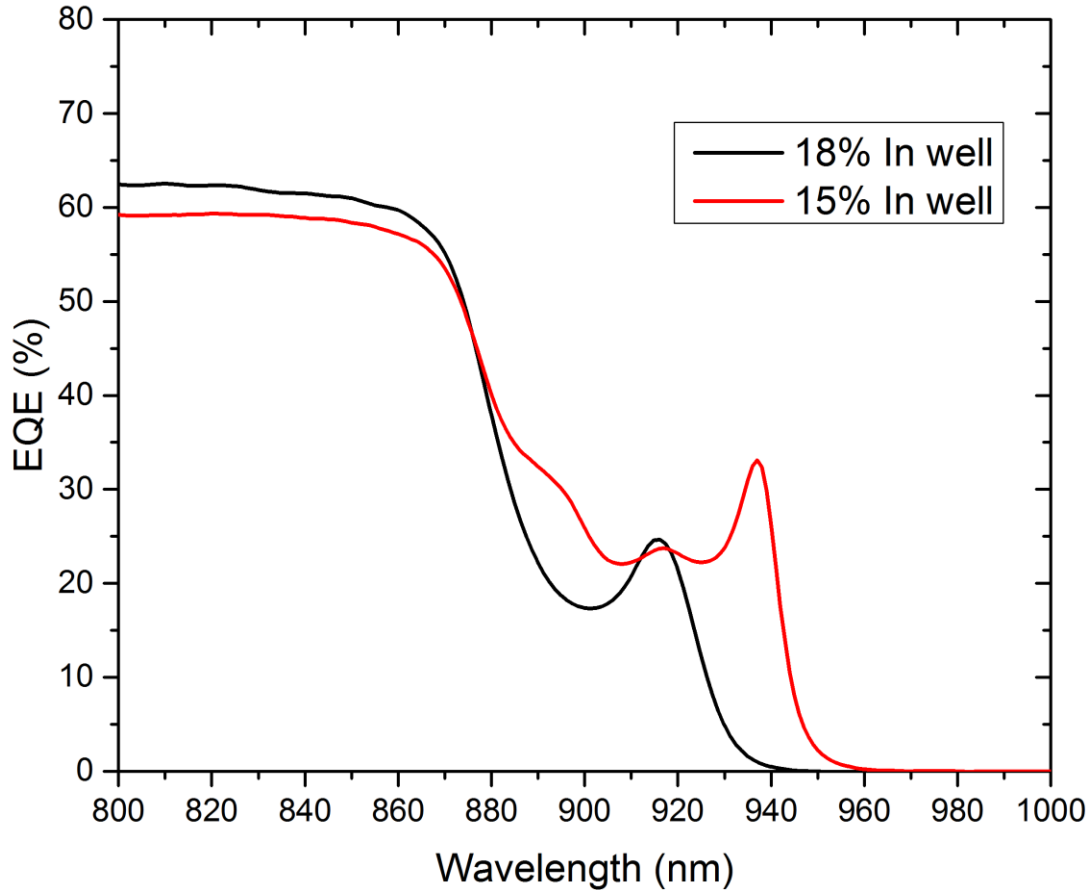


Figure 5.15: EQE showing the extension of absorption due to $\text{In}_{0.18}\text{Ga}_{0.83}\text{As}$ and $\text{In}_{0.15}\text{Ga}_{0.77}\text{As}$ wells with 30\AA $\text{GaAs}_{0.22}\text{P}_{0.78}$ barriers.

5.2.3. The addition of GaAs layers at InGaAs/GaAsP interfaces and the effect on interface grading

In order to address the graded barrier issue it is necessary to determine which interface is responsible for the observed behavior. In an InGaAs/GaAsP superlattice, there are two types of interfaces: the transition from InGaAs to GaAsP (referred to as the In→P interface) and the transition from GaAsP to InGaAs (referred to as the P→In interface). While it was assumed in section 5.1.3. that the two interfaces are equivalent, the actual behavior of the interfaces will depend upon the properties of the individual elements and their organometallic precursors.

There are several potential mechanisms that could cause the interfacial grading. Arsenic-phosphorus exchange or phosphorus carryover can result in grading at the P→In interface while indium segregation can cause grading at the In→P interface. To determine the dominant mechanism, it is necessary to first determine which interface is responsible for the observed increase in the effective band gap. This can be done by increasing the length of the GaAs layer at each interface and seeing the effect that this has on the photoluminescence of the superlattice.

Three superlattices were grown with 94 Å $\text{In}_{0.23}\text{Ga}_{0.87}\text{As}$ and 30 Å $\text{GaAs}_{0.2}\text{P}_{0.8}$ for 20 periods. They differed in the thickness of the GaAs at each interface. One had 7 Å at both interfaces, the second had 7 Å at the interface and 70 Å at the P→In interface and the third had 70 Å at the In→P interface and 7 Å at the P→In interface. The photoluminescence response was measured between 850 and 1100 nm, as shown in figure 5.16. There was little change when the GaAs thickness was increased at the In→P interface, but there is a significant increase in the wavelength of the peak PL intensity when the GaAs was thickened at the P→In interface. This demonstrates that the large quantum size effects are due to carryover of phosphorus into the InGaAs layer. When the GaAs thickness at this interface is increased, the thickness of the InGaAs well is effectively thicker at the energy levels corresponding to the n=1 states in the conduction and valence band that are responsible for the absorption edge and primary PL emission. While the well is thicker at energy higher energy levels when the GaAs thickness is increased at the In→P interface, in the absence of any grading in the phosphorus and indium composition, there is no change in the peak PL wavelength as these n=1 states are below the energy level of the GaAs.

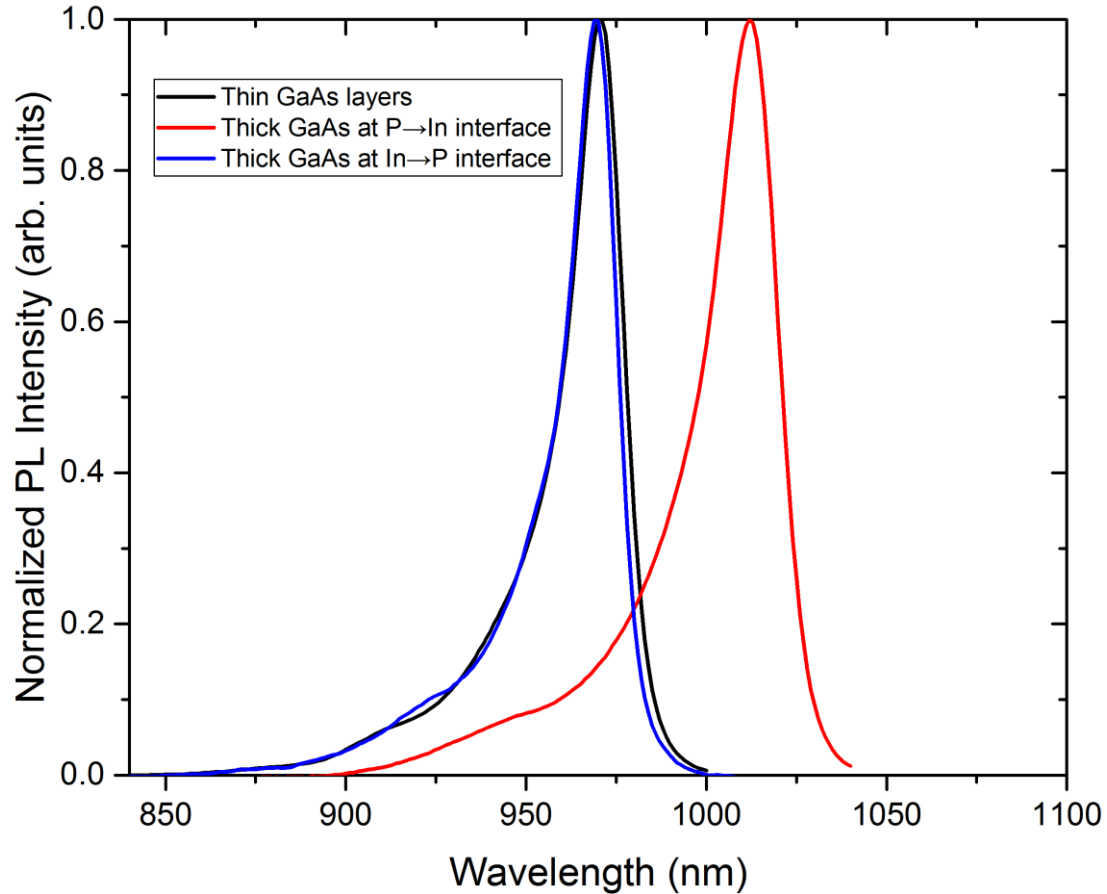


Figure 5.16: PL response of superlattice showing the effect of increasing the GaAs thickness as both ternary/ternary interfaces.

A direct measurement of the phosphorus carryover was found by Joshua Samberg through an energy dispersive spectroscopy scanning tunneling microscopy (EDS-STEM) measurements [17]. EDS-STEM is capable of determining the relative elemental composition of the superlattice as a function of position. The EDS-STEM results were in agreement with the PL results. Both the indium and phosphorus compositions were abrupt at the In→P interface while the P→In interface showed a carryover of the phosphorus. This carryover was present for structures with both a 7 Å and 70 Å GaAs layers at this interface. The phosphorus composition decreased by one half for every 15 Å grown after the TBP was switched from the run to the vent line. This means that for the 70 Å GaAs layers, the phosphorus composition has dropped to 4% of the barrier composition, which means that the InGaAs layer contains very little phosphorus. This also explains the necessity for a thin GaAs layer at the P→In interface. If the InGaAs growth begins immediately after the GaAsP layer there will be a large fraction of phosphorus remaining, resulting in the growth of InGaAsP. These high phosphorus fractions may be within the immiscible composition range for InGaAsP.

Having determined that the carryover of phosphorus at the P→In interface is responsible for the decrease in the effective band gap in the InGaAs wells, the effect of the GaAs thickness was investigated for superlattice solar cell devices. Since the GaAs layer limits the number of periods that can be included within a particular thickness, it is desirable to minimize the thickness while maximizing the absorption band edge of the superlattice. Three devices were grown with 100 Å In_{0.18}Ga_{0.82}As wells, 31 Å GaAs_{0.35}As_{0.35} barriers and 7 Å of GaAs at the In→P interface. The difference between the three structures was the thickness of the GaAs at the P→In interface, which was set to 25, 50 and 75 Å. Figure 5.17 shows the EQE for each of these devices. An increase in the extension from 945 to 955 was observed when the GaAs thickness was increased from 25 Å to 50 Å, but was unchanged when the GaAs thickness was increased from 50 Å to 75 Å. The ideal thickness for this layer is somewhere between 25 Å and 50 Å. The phosphorus composition of the barriers in these devices was lower than in other structures at 65%. In the absence of the GaAs buffer layer such a device would not have been feasible.

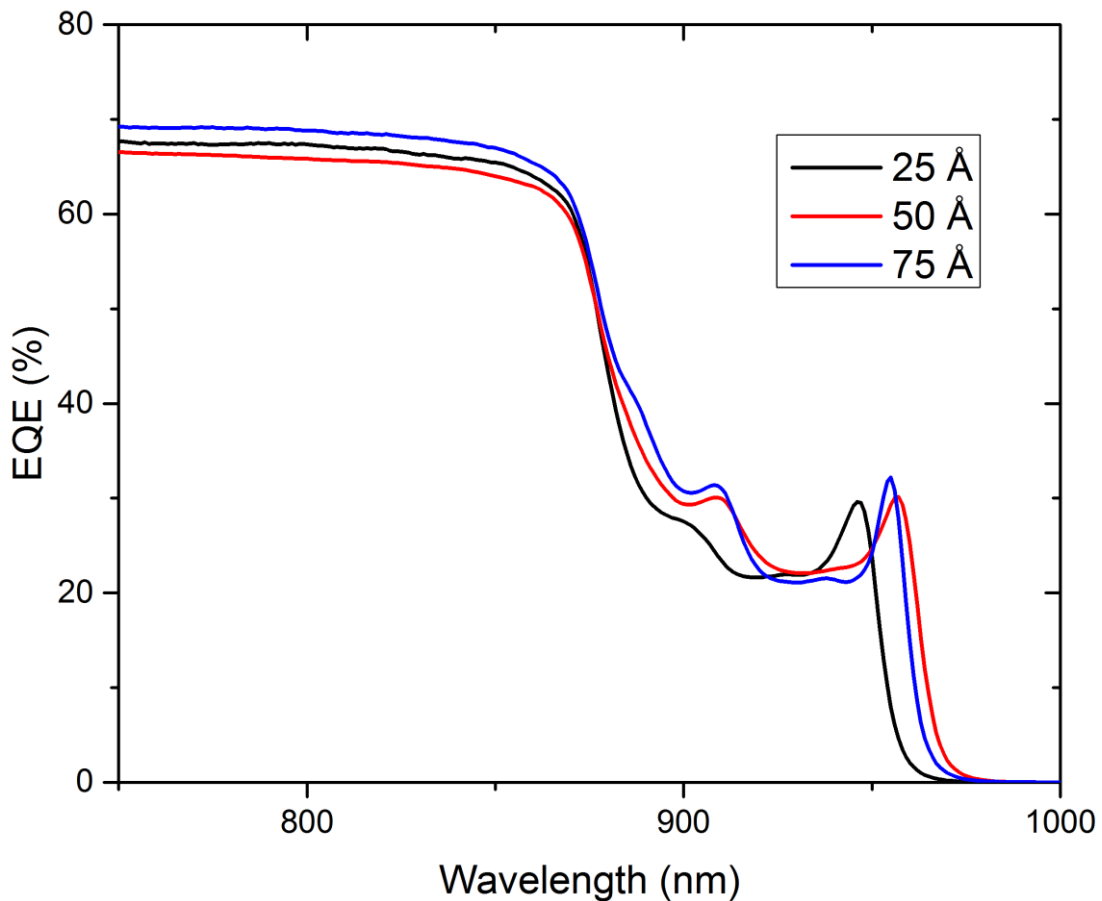


Figure 5.17: EQE of In_{0.18}Ga_{0.82}As/GaAs_{0.35}P_{0.65} superlattice devices with 25, 50 and 75 Å GaAs buffer layers at the P→In interface.

6. Effect of barrier width on carrier transport

Efficient transport of both electrons and holes through the $\text{In}_x\text{Ga}_{1-x}\text{As}/\text{GaAs}_{1-y}\text{P}_y$ superlattice is required for high efficiencies in solar cells containing a superlattice. For the $\text{GaAs}_{1-y}\text{P}_y$ barriers used in this work, the phosphorus composition of $y > 0.65$ means that in both electrons and holes will have barriers of at least 0.3 eV. This makes transport through thermionic emission unfeasible at 300 K and requires that the primary mechanism is some form of tunneling transport. n-GaAs/i-(InGaAs/GaAsP)/p-GaAs solar cell structures will be analyzed both through modeling of EQE and the measurement of EQE and IV of MOCVD grown devices. It will be shown that the primary limitation on transport is the tunneling of electrons, requiring GaAsP of 30 Å or less for near 100% efficient transport through a superlattice of 20 periods or more. Superlattices with thicker barrier layers were found to be useful for determining the minority carrier lifetime in the InGaAs well material.

6.1. Effect of barrier thickness on EQE

6.1.1. Effect of device polarity: importance of electron transport

It was shown in chapter 5 that increasing the thickness of the InGaAs wells lowers the effective band gap of the superlattice due to less severe quantum confinement effects. However, a thicker InGaAs well requires a thicker GaAsP in order to satisfy the strain balance condition [1]. When superlattices with GaAsP barriers thicker than 30 Å are used both the J-V response and EQE show a decrease in performance. Solar cells with p-type emitter and n-type bases (p on n) and n-type emitters and n-type bases (n on p) were grown and modeled in order to determine the source of this decreased performance.

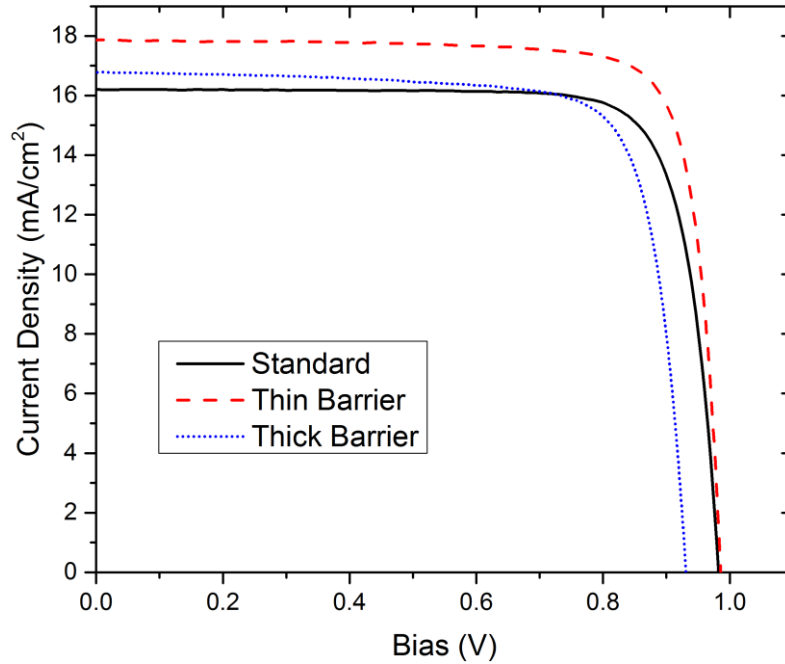


Figure 6.1: J-V response for three solar cell devices: 1. A GaAs standard cell, 2. a device with an $\text{In}_{0.18}\text{Ga}_{0.82}\text{As}/\text{GaAs}_{0.21}\text{P}_{0.79}$ superlattice and 30 Å barrier and 3. the same superlattice with 34 Å barriers.

Figure 6.1 shows the J-V response of three p on n solar cell structures: a GaAs standard, and two $\text{In}_{0.18}\text{Ga}_{0.82}\text{As}/\text{GaAs}_{0.21}\text{P}_{0.79}$ superlattice devices, one with a 30 Å ‘thin’ barrier and one with a 34 Å ‘thick’ barrier. The thin GaAsP barrier device has a similar fill factor and V_{oc} as the standard cell but a higher J_{sc} due to increased absorption. On the other hand, the J_{sc} , V_{oc} , and ff are decreased in the thick barrier device. Similar behavior is seen the J-V response for the n on p devices. What appears to be a low shunt resistance for the thick barrier device is due to the electric field dependence of tunneling through the barriers. The EQE for n on p devices is shown in figure 6.2a, with figure 6.2b is the EQE for the p on n devices that were shown in figure 6.1. The extension due to absorption in the InGaAs wells can be seen in these figures; the larger extension in the thick barrier devices is due to lower quantum size effects from wells which are made thicker due to the strain balancing requirement. For devices of both polarities, the thin barrier devices did not have any decrease in EQE relative to standard cells at wavelengths below the GaAs band edge. The thick barrier devices did show a decrease in EQE but at different wavelengths depending upon the device polarity. For p on n, there is a fairly even decrease at all wavelengths, while for n on p the decrease is more pronounced at longer wavelengths. Both of these results suggest that transport is limited primarily by electrons. For an n on p device, the minority carrier electrons are generated in the base, which absorbs primarily at long wavelengths as the short wavelength light has been filtered by the emitter. Conversely, a p on n

device generates minority carrier electrons in the emitter, which absorbs all wavelengths.

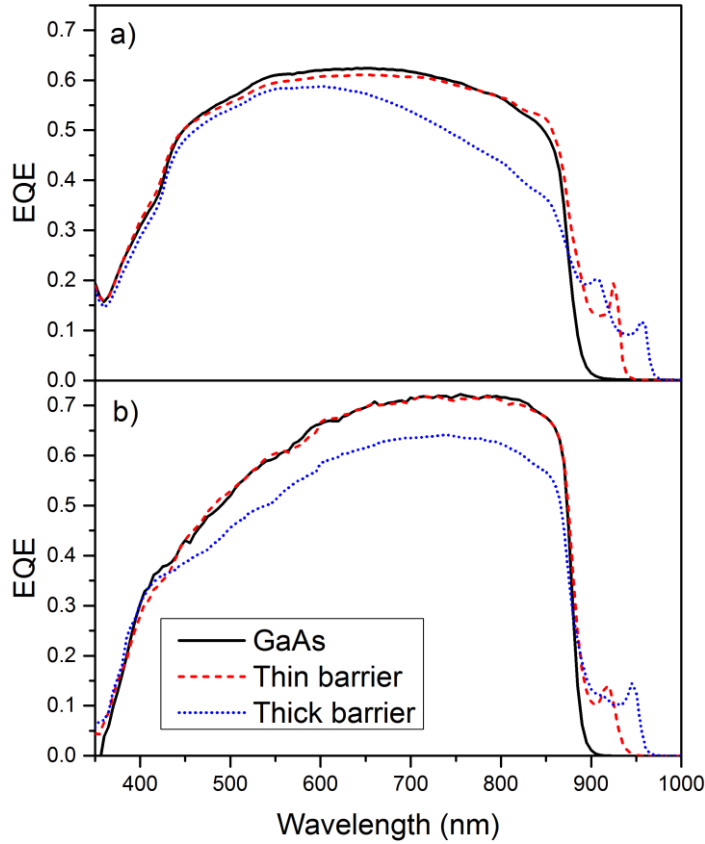


Figure 6.2: Standard, thin barrier and thick barrier solar cell devices with a) n on p polarity and $\text{In}_{0.18}\text{Ga}_{0.82}\text{As}/\text{GaAs}_{0.21}\text{P}_{0.79}$ superlattices and b) p on n polarity and $\text{In}_{0.15}\text{Ga}_{0.85}\text{As}/\text{GaAs}_{0.20}\text{P}_{0.80}$ superlattices.

Carrier transport through the superlattice could occur through two different mechanisms: thermionic emission and tunneling. Thermionic emission occurs when a carrier acquires enough thermal energy such that it can move over the top of the barrier layer. The characteristic lifetime of thermionic emission, τ_{th} , is given by equation 6.1 [2]:

$$\frac{1}{\tau_{\text{th}}} = \sqrt{\frac{kT}{2\pi m_w^* L_w^2}} e^{-E_b/kT} \quad 6.1$$

Thermionic emission depends strongly upon the barrier height, E_b , and the temperature since both parameters are present in the exponential term. There is a weaker dependence on effective mass in the well, m_w^* , and the length of the well, L_w . A superlattice devices that depend upon thermionic emission should have improved performance at elevated temperatures.

Tunneling is a quantum mechanical phenomenon where a carrier can be transported through the barrier even at energies within the band gap of the barrier material. Since the wavefunction has a nonzero amplitude for within barriers of finite potential, there is a chance for the carrier to transfer to the other side of the barrier with the characteristic lifetime given by [3]:

$$\frac{1}{\tau_{tn}} = \frac{n\hbar\pi}{2L_w^2 m_w^*} \exp\left(-\frac{2}{\hbar} \int_0^{L_b} \sqrt{2m_b^*(E_b - Fz)} dz\right) \quad 6.2$$

Equation 6.2 is generalized for a barrier within a constant electric field, F. The most important parameter that determines τ_{tn} is the barrier thickness, L_b , but the barrier height and effective mass in the well, m_b^* , are also important factors.

6.1.2. Effect of temperature and bias on EQE

The importance of barrier thickness on the superlattice device performance was already demonstrated, but in order to determine if there is any thermal component to transport, the EQE was measured while being heated above room temperature. Figure 6.3(a) shows that as the temperature is increased there is an increase in both the superlattice and GaAs absorption at longer wavelengths and an increase in the EQE at all wavelengths above 600 nm. The first phenomenon occurs due to the reduction in the band gap as the lattice expands at higher temperatures. The second effect suggests that there is a thermal component to the carrier transport, but does not necessarily indicate that transport is occurring through thermionic emission. While there is no explicit dependence for tunneling on temperature as given in equation 6.2, the tunneling lifetime will depend upon the energy of a carrier in the well. For a carrier that is at an energy higher than the ground state of the well will at the very least have a shorter barrier height, which should decrease the tunneling lifetime. Additionally, if the barrier/well interface is not abrupt, then it is likely that there will be a shorter barrier width at higher energies. As there will always be carriers at energies above the ground state of the well, the thermal component of tunneling must be investigated when modeling the transport process.

Equation 6.2 includes the dependence of tunneling on the electric field in the superlattice region. Higher electric fields effectively lower the barrier height thus decreasing the tunneling lifetime. One way to increase the electric field in the superlattice is to operate the solar cell at reverse bias. The EQE of the n on p thick barrier device is shown in figure 6.3(b). There is an increase in EQE for both the GaAs and superlattice absorption, indicating that carrier transport is improved due to the higher electric field.

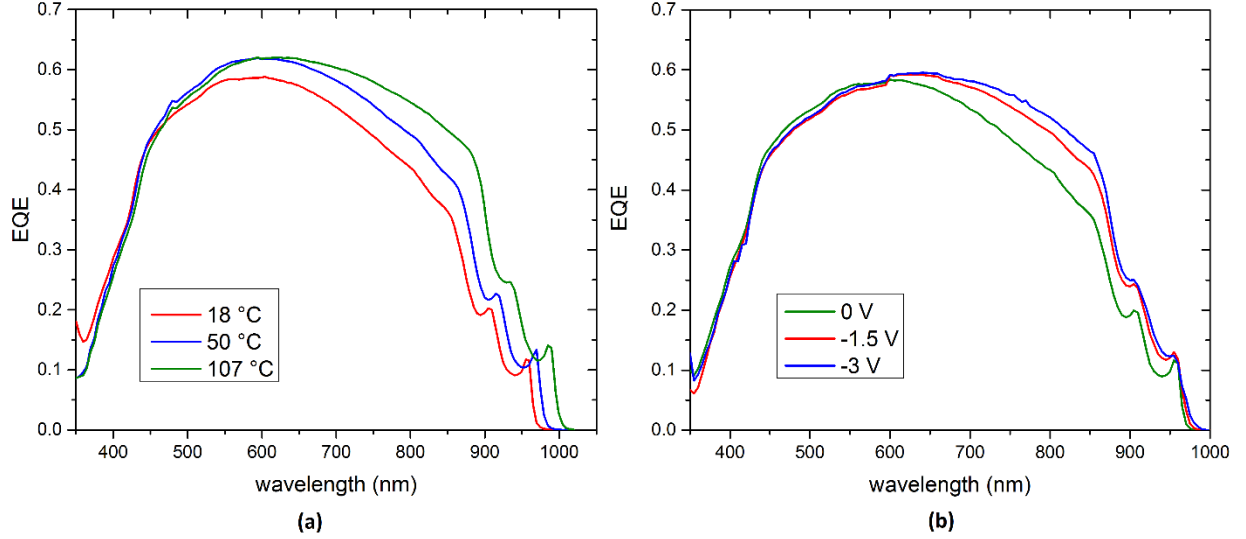


Figure 6.3: EQE of n on p thick barrier superlattice devices as a function of (a) device temperature and (b) reverse bias. Both higher temperatures and larger reverse bias increase the EQE above 600 nm due to an improvement in carrier transport.

6.2. Empirical model for EQE of solar cell devices.

6.2.1. EQE for p-n GaAs structures

In order to determine the processes that are limiting transport through the GaAsP barriers and to determine the carrier lifetime, there are two aspects that must be modeled. The first is to model the EQE using the solutions one-dimensional continuity and drift diffusion equations for the base, emitter and intrinsic layers. Next, the tunneling probability through each barrier layer is found and extended to the entire structure to give P_{tot} , the probability of a carrier traversing the entire MQW system. It will be assumed that the current due to a carrier traversing the intrinsic layer will be reduced in proportion to this probability. A minority carrier generated in the emitter or base must traverse every barrier in the superlattice. Carriers generated in the InGaAs wells pass through fewer barriers which means that P_{tot} depends upon the depth at which the carrier is generated.

The intrinsic MQW region layer was treated as if it were fully depleted. In order to find the total current, the contribution of each layer was considered independently, taking into account the wavelength dependent absorption of the preceding layers. The current produced in the emitter, base and depletion layers was calculated using the analytical solution to the one-dimensional drift-diffusion and continuity equations for a constant doping [4].

$$J_b = \frac{q\phi(1-R)\alpha_b(F_w F_e F_i)}{\alpha_b^2 L_b^2 - 1} \left[\alpha_b L_b - \frac{\frac{S_b L_b}{D_b} \left[\cosh\left(\frac{W_b}{L_b}\right) - e^{-\alpha_b W_b} \right] + \sinh\left(\frac{W_b}{L_b}\right) + \alpha_b L_b + \alpha_b L_b e^{-\alpha_b W_b}}{\frac{S_b L_b}{D_b} \sinh\left(\frac{W_b}{L_b}\right) + \cosh\left(\frac{W_b}{L_b}\right)} \right] \quad 6.3$$

$$J_i = q\phi(1 - R)(F_w F_e)(1 - e^{-\alpha_i W_i}) \quad 6.4$$

$$J_e = \frac{q\phi(1-R)\alpha_e F_w}{\alpha_e^2 L_n^2 - 1} \left[\frac{\alpha_e L_e + \frac{S_e L_e}{D_e} - e^{-\alpha_e W_e} \left[\frac{S_e L_e}{D_e} \cosh\left(\frac{W_e}{L_e}\right) + \sinh\left(\frac{W_e}{L_e}\right) \right]}{\frac{S_e L_e}{D_e} \sinh\left(\frac{W_e}{L_e}\right) + \cosh\left(\frac{W_e}{L_e}\right)} - \alpha_e L_e e^{-\alpha_e W_e} \right] \quad 6.5$$

The subscripts e, i, b and w indicate quantities for the emitter, depletion layer, base and window respectively. ϕ is the incident photon flux in photons/cm²·s, R is the reflectivity of the top surface, F is the fraction of light absorbed by the preceding layers, W is the thickness of a particular layer, α is the absorption coefficient for a particular layer and S, L and D are the minority carrier surface recombination, diffusion length and diffusion coefficients. Since the absorption coefficient is a function of the wavelength of the incident light, each current is also a function of wavelength. The EQE at a particular wavelength can be found from J_e , J_i and J_b from [4]:

$$EQE(\lambda) = \frac{hc[J_b(\lambda) + J_i(\lambda) + J_e(\lambda)]}{q\phi\lambda} \quad 6.6$$

If recombination in the depletion region is ignored, the fraction of carriers collected from the intrinsic layer can be assumed to be 100% for both electrons and holes for the GaAs standard cells and the MQW devices with barriers thin enough to not impede transport. Published values of the doping dependent minority carrier mobility and lifetime in p- and n-type GaAs were used for the base and emitter [5]. The base doping was taken to be 2×10^{17} cm⁻³ while the emitter doping was considered to be 2×10^{18} cm⁻³. The surface recombination velocity at the BSF and window were parameterized to give the best fit to the thin barrier devices; the same value was used in the EQE calculation for the thick barrier devices for each device polarity. Absorption from the window at short wavelengths was also taken into account. Tabulated values were used for the GaAs and AlGaAs absorption coefficients and for the reflection from the AlGaAs window. The absorption in the InGaAs quantum wells was calculated as discussed in section 6.2.2. Tables 6.1 and 6.2 lists the relevant structural and material parameters for the device with an n on p polarity and an In_{0.18}Ga_{0.82}As/GaAs_{0.21}P_{0.79} superlattice and the device with a p on n polarity and In_{0.15}Ga_{0.85}As/GaAs_{0.20}P_{0.80} superlattice.

Table 6.1: Structural and material parameters for the n on p polarity device.

n on p polarity			
Parameter	Symbol	Value	Unit
Window thickness	W_w	310	Å
Emitter thickness	W_e	0.26	µm
Base thickness	W_b	2.0	µm

Table 6.1 continued

Emitter doping	N_d	2×10^{18}	cm^{-3}
Base doping	N_a	2×10^{17}	cm^{-3}
Diffusion coefficient, base	D_b	103	cm^2/s
Diffusion coefficient, emitter	D_e	3.6	cm^2/s
Diffusion length, base	L_b	21	μm
Diffusion length, emitter	L_e	6.0	μm
Surface recombination, base	S_b	1×10^4	cm/s
Surface recombination, emitter	S_e	3×10^6	cm/s
Electron effective mass, well	$m_{e,w}^*$	0.067	m_0^*
Electron effective mass, barrier	$m_{e,b}^*$	0.117	m_0^*
Hole effective mass, well	$m_{h,w}^*$	0.082	m_0^*
Hole effective mass, barrier	$m_{h,b}^*$	0.152	m_0^*

Table 6.2: Structural and material parameters for the n on p polarity device.

p on n polarity			
Parameter	Symbol	Value	Unit
Window thickness	W_w	450	\AA
Emitter thickness	W_e	0.50	μm
Base thickness	W_b	1.7	μm
Emitter doping	N_a	2×10^{18}	cm^{-3}
Base doping	N_d	2×10^{17}	cm^{-3}
Diffusion coefficient, base	D_b	5.7	cm^2/s
Diffusion coefficient, emitter	D_e	65	cm^2/s
Diffusion length, base	L_b	17	μm
Diffusion length, emitter	L_e	6.1	μm
Surface recombination, base	S_b	1×10^4	cm/s
Surface recombination, emitter	S_e	1×10^6	cm/s
Electron effective mass, well	$m_{e,w}^*$	0.060	m_0^*
Electron effective mass, barrier	$m_{e,b}^*$	0.117	m_0^*
Hole effective mass, well	$m_{h,w}^*$	0.074	m_0^*
Hole effective mass, barrier	$m_{h,b}^*$	0.152	m_0^*

Figure 6.4 shows the measured EQEs for both p-on-n and n-on-p GaAs devices along with the modeled EQEs with the best fit for surface recombination at both the window and the BSF interfaces. The modeled contribution to the EQE from the emitter, base and depletion regions are also shown on the plot. Since the depletion region is thin for the standard devices it contributes the smallest amount to the EQE. The EQE for short wavelengths is almost entirely due to the emitter. In both cases the EQE at short wavelengths comes almost entirely from current in the emitter since the absorption coefficient is high in this region. The depletion region contribution is highest for the n-on-p device since the emitter is made thinner (0.2 μm for n-on-p versus 0.5 μm for p-on-n) due to the shorter minority carrier diffusion length for holes compared to electrons.

6.2.2. Calculation of absorption in MQW structures

The absorption in the GaAs base and emitter and AlGaAs window can be found using published values for the absorption coefficient. However, absorption in the InGaAs quantum wells must be calculated since the absorption will depend upon the superlattice structure as well as the InGaAs composition.

6.2.2.1. Single-carrier absorption

Unlike a three dimensional semiconductor, if the incident light is oriented in the same direction as the envelope function of a quantum well then the absorption coefficient depends upon the thickness of the well and barrier layers as well as the material composition of the layers [6]. Thus, each superlattice can be treated as a unique material with a characteristic absorption spectrum. Nevertheless, for a particular set of quantum wells and barriers an effective absorption coefficient can be calculated in order to use equations 6.3-5 to find the EQE.

For a quantum well the strongest transitions are between electron and hole states with the same quantum number, with the n=1 state for electrons and holes giving the lowest energy for absorption. For a two dimensional structure the absorption has a staircase lineshape with abrupt increases in absorption corresponding to the n=1,2,3,etc. states. The wavelength dependent magnitude of absorption is given by [6]:

$$\alpha(\lambda) = \frac{q^2 E_p \lambda}{8nc\varepsilon_0 \pi L_w \hbar^3} \frac{m_e m_{hh}}{m_e + m_{hh}} \int_{-\infty}^{\infty} \psi_{hh}^* \psi_e dz \quad 6.7$$

Where L is the length of the quantum well, ψ_{hh} and ψ_e are the wavefunctions for the heavy hole and electron states and E_p is the Kane matrix element which has a value of 23 eV. A similar expression is

used for the light hole states with E_p replaced with $E_p/3$ due to difference in selection rules for the heavy hole to electron transition versus the light hole to electron transition.

6.2.2.2. Excitonic absorption

The reduction of dimensionality in the quantum wells results in excitonic states that have much longer than is found in three dimensional semiconductors. The measured EQEs of superlattice devices in figures 6.2 and 6.3 show clear excitonic features in the superlattice absorption region. To accurately model the EQE, these excitonic absorption features must be included.

An exciton behaves similarly to the hydrogen atom with the proton replaced with a heavy hole. Just as an electron bound in a hydrogen atom has a lower potential energy compared to a free electron, the excitonic state will be at a lower energy relative to the band gap of free carriers. The exciton energy can be found using the Bohr model with the carrier masses replacing the free electron and proton mass and the semiconductor permittivity replacing the vacuum permittivity. The exciton radius, ρ , is the radius which gives the lowest binding energy for the exciton state and once found can be used to calculate the exciton wavefunction and absorption. Since the exciton behaves as a 1s hydrogen state ψ is given in polar coordinates [6]

$$\psi_{ex}(r) = \sqrt{\frac{2}{\pi\rho^2}} e^{-r/\rho} \quad 6.8$$

$$\alpha_{ex}(\lambda) = \frac{q^2 E_p \lambda}{4\pi^2 n c^2 m_0 \epsilon_0 \hbar L_w \rho^2} \int \psi_{ex}^* \psi_{ex} dz \quad 6.9$$

Where ρ is the Bohr radius of the exciton ground state and the other parameters are the same as for the bulk absorption. This gives the excitonic absorption strength as an impulse function at the exciton binding energy. In real systems there is a broadening of this impulse due to factors such as non-absolute zero temperatures and roughness at the quantum well interfaces [7]. Since these features are difficult to characterize, the excitonic absorption was treated as a Gaussian distribution. The impulse function was broadened to give the same width at half height as the excitonic absorption peak in the EQE. These range from 12 to 17 meV for the n=1 exciton and the n on p thick barrier device has a width of 27 meV for the n=2 exciton.

6.2.3. EQE of MQW solar cell structures

Figure 6.4(a) shows modeled EQE of the thick barrier device for the n on p polarity, while 6.4(b) is the same result for the p on n polarity. The calculated contribution from the emitter, base and intrinsic layer are shown, along with the measured EQE for each device. As expected, the EQE is accurately

modeled as reduction in the current from the layer with minority carrier electrons, since the EQE was calculated with the full current for n-type layers but a lower current in the p-type and intrinsic layers. If the minority carrier holes were lost to recombination, the emitter current would be reduced in the n on p structure. A decrease in the EQE at the blue end of the spectrum can only be caused by decrease in current from the emitter, but no such decrease is seen for the thick barrier device relative to the thin barrier device. The discrepancy between the hole and the electron tunneling is likely due to the deeper well in the conduction band relative to the valence band. For instance, the conduction band offset for an $\text{In}_{0.14}\text{Ga}_{0.86}\text{As}/\text{GaAs}_{0.25}\text{P}_{0.75}$ structure is 0.55 eV, while the valence band offset is 0.36 eV. These were found using the calculated valence band offsets of Wei and Zunger [8] due to the lack of experimentally determined valence band offsets in the InGaAs/GaAsP material system. This may become an issue for devices that use InGaAs wells with InAs fractions that exceed 20%, since P_{tot} will be effected both by a decreased tunneling probability and a decreased recombination lifetime. It is also evident that the p on n devices are more strongly effected by poor electron tunneling since a larger amount of current is generated in the emitter than the base or intrinsic layer. It is expected that any device which uses an InGaAs/GaAsP heterostructure and depends upon minority carrier generation in a p-type region will be particularly sensitive to the barrier thickness in the heterostructure.

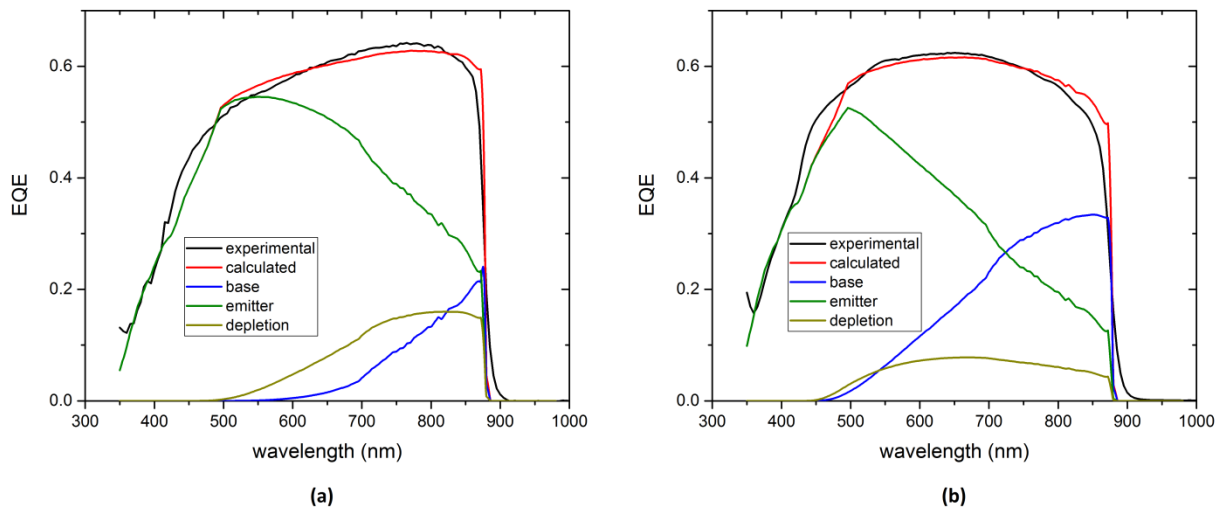


Figure 6.4: Experimental and modeled EQE for a GaAs with a) an n on p polarity and b) a p on n polarity. Also shown are the contributions to the EQE from the emitter, base and depletion region.

6.2.4. Determination of recombination lifetime from EQE modeling

The EQE of the thick barrier devices depends upon the escape probability from each individual well and the superlattice as a whole. If there is a low probability of escape from the well then carriers can

recombine before they can traverse the entire superlattice, The escape probability of a carrier from a single well is found using the tunneling escape lifetime from the well, τ_{tn} , along with the recombination lifetime in the well, τ_r , by [9]:

$$P = \tau_{tn}^{-1} / (\tau_{tn}^{-1} + \tau_r^{-1}) \quad 6.10$$

The total probability of transport through the multiple quantum well structure is the product of the probabilities of tunneling through each barrier, which gives $P_{tot} = P^N$ for N barriers of equal thickness. For thin barrier devices it was assumed that $\tau_{tn} \ll \tau_r$, which means that P_{tot} can be taken as 100% for these structures. This will be confirmed when the recombination lifetime is determined from the EQE of the thick barrier devices. In order to find the recombination lifetime it is first necessary to find the tunneling lifetime for each MQW system.

Where L_w and m_w^* are the length and effective mass in the well and L_b and m_b^* are the same parameters in the barrier. The confined state energies were found by solving the Schrödinger equation for a finite well in an electric field using a perturbed wavefunction. From Eqn. 6.9 it can be seen that the tunneling lifetime will be shorter for carriers at a higher energies in the quantum well since the tunneling barrier will be smaller. So while the population of carriers at higher energies may be small, they can contribute significantly to the tunneling lifetime. The overall lifetime for carrier escape from a particular well can be found by averaging the tunneling lifetime across the distribution of carriers in the well using the expression in Eqn. 6.10 along with the energy dependent tunneling lifetime from Eqn. 6.9. The two-dimensional quantum well density of states, $\rho(E)$, is a step function which uses the previously determined energy states and $f(E)$ is the Fermi distribution.

$$\frac{1}{\tau_{tn}} = \frac{\int \frac{1}{\tau_{tn}(E)} \rho(E) f(E) dE}{\int \rho(E) f(E) dE} \quad 6.11$$

The expression in Eqn. 6.11 was originally stated in terms of the average carrier velocity, v , but also can be given as the average of tunneling lifetime ($1/\tau_{tn} = v/L_w$) when thermionic emission is insignificant and the wells are of uniform thickness. As conduction band offsets for all of the devices under investigation are in excess of 0.5 eV, this is a reasonable assumption.

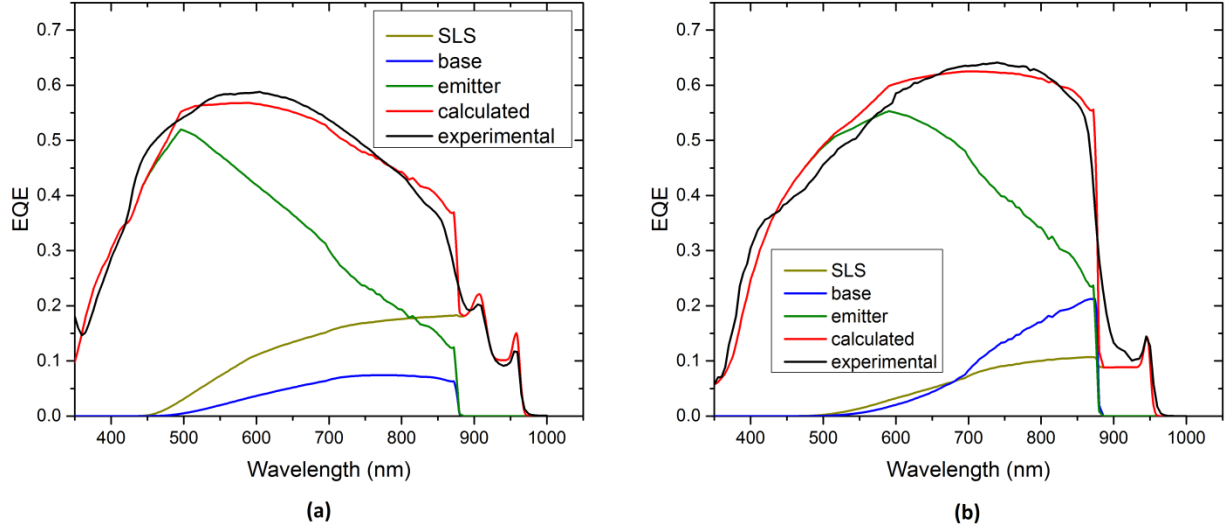


Figure 6.5: The modeled and measured EQE for thick barrier devices with a) an n on p polarity and b) a p on n polarity. The EQE contributions from the base, emitter and SLS layers are included. P_{tot} was adjusted to give the best fit to the measured EQE.

The modeled EQE for the thick barrier devices is given in figure 6.5. Equations 6.3-5 were used to find the EQE contribution from each layer using the same surface recombination velocity as was found for the standard devices in section 6.2.3. Since transport is limited by electron transport, the EQE from the p-type layer is assumed to be reduced by P_{tot} while the EQE from the superlattice is reduced by half as much. This is because electrons are generated throughout the SLS and will not pass through all the barriers while those generated in the emitter or base must pass through all the barriers. The values of P_{tot} that best fit the measured EQEs were found to be 0.60 for the n on p and 0.91. The same analysis was done for the thin (30 Å) barrier devices which showed a P_{tot} close to 1 for both device polarities. Once P_{tot} and τ_{in} were found, the recombination lifetime was calculated from equation 6.10.

Table 6.3 Calculated tunneling lifetime, transmission probability and recombination lifetime of electrons for various device polarities and GaAsP barrier thicknesses. Each device has 40 superlattice periods.

Sample	L_b (Å)	τ_{in} (ps)	P_{tot}	τ_r (ns)
Thin barrier, n on p	25	6.8	0.999	110
Thick barrier, n on p	41	2800	0.608	110
Thin barrier, p on n	30	14	0.991	25
Thick barrier, p on n	34	130	0.917	25

The τ_{in} , τ_r and P_{tot} for each device are shown in table 6.3. The recombination lifetimes are close to

those measured in metamorphic InGaAs/GaInP heterostructures by time resolved photoluminescence (TRPL) [10]. This suggests that the interface between the GaAsP and InGaAs layers is largely free from defects, as a much larger decrease in recombination lifetime would be expected if dislocations were formed due to relaxation of either well or barrier layers. It is also in agreement with previous results by x-ray diffraction, which show no linewidth increase in thick barrier structures due to defects. The difference in the lifetime for the two polarities can be attributed to the composition of InGaAs used in the well material, with the shorter lifetime observed in the InGaAs layers with a higher indium fraction, due to the lower band gap. Using these recombination lifetimes with the calculated τ_{in} for the thin barrier devices gives calculated values of P_{tot} close to 1, as table 6.3 indicates.

The EQE of the thick barrier n on p device was also calculated for the effect of higher temperatures as shown in figure 6.6. The modeled EQE is compared to the same results that were given in figure 6.3(a). The absorption coefficients used the room temperature values shifted in energy by the same amount as the change in the band gap of GaAs due to temperature (a reduction of 15 meV for 50 °C and 41 meV for 107 °C). The minority carrier hole and electron mobility have been shown to have a $1/T$ temperature dependence, which is taken into account for the calculation of the modeled EQEs, but it is assumed that the surface recombination velocities for both holes and electrons is the same as at room temperature. P_{tot} increases as the temperature increases and is 0.61 at 18 °C, 0.82 at 50 °C and 0.95 at 107 °C.

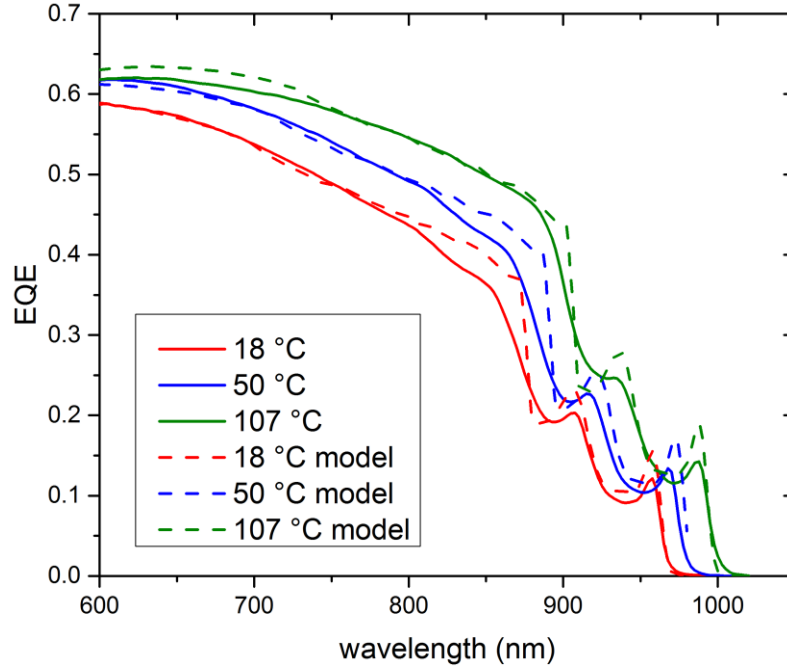


Figure 6.6: Modeled and measured EQEs for the n on p thick barrier device at several temperatures. The value of P_{tot} increases with increasing temperature and is near 1 at 107 °C.

Figure 6.7 shows the modeled and measured EQE for several values of reverse bias. There is an increase in P_{tot} as the reverse bias is increased due to two factors: 1) the reduction in the effective barrier height at larger electric fields as shown in equation 6.2 and 2) an increase in the electron state levels due to the Stark effect in the InGaAs wells. The second factor effectively reduces the barrier height since the ground state of the electron is at a higher point in the well relative to the ground state at a lower electric field. The value of P_{tot} increases from 0.61 at no reverse bias, 0.85 at a reverse bias of -1.5 V and 1 at a reverse bias of -3.0 V.

7. InGaP/GaAs/AlGaAs tunnel junctions

7.1. Growth of highly doped materials

A tunnel diode requires very high doping levels in the region near the junction for two reasons: 1) in order for there to be an overlap between the p side valence band and the n side conduction band, both the n and p materials must be degenerately doped and 2) the tunneling width is shorter when the depletion width is smaller. Since the tunneling current is strongly dependent on the tunneling distance, the depletion region must be made as thin as possible. Determining the growth conditions that maximize the effective doping in each layer in the junction is essential.

7.1.1. Te doping in InGaP

A particular challenge for the InGaP growth is that not present for the other tunnel junction materials, GaAs and AlGaAs, is the need to balance the flow of TMGa and TMIn in order to fulfill the lattice matching condition to the GaAs substrate. This is further complicated by the effect of tellurium doping on the incorporation of indium. It has been found that increasing the DETe flow will increase the fraction of indium relative to gallium in the lattice even when the TMGa and TMIn flows are unchanged [1]. To find the effective n-type doping the InGaP was grown 0.5 μm thick on undoped GaAs substrates. A Te doped GaAs cap was grown 0.3 μm thick to serve as a contact layer for Hall measurements and to prevent the exposure of phosphorus containing materials to air when the sample was removed from the growth chamber. To determine the InGaP thickness the GaAs cap was first etched with a 4:1:1 water/ NH_3 / H_2O_2 mixture followed by an HCl etch for the InGaP. The thickness was measured on a IIA Dektak profilometer and the lattice constant was found using x-ray diffraction measurements. The large Te atoms distort the InGaP lattice, resulting in a larger lattice constant in comparison to an undoped material with the same composition [2]. As a result, a lattice matched Te doped InGaP will have a lower fraction of indium in the lattice compared to undoped InGaP.

The highest doping of Te in InGaP was $1.9 \times 10^{19} \text{ cm}^{-3}$, with a V/III ratio of 42 and a growth temperature of 560 °C. Similar results were achieved for InGaP grown at 580 °C. These results are notable since other efforts to achieve high doping in this material system have not exceeded $1.1 \times 10^{19} \text{ cm}^{-3}$. There are several possible reasons for these unprecedented results. One is that the growth rates were very high, ranging from 7 to 9 \AA/s . InGaP layers grown at a lower growth rate (2 \AA/s) were found to have an effective doping of $1.1 \times 10^{19} \text{ cm}^{-3}$. Also, the use of TBP as a phosphorus precursor is unusual, all of the previously reported results used phosphine. For subsequent device modeling, the doping in the InGaP will be assumed to be $1.6 \times 10^{19} \text{ cm}^{-3}$ for thick InGaP layers.

7.1.2. Te doping in GaAs

Te doped with GaAs is necessary for the growth of high J_{pk} TJ as will be demonstrated later. Unlike InGaP, there is no need to adjust the precursor flows to insure lattice matching to the GaAs substrate. The incorporation of Te increases the lattice constant as with the InGaP, resulting in a slightly compressively strained material. However, there is no evidence for crosshatching even in layers as thick as 0.5 μm . Since the highly doped GaAs is grown no more than 100 \AA thick in TJ structures, there is no potential for the formation of defects due to relaxation of the crystal lattice.

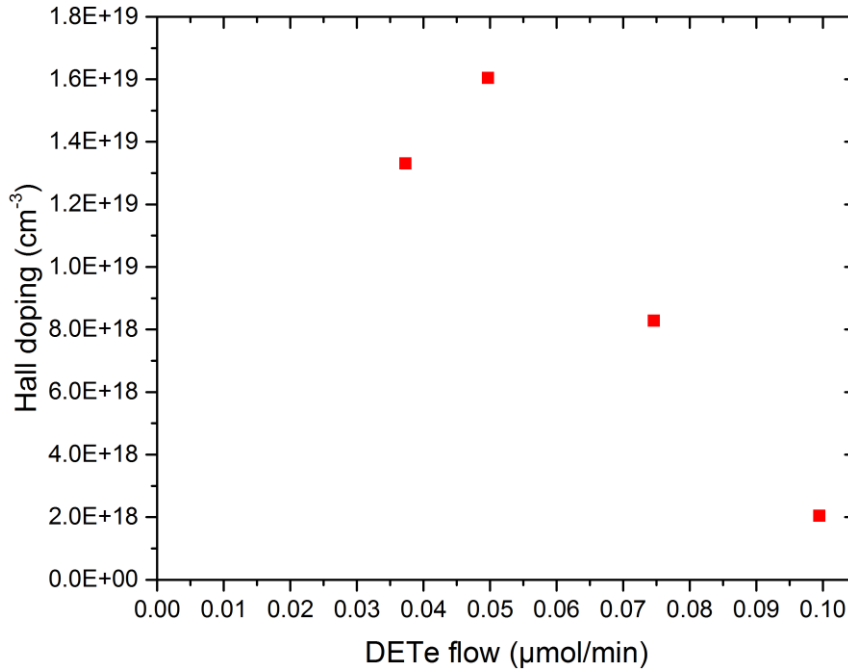


Figure 7.1: Hall n-type doping versus DETe flow for GaAs

In order to maximize the doping in the GaAs, it is necessary to determine the ideal flow for the DETe. As figure 1, shows the effective doping cannot be increased indefinitely by increasing the DETe flow. The maximum doping obtained in this series is for a DETe flow of 0.05 $\mu\text{mol}/\text{min}$ at a growth temperature of 580 $^{\circ}\text{C}$ and a V/III ratio of 30. Higher doping levels were obtained by lowering the temperature to 560 $^{\circ}\text{C}$ and the V/III ratio to 10 and 15, with the Hall doping measured as $2.2 \times 10^{19} \text{cm}^{-3}$ in both cases. GaAs layers with very high DETe flows (0.45 $\mu\text{mol}/\text{min}$) were found to have very high resistances between In contacts such that it was impossible to carry out Hall effect measurements. While these results show that it is possible to achieve high doping levels, it is likely that these results do not reflect the actual effective doping in the GaAs at the InGaP/AlGaAs interface of the tunnel junction. The well documented carryover of Te in GaAs and InGaP makes it difficult to control in the thin GaAs ($<50 \text{\AA}$) layer without the use of growth pauses. It will be shown later that

high doping levels in the GaAs are not necessary to produce a large J_{pk} in the tunnel junction, and in some cases the TJ performance will increase when the GaAs doping is low.

7.1.3. C doping in AlGaAs

The single p-typed doped material is carbon doped AlGaAs with carbon tetrabromide (CBr_4) as the dopant precursor. As with the Te, the high concentration of carbon in the AlGaAs lattice results in a shift in the lattice constant relative to the undoped material [3], making determination of the aluminum composition difficult. One difference with the carbon doping is that the CBr_4 also acts as an etchant for the growing AlGaAs layer. A higher flow of the CBr_4 will decrease in the growth rate of the AlGaAs. The AlGaAs also exhibits the same self-compensation that was seen the Te doped GaAs.

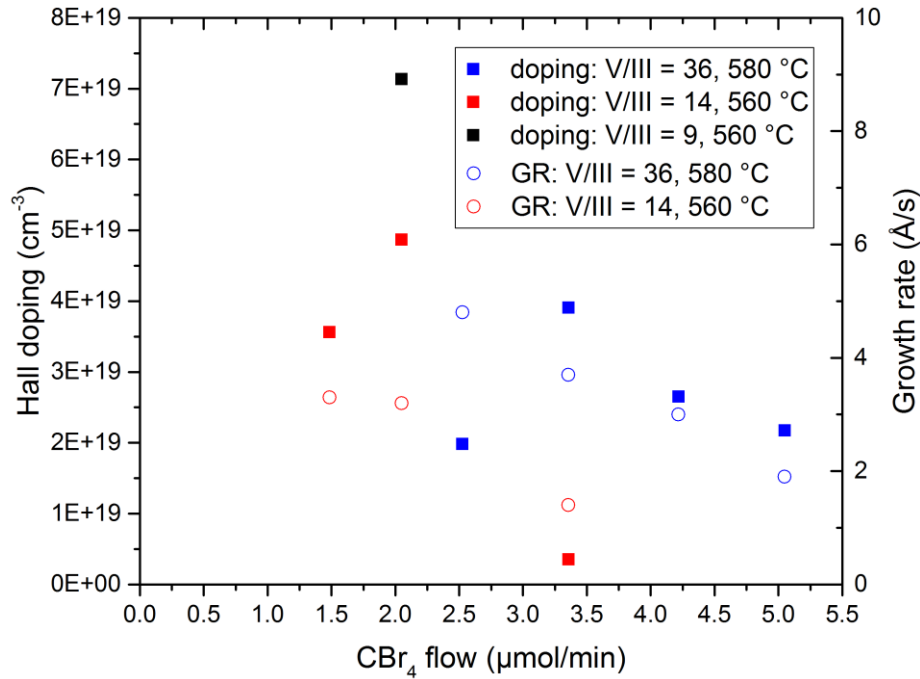


Figure 7.2: Hall p-type doping and growth rate versus CBr_4 flow for AlGaAs

Figure 2 shows the effect of CBr_4 flow on both the effective p-type doping and the growth rate of the AlGaAs. As expected, there is a decrease in the growth rate as the CBr_4 flow is increase. As with the Te doping in GaAs, there is a maximum doping for a particular set of growth parameters. This maximum doping was increased by lowering both the growth temperature and the V/III ratio. A doping level of $7.1 \times 10^{19} \text{ cm}^{-3}$ was achieved with a growth temperature of 560 °C, a V/III ratio of 9, a growth rate of 2.5 Å/s and a CBr_4 flow of 2.05 $\mu\text{mol/min}$. For subsequent modeling, a doping level of $7.0 \times 10^{19} \text{ cm}^{-3}$ will be used.

7.2. InGaP/AlGaAs tunnel junctions

The primary motivation for growing an n^+ -InGaP/ p^+ -AlGaAs TJ in an InGaP/GaAs/Ge MJ structure is for use as a low resistance, transparent contact between the top and middle subcells [4]. The low resistance and transparency requirements are necessary to prevent losses in efficiency as discussed in chapter 3. Historically, the difficulty of achieving sufficiently high doping in the high band gap semiconductors has led to the use of n^+ -GaAs/ p^+ -AlGaAs and n^+ -GaAs/ p^+ -GaAs structures where a decrease in short circuit current and hence a reduction in maximum efficiency was accepted in order to operate the MJ cell at high solar concentration. The objective of this work is to develop an InGaP/AlGaAs device that reduces the efficiency loss from absorption while having a J_{pk} high enough to allow the MJ cell to be operated at concentrations as high as 2000 suns. The TJ should also be able to operate after exposure to the thermal conditions that are present during the growth of the InGaP top cell, which is typically grown at a temperature of at least 650 °C for 30 minutes or more.

Figure 3 shows the J-V response from several points on an InGaP/AlGaAs tunnel junction. X# mesas were fabricated on the 14 mm × 14 mm substrate, each with $y \mu\text{m} \times y \mu\text{m}$ dimension. The largest peak tunneling current for this device is 18 A/cm², which corresponds to 1200 suns for a multijunction cell with a one sun J_{sc} of 15 mA/cm². A number of other mesas were also tested, but had a lower J_{pk} . This device was grown at 580 °C and was not exposed to the thermal conditions of the top cell growth, which would likely reduce J_{pk} . There are several potential reasons for the poor performance of this structure: 1) tellurium carryover. The carryover of Te and InGaP is well documented. While the behavior of Te in AlGaAs is not as well known, the doping compensation from a carryover of a few angstroms could have a significant impact on J_{pk} . 2) Phosphorus carryover. In chapter 5 it was shown that there is a carryover of the phosphorus during the transition from GaAsP to InGaAs. It is possible that there is a similar carryover of phosphorus from the InGaP into the AlGaAs to produce a thin layer of AlGaAsP at the junction interface. This material would have a lower hole effective mass than the AlGaAs and also may have a lower effective p-type doping. 3) Poor physical properties in InGaP for tunneling. As seen in sections 7.1.1 and 7.1.2, the maximum effective n-type doping is lower in the InGaP than the GaAs. In addition, the effective mass of both electrons and holes is larger in InGaP than GaAs [5]. In order for the InGaP/AlGaAs TJ to be usable at high solar concentration, these issues must be addressed.

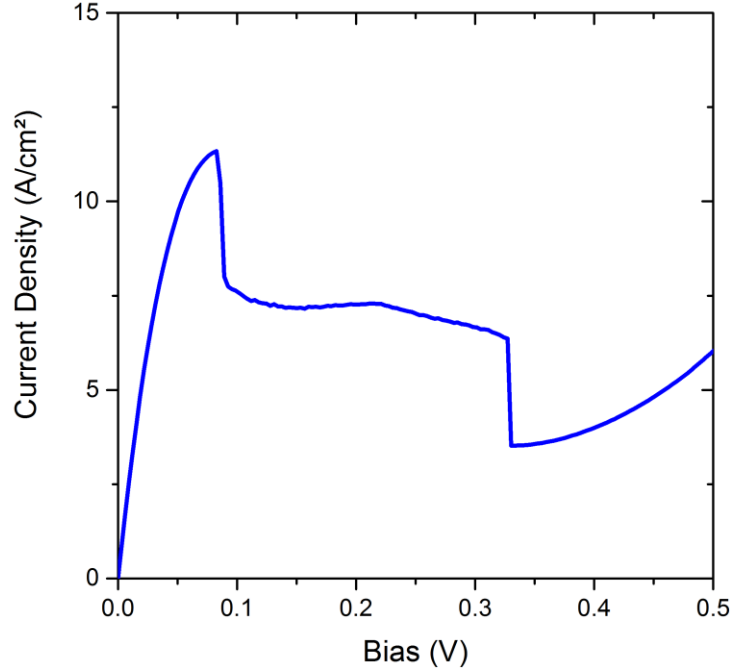


Figure 7.3: J-V response of an InGaP/AlGaAs tunnel diode

7.3. The addition of a GaAs interfacial layer to InGaP/AlGaAs tunnel junctions

To address the issues presented in section 7.2, a thin n-doped GaAs layer was added to the InGaP/AlGaAs interface. Attempts to add a 20 second growth pause under a TBP overpressure failed due to the poor surface morphology of the resulting TJ. Unlike the GaAs/AlGaAs TJ structures, this GaAs is thin, less than 50 Å. Table 7.1 shows the calculated effect of the GaAs absorption on efficiency for various GaAs layer thicknesses. The potential reduction in efficiency is much less than that for a traditional GaAs/AlGaAs TJ, which will have several hundred angstroms of GaAs. Also, a very thin GaAs layer at the junction is likely to have a lower absorption coefficient than that of a thick GaAs layer due to the large electric field near the junction. Efficiency losses are expected to be minor, no more than 0.2% for a 50 Å GaAs layer.

Table 7.1: Absorption losses from GaAs in top tunnel junctions. A typical TJ will have a 200-500 Å thick GaAs layers [6,7].

GaAs thickness (Å)	J_{sc} (A/cm ²)	Efficiency (%)
0	14.50	40
30	14.46	39.9
50	14.43	39.8
100	14.36	39.6
200	14.22	39.2
500	13.94	38.6

7.3.1. The effect of GaAs thickness

While the effect of the GaAs absorption is expected to be minor, it is desirable to determine the minimum thickness of GaAs required to achieve the 30 A/cm^2 peak current density that corresponds to a concentration of 2000 suns. Furthermore, it is unknown if the TJ performance is improved strictly by increasing the GaAs thickness; there is the possibility of an ideal thickness where J_{pk} is maximized. To test this idea, n-InGaP/n-GaAs/p-AlGaAs tunnel junctions were grown with 15, 30 and 45 Å GaAs layers. Figure 4 shows the peak tunneling current for several mesas on each structure, along with the InGaP/AlGaAs TJ from section 7.2. The best performance is for the device with a 30 Å GaAs layer, with a somewhat lower J_{pk} for the device with 45 Å of GaAs. However, the performance for these two structures is significantly better than that of either the 0 Å or the 15 Å GaAs device.

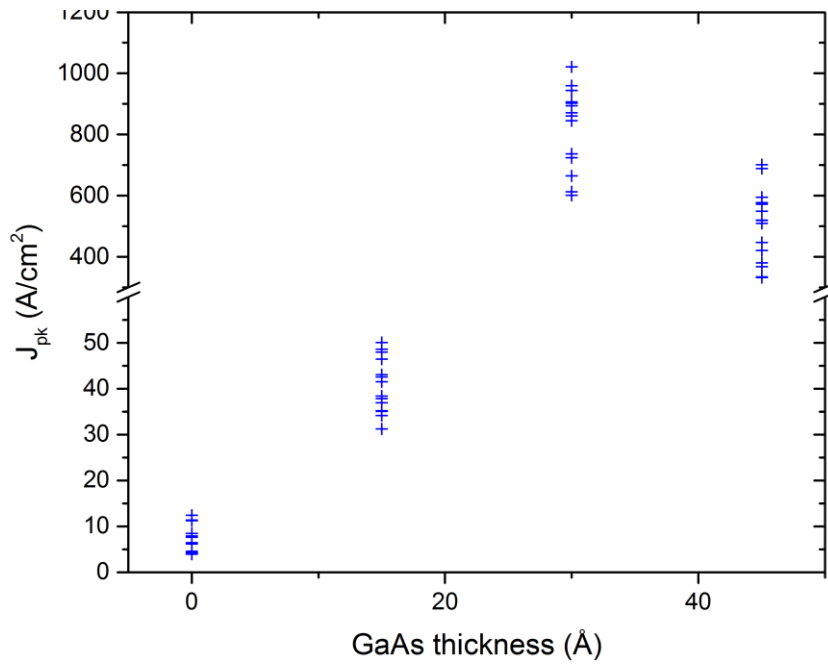


Figure 7.4: Peak tunneling current for an n-InGaP/n-GaAs/p-AlGaAs TJ for several GaAs thicknesses

For each of these devices the flow of the DETe was the same as that in the InGaP, $0.22 \mu\text{mol/min}$. As noted in section 7.1.2, thick GaAs layers with this DETe flow could not be analyzed by Hall effect measurements due to a large resistance between indium contacts. With this in mind, devices were grown with a 30 Å GaAs layer with the DETe flow set to $0 \mu\text{mol/min}$. This has resulted in devices with J_{pk} as high as 600 A/cm^2 . Two possible explanations for this behavior are that either the memory effect of Te is significant enough to dope the GaAs to an acceptably high level over the short GaAs growth period or that a high doping is not necessary in the GaAs. Similarly, devices were grown with

DETe flow shut off at various intervals before the initialization of GaAs growth. This delay period was set to as much as 8 seconds, which corresponds to a thickness of 40 Å with no DETe flow with growth rate of 5 Å/s. This device was found to have a J_{pk} of 42 A/cm². A total of 70 Å of InGaP and GaAs was grown without any DETe flow to the reactor, suggesting that the tellurium memory effect is present in these devices.

7.3.2. Annealing of InGaP/GaAs/AlGaAs tunnel junctions

While the AlGaAs/GaAs/InGaP TJ has been grown at temperatures of 560 and 580 °C, in a multijunction solar cell this structure will be subject to temperatures between 650 and 700 °C for periods as long as 30 minutes during the growth of the InGaP top cell. Thus any tunnel junction must be able to survive the diffusion of both n-type and p-type dopants during this period. Tellurium and carbon were chosen as dopants for this reason as they have a lower diffusion coefficient in this temperature range compared to other typical dopants of III-V materials [1,8]. To test the performance of the TJ under simulated top cell growth conditions, the InGaP/GaAs/AlGaAs structure with a GaAs layer thickness of 30 Å was annealed under a TBA overpressure of 300 µmol/min for 30 min at 650, 675 and 700 °C. There was a complete loss of tunnel diode characteristics in each case. A possible explanation for these results is that the Zn used as a dopant for the contact layer diffused into the junction [9], resulting in a compensation of the n-type semiconductors. A sample with the Zn layer removed was annealed under more moderate conditions of 625 °C for 15 min. Even then, J_{pk} decreased from 456 A/cm² before the annealing to 104 A/cm². Another approach was used to perform the annealing immediately after the growth without the removal of the chamber. After annealing at 650 °C for 30 minutes, the Zn doped cap was grown at a lower temperature, 560 °C in order to limit diffusion. Again, a device that had a J_{pk} of 602 A/cm² before annealing resulted in a complete loss of tunnel junction characteristics afterwards.

The InGaP/GaAs/AlGaAs had given promising results for achieving a high J_{pk} for use as a low resistance contact in MJ solar cells. However, its behavior after the growth of the InGaP cell must be improved for it to be of any practical use. The objective of the remainder of this chapter is to develop a theoretical model for the tunneling characteristics that explains both the high J_{pk} observed in unannealed samples and the rapid degradation of the same devices at high temperatures.

7.4. Modeling of tunneling current

There are several models for calculating the current in a tunnel junction. The simplest model is the Kane model, which calculates the current using the properties of the n- and p-type materials. It was developed in 1960 for a homojunction diode [10], and later modified for to model an InGaP/AlGaAs

heterojunction [11], but it does not include all of the details of the InGaP/GaAs/AlGaAs structure such as changes in tunneling width due to band offset between the GaAs and AlGaAs. Efforts to apply local tunneling models with trap assisted tunneling (TAT) to n-GaAs/p-GaAs structures have given results that agree with experimental results, but these results often use trap effective masses that best fit the experimental data since these parameters have not been reported in the literature [12]. Non-local TAT models have been used to explain the excess current, but this is not relevant to the use of tunnel junctions in multijunction solar cells since they operate a low bias where non-local TAT is not significant [13]. The direct tunneling model of Esaki [14], using a transfer matrix method to calculate the tunneling probability, was found to underestimate the tunneling current compared to the experimental results. Two variations of this model were used to explain the high J_{pk} : one that accounted for resonant tunneling through defects and another that assumed that a large doping spike was present at the InGaP/GaAs interface.

7.4.1. Kane model

The Kane model was developed by Kane [10] and Keldysh [15] and is the most computationally simple of the models as it only requires the material properties, the magnitude of the doping and the applied bias of the junction to calculate. It only considers the direct tunneling at a constant energy and so does not attempt to model the excess current. The primary approximation is that there is a constant electric field in the depletion region and no electric in the neutral regions. Tunneling occurs for electrons and holes that are between the energy levels at n-type conduction band energy, E_1 , and and the p-type valence band energy, E_2 , with the current dropping to zero at sufficiently large forward bias. The bias dependent current can be calculated from a slightly modified form given by Hauser:

$$J = A e^{-BE_b^{3/2}/\mathcal{E}\bar{E}} \frac{\bar{E}}{2} \int_{E_1}^{E_2} [f_c(E) - f_v(E)] [1 - e^{-2E_s/\bar{E}}] dE \quad 7.1$$

$$A = \frac{qm^*}{2\pi^2\hbar^3}, B = \frac{\pi(m^*)^{1/2}}{8^{1/2}q\hbar}, \bar{E} = \frac{32^{1/2}q\hbar\mathcal{E}}{3\pi(m^*)^{1/2}E_b^{1/2}} \quad 7.2$$

Where E_b is the tunneling barrier height, \mathcal{E} is the electric field in the depletion region, f_c and f_v are the Fermi-Dirac functions for electrons and holes, respectively, m^* is the mean effective mass and E_s is the difference between E and the closest of the two band edge energies (E_1 or E_2). The electric field in the depletion region can also be written in terms of the tunneling distance, W as $\mathcal{E} = E_b/qW$.

The effect of high doping on the band energies of both the n-type and p-type materials must be taken into consideration. The addition of shallow donor and acceptor states results in a narrower band gap. Separate expressions have been given for shift in the majority and minority band energies [16,17]:

$$\Delta E_{min} = \frac{q^2}{4\pi\epsilon} \sqrt[3]{\frac{q\pi N}{2}}, \Delta E_{maj} = \frac{3q^3}{16\pi\epsilon} \sqrt{\frac{N}{\epsilon kT}} \quad 7.3$$

Where N is either the donor or acceptor doping level.

While the terms of equations 7.1 and 7.2 are straightforward for a homojunction, some of them must be defined for the InGaP/AlGaAs tunnel junction. First, the tunneling barrier strictly depends upon the band gap of both materials. However, since the AlGaAs is typically doped at much higher levels than the InGaP, the majority of the tunneling will occur on the n-type side of the junction, which means that E_b can be taken to be the band gap of the InGaP. Similarly, m^* will depend primarily upon the effective mass of holes and electrons in the InGaP. Heavy holes are much heavier ($0.60m_0$) than light holes ($0.14m_0$) [5], so tunneling by heavy holes can be ignored. Kane assumed that equal hole and electron mass, but in all the materials under consideration, the light hole mass is slightly heavier than the electron mass. The effective mass will be approximated as $m^* = 2((m_e^*)^{-1} + (m_{lh}^*)^{-1})^{-1}$.

Another feature of the InGaP/AlGaAs heterojunction is that the band offset reduces the tunneling width, and so increases the tunneling current. The simplified junction has a tunneling width that is independent of energy, but a more accurate result can be obtained by finding the band structure using Poisson's equation [18]:

$$\frac{d}{dz} \left(\epsilon(z) \frac{dE}{dz} \right) = q[p(z) - n(z) + N_d^+(z) - N_a^+(z)] \quad 7.4$$

Since the permittivity depends upon the particular material, the positional dependence of ϵ must be included. Also, the hole and electron density cannot use the Boltzmann approximation in the neutral regions, the half-order Fermi-Dirac integral must be used in these cases [19].

$$n = N_c \frac{2}{\sqrt{\pi}} F_{1/2} \left(\frac{E_f - E_c}{kT} \right), \quad p = N_v \frac{2}{\sqrt{\pi}} F_{1/2} \left(\frac{E_v - E_f}{kT} \right) \quad 7.5$$

For a junction with the n-type material at $z < 0$ and p-type material at $z > 0$, the boundary conditions for the valence band will be $E(-\infty) = 0, E(\infty) = q(V_{bi} - V_a)$ and $\mathcal{E}(-\infty) = \mathcal{E}(\infty) = 0$ with V_{bi} and V_a being the built in and applied voltage, respectively. There are also internal boundary conditions at each heterojunction interface with $E(E^+) - E(E^-) = \Delta E_v$ and $\mathcal{E}(E^+)/\mathcal{E}(E^-) = \epsilon(E^+)/\epsilon(E^-)$. Once the conduction and valence band energies are found, the tunneling width can be calculated as a function of energy. Equation 7.1 can then be used to find the tunneling current either by using an average value for W or by including the terms containing B and \bar{E} in the integral.

For a InGaP doping of $1.6 \times 10^{19} \text{ cm}^{-3}$ and an AlGaAs doping of $7.0 \times 10^{19} \text{ cm}^{-3}$, equation 7.1 gives a peak tunneling current of 0.82 A/cm^2 , much lower than the 18 A/cm^2 measured from an actual device.

Since the Kane model does not adequately account for the behavior of this TJ, other models must be considered. The Kane model is also inadequate for more complex structures like the n-InGaP/n-GaAs/p-AlGaAs TJ since tunneling may occur through both the InGaP and the GaAs.

7.4.2. Transfer matrix model

The Esaki equation for tunneling uses the tunneling probability as a function of energy, $t(E)$ to find the current [14].

$$J = \frac{q}{2\pi\hbar} \int_{E_1}^{E_2} [n_{2D}(E_f - E) - n_{2D}(E_f - qV_a - F)] t(E) dE \quad 7.6$$

n_{2D} is the carrier density in a two dimensional electron (or hole) gas:

$$n_{2D} = \frac{m^*kT}{\pi\hbar^2} \ln(e^{E/kT} + 1) \quad 7.7$$

Since the band structure is already known from equation 7.4, $t(E)$ can be found using the transfer matrix method. At any particular energy, E , between E_1 and E_2 , an electron can tunnel from the conduction band to the valence band, $t(E)$ is the probability that the tunneling process will occur. Over this interval, the barrier is split into a number of equally spaced rectangular barriers. The transmission through the i^{th} barrier depends upon the wavenumber in that layer, $k_i = \sqrt{[2qm^*(E_c - E)]/\hbar^2}$, and the previous layer [20]:

$$M_i = \begin{pmatrix} e^{-k_i d_i} & 0 \\ 0 & e^{k_i d_i} \end{pmatrix} \begin{pmatrix} 1 + k_i/k_{i-1} & 1 - k_i/k_{i-1} \\ 1 - k_i/k_{i-1} & 1 + k_i/k_{i-1} \end{pmatrix} \quad 7.8$$

d_i is the thickness of the layer. The complete transmission matrix is found from the product $M = \prod_i^N M_i$ and for tunneling in the positive direction the transmission probability can be found from the M_{22} matrix element as $T=1/M_{22}$.

7.4.2.1. Direct tunneling

The simplest case is where the junction contains no trap states and tunneling directly from one band to another. This method is applicable to both the InGaP/AlGaAs and InGaP/GaAs/AlGaAs structures. Since there is only one source of tunneling current, the tunneling probability is related to the transmission probability by $t_{\text{dir}}(E)=|T_{\text{dir}}(E)|^2$.

Table 7.2: Comparison between measured and calculated J_{pk} for various GaAs thicknesses using a direct tunneling model.

GaAs thickness (Å)	Measured J_{pk} (A/cm ²)	Calculated J_{pk} (A/cm ²)
0	18	0.0079
15	50	1.0
30	1020	2.3
45	701	5.5

Table 7.2 shows the comparison of J_{pk} of actual devices and J_{pk} as calculated by direct tunneling with $N_{d,InGaP}=1.6 \times 10^{19} \text{ cm}^{-3}$, $N_{d,GaAs}=2.2 \times 10^{19} \text{ cm}^{-3}$ and $N_{a,AlGaAs}=7.0 \times 10^{19} \text{ cm}^{-3}$. The devices show the general trend of increasing current with increasing GaAs thickness which can be attributed to the lower effective mass in the GaAs. As with the Kane model, the measured current is much higher than the calculated current. Direct tunneling also does not explain the large jump in J_{pk} for the 30 and 45 Å GaAs layers.

7.4.2.2. Resonant trap assisted tunneling

The case of trap assisted tunneling is somewhat more complicated. The trap can be modeled as a quantum well that has a depth and width that is characteristic of the particular trap. Figure 6 shows several parameters of the trap that define its behavior. It is assumed that the trap occurs at a particular depth relative to either the conduction or valence band and will have the same width at all locations. The other two parameters are trap density (N_t) and capture cross section (σ). In order for tunneling through a defect to occur there must be an available trap nearby. The capture cross section is the area at the junction over which TAT can occur for a single trap, and the number of available traps in an area is given by $N_t^{2/3}$. This means for TAT, the tunneling probability is $t_{TAT}(E)=\sigma N_t^{2/3} T_{TAT}(E)$.

The characteristics of deep levels are not as well documented for AlGaAs and InGaP as for GaAs, so only traps in the GaAs of the InGaP/GaAs/AlGaAs structure will be modeled. There are two types of defects that will be taken into consideration. The first is the oxygen deep level in GaAs that was considered by Jandieri et. al [21]. This defect is an electron trap that has been reported to be 0.75 eV below the conduction band and can have concentrations as high as $1 \times 10^{15} \text{ cm}^{-3}$. For the second defect, it can be speculated that the excess Te in GaAs may result in a defect state. Several defects have been found in GaAs with high Te doping, such as Ga_7Te_3 precipitates [22] and Te_{As} donors [23], the latter of which has been found to have densities as high as $6 \times 10^{18} \text{ cm}^{-3}$. In order to determine the effect of a very large defect density, this Te based defect will be considered to have a concentration of $1 \times 10^{19} \text{ cm}^{-3}$ at several different levels relative to the conduction band in order to find the maximum possible current that can be attributed to resonant TAT. The traps will be considered to be a single monolayer

in thickness (2.8 \AA) and will have the same mass as electrons in GaAs. In both cases the oxygen trap capture cross section of $7 \times 10^{-16} \text{ cm}^2$ will be used [24].

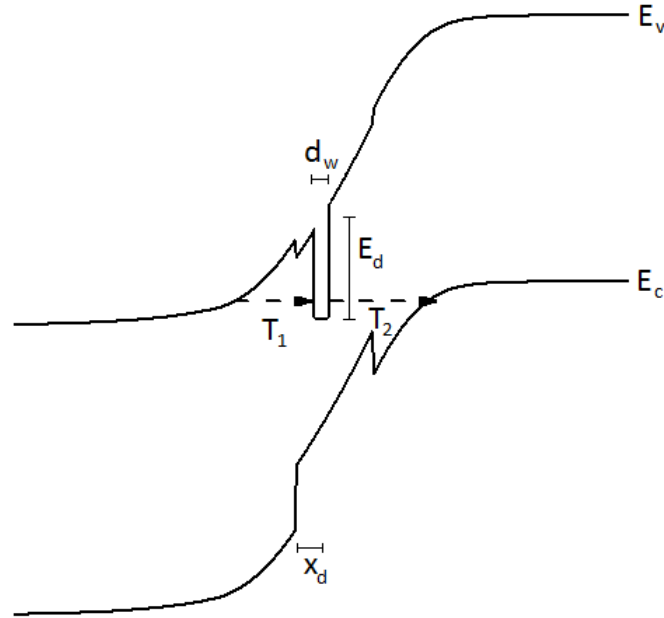


Figure 7.5: InGaP/GaAs/InGaP with the quantum well model for a single trap state

Resonant TAT behaves in the same manner as a resonant tunneling diode except that there are several possible locations where the quantum well could be present since the traps can be present anywhere within the depletion region of the diode. Regions of high transmission due to resonance occur at particular combinations of energies and trap positions. Figure 5 shows the band structure for one particular trap location, but traps can be distributed throughout the depletion region. The tunneling process can be broken down into three regions: from the conduction band to the trap state, from the trap state to the valence band and the trap itself. If the transmission and reflection probabilities through the two sections are given as T_1 , T_2 , R_1 and R_2 and the well thickness as d_w and well wavenumber as k_w then the total transmission probability is:

$$T_{TAT}(E, x) = \frac{T_1 T_2}{1 - R_1 R_2 e^{2ik_w d_w}} \quad 7.9$$

T_{TAT} will depend both upon energy and the position of the trap in the GaAs layer. If it is assumed that the traps are evenly distributed throughout the GaAs, then T_{TAT} at any particular energy is the average of T_{TAT} for all possible trap locations.

Figure 6 shows the J-V response for the same tunnel diode as section 7.4.2.1. The direct tunneling current is shown along with the expected contributions from a trap state with a concentration of 10^{15}

cm^{-3} and 10^{19} cm^{-3} and a trap depth of 0.5 eV. Slightly higher current densities were obtained as the trap depth was increased to 1.0 eV, but only about twice the J_{pk} as the 0.5 eV state. Even with the very high trap density, the TAT contribution is much lower than the direct tunneling.

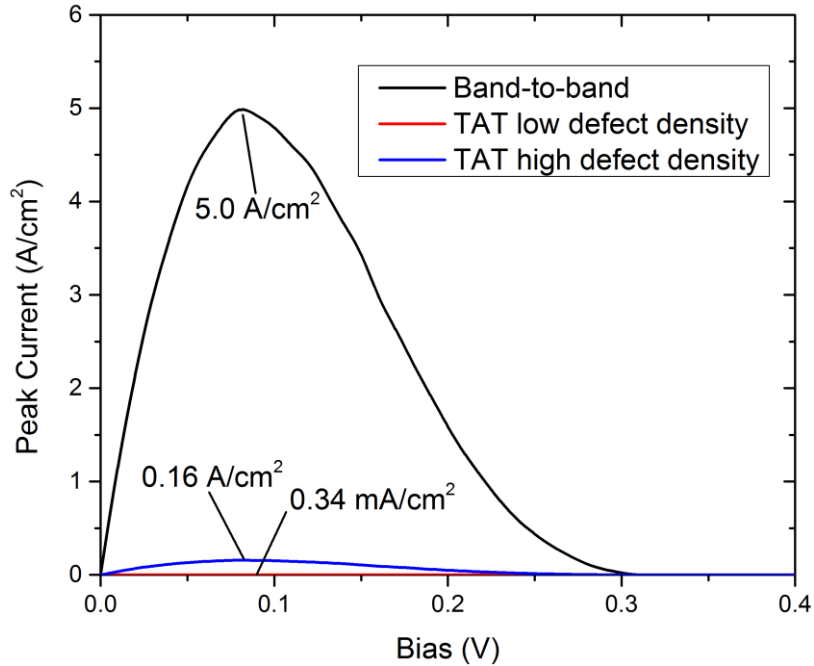


Figure 7.6: Modeled J-V response for a TJ with direct tunneling and TAT for traps with densities of 10^{15} cm^{-3} and 10^{19} cm^{-3}

7.4.3. Thermal diffusion of dopants and diffusion barriers

Since the Ge/GaAs/InGaP multijunction cell is grown monolithically, the top tunnel junction will be subject to the thermal conditions of the InGaP subcell growth. InGaP is typically grown at 650 °C or higher in order to obtain long recombination lifetime in the top cell. The tunnel junction should be able to maintain a high J_{pk} after this growth.

Modeling the dopant diffusion requires the temperature dependent diffusion coefficient (D) of both tellurium and carbon in GaAs, InGaP and AlGaAs to be known. The diffusion coefficient of both C [8] and Te [25] in GaAs are well documented, as well as that of C in AlGaAs which is lower than in GaAs [8]. For Te in AlGaAs, which has not been reported, it is assumed that the ratio between D for tellurium in GaAs and AlGaAs is that same as the ratio between the same two materials in carbon. For InGaP there are no reports of the measurement of D for either C or Te. Zn in InGaP diffuses about 6 times as fast as in GaAs [26], so this will be used as the scaling factor for both Te and C.

Dopant diffusion can occur either between the n- and p-type layers at the junction or away from highly doped layers into lower doped cladding layers. Diffusion at the interface reduces the effective

doping due to both the reduction in the concentration of dopant species and compensation from the dopants in from the adjacent material. This is particularly an issue on the donor side since the AlGaAs doping is much larger than the either the n-type GaAs or InGaP. Outdiffusion is an issue when the highly doped layer is thin enough such that the doping concentration is reduced in the depletion region of the junction. This is more serious issue for tunnel junctions containing GaAs since it is grown as thin as possible to avoid losses due to absorption. Outdiffusion can be avoided in the InGaP/GaAs/AlGaAs structure by growing the InGaP sufficiently thick. The spike doping model, which will be discussed in the next section, can be effected by outdiffusion.

Once the diffusion coefficients and doping profile ($N(z,t)$) is known, the diffused doping profile can be found by solving the one dimensional diffusion equation:

$$\frac{\partial N(z,t)}{\partial t} = \frac{\partial}{\partial z} \left[D(z) \frac{\partial N(z,t)}{\partial z} \right] \quad 7.10$$

Note that diffusion coefficient is between the two differential terms, this is necessary since the diffusion coefficient differs between materials and so will be a function of position in the tunnel junction.

Interdiffusion between the n and p-type materials can occur in both the InGaP/AlGaAs structure and the InGaP/GaAs/AlGaAs structure. The doping was assumed to be $2.4 \times 10^{19} \text{ cm}^{-3}$ in the InGaP and $1.2 \times 10^{20} \text{ cm}^{-3}$ in the AlGaAs. The doping in each layer was taken to be higher than the experimental doping in order to ensure that J_{pk} was larger than 1 A/cm^2 . This is necessary since for this implementation of the Kane model very weak tunnel diodes did not give the expected tunneling characteristic. For carbon in $\text{Al}_x\text{Ga}_{1-x}\text{As}$, it has been found that the diffusion coefficient decreases as the aluminum fraction increases, especially for $x > 0.6$. A potential solution is to add a thin AlAs layer at the junction interface. Since it can be difficult to dope AlAs as high as AlGaAs, it is assumed that the doping in this layer is lower, at 10^{18} cm^{-3} . It is expected that the unannealed junction have a lower J_{pk} due to the low doping in this layer, but due to the reduction in diffusion it is possible that annealed devices will show improved performance with the diffusion barrier.

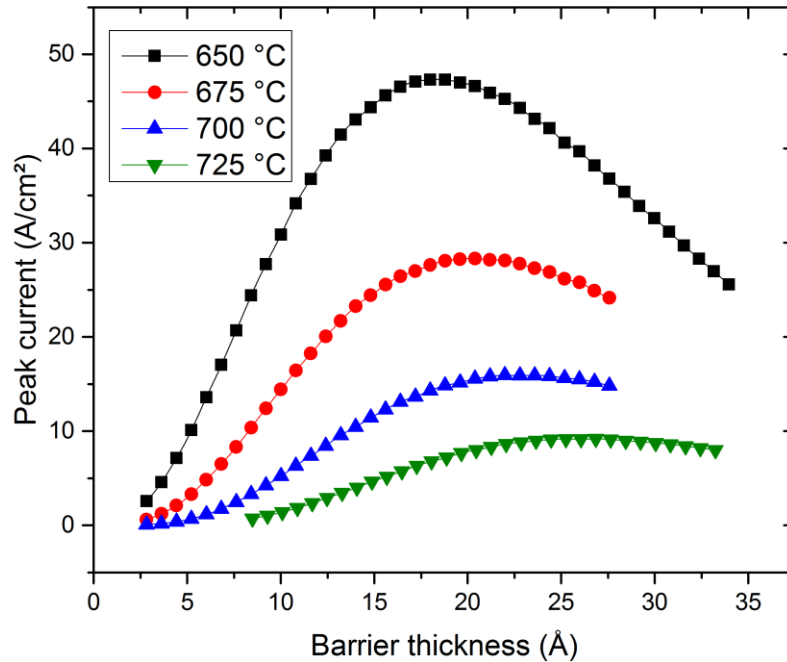


Figure 7.7: Peak current for an annealed InGaP/AlAs/AlGaAs TJ as a function of the AlAs diffusion barrier thickness

The effect of annealing for 30 minutes at several temperatures on the J_{pk} as a function of AlAs thickness is shown in figure 7 for an InGaP/AlAs/AlGaAs TJ. The Kane model was used to find J_{pk} . For each annealing temperature there is an ideal AlAs thickness. This arises since a thin AlAs layer does not block the diffusion of dopants adequately while a thick AlAs reduces J_{pk} since it is not doped to a very high level. Higher annealing temperatures result in lower peak current densities and have higher ideal AlAs thicknesses since diffusion is increased. The ideal AlAs thickness ranges from 17 and 26 Å for anneal temperatures from 650 °C to 725 °C.

Diffusion barriers have also been used to clad the highly doped semiconductors in order to limit outdiffusion. This is particularly important when GaAs is used since its thickness must be minimized to avoid absorption losses. Nevertheless, outdiffusion barriers are of some interest for InGaP/AlGaAs TJ as it will be seen in the next section. J_{pk} was calculated for various thicknesses of the InGaP layer. The cladding material was taken to be InGaP but with a lower doping level of 10^{18} cm^{-3} . Figure 8 shows the results for several annealing temperatures. The sudden drop for InGaP less than 100 Å is due to the highly doped n-type material being thinner than the depletion width. When this occurs, the depletion width includes the low doped region and J_{pk} falls rapidly. Outdiffusion is an issue only for the higher growth temperatures. For a tunnel diode exposed to a 650 °C, 30 minute growth step, the InGaP can be made as thin as 110 Å without any reduction in J_{pk} .

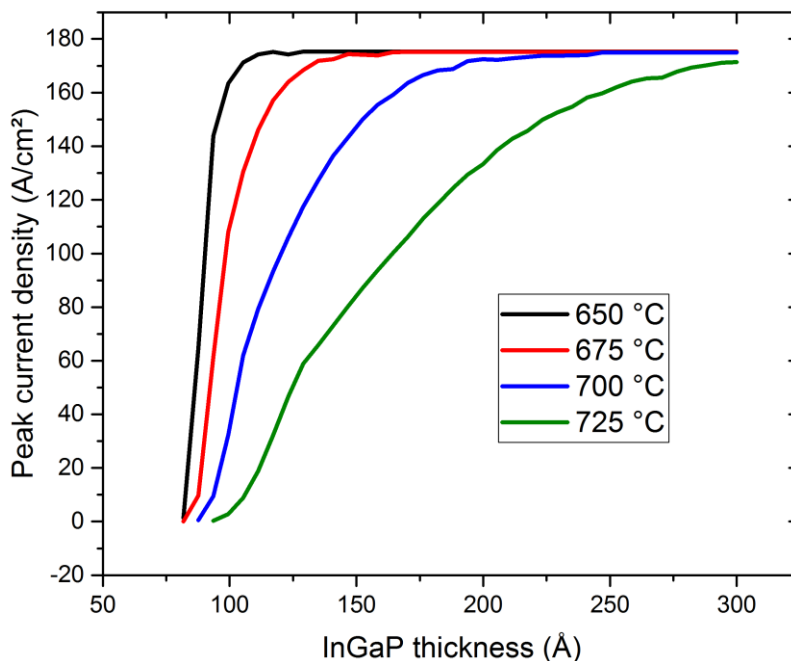


Figure 7.8: Peak current density as a function of InGaP thickness for annealed InGaP/AlGaAs tunnel junctions

7.4.4. Spike doping at InGaP/GaAs interface

Neither the direct tunneling nor the resonant trap assisted tunneling models were able to explain the J_{pk} that were consistent with the experimental results for the InGaP/GaAs/AlGaAs TJ structures. In both models the doping in each layer was chosen based upon the Hall effect measurements of layers that were grown between 0.3 and 0.6 μm thick. However, the behavior of the tunnel junction depends upon the doping in a region that is much thinner, about 10 nm thick near the heterointerfaces and includes transitions from InGaP to GaAs and GaAs to AlGaAs. There is the possibility that the doping characteristics in this region are not the same as in the thicker layers used in calibration sample. There are several mechanisms that could account for a higher doping at the InGaP/GaAs interface: 1. tellurium can carryover from the InGaP into the GaAs where Te has a higher solubility, 2. it was shown that in the InGaAs/GaAsP superlattice, MOCVD growth does not result in abrupt interfaces, so there is likely carryover of indium and phosphorus into the GaAs layer of the TJ. This section will discuss the first possibility while the next section will discuss the second possibility.

Tellurium in particular is known to be retained on the surface at a higher concentration than in the crystal lattice; this behavior has been associated with Te carryover effect [27]. If the tellurium is incorporated in a larger amount at the InGaP/GaAs interface than in the lattice of either GaAs or InGaP, a doping spike could form in a thin region at the interface. This would not be apparent in Hall effect measurements since it is used to determine the average doping in a thick layer.

The behavior of this doping spike will be investigated to determine if it can account for three features of the InGaP/GaAs/AlGaAs TJ: the strong dependence of J_{pk} on the thickness of the GaAs, the sharp decrease in J_{pk} when the structure is annealed at 650 °C or higher and the inability to model the experimental J_{pk} by either direct tunneling or TAT mechanisms. The spike will be considered to be a layer 10-30 Å thick in either the InGaP or GaAs with a doping that ranges from the bulk doping level ($1.6 \times 10^{19} \text{ cm}^{-3}$ in InGaP and $2.2 \times 10^{19} \text{ cm}^{-3}$ in GaAs) to $6.0 \times 10^{19} \text{ cm}^{-3}$. The GaAs layer thickness will be considered to be 0 to 45 Å thick in order to model previously grown InGaP/GaAs/AlGaAs structures.

The J-V response is calculated using the same method as section 7.4.2.1. with the addition of the doping spike when finding the band structure. The Kane model is not appropriate for this structure since it cannot account for the complexity of the n-type doping profile. As it will be shown later, the valence band discontinuity between the GaAs and AlGaAs will be of particular importance.

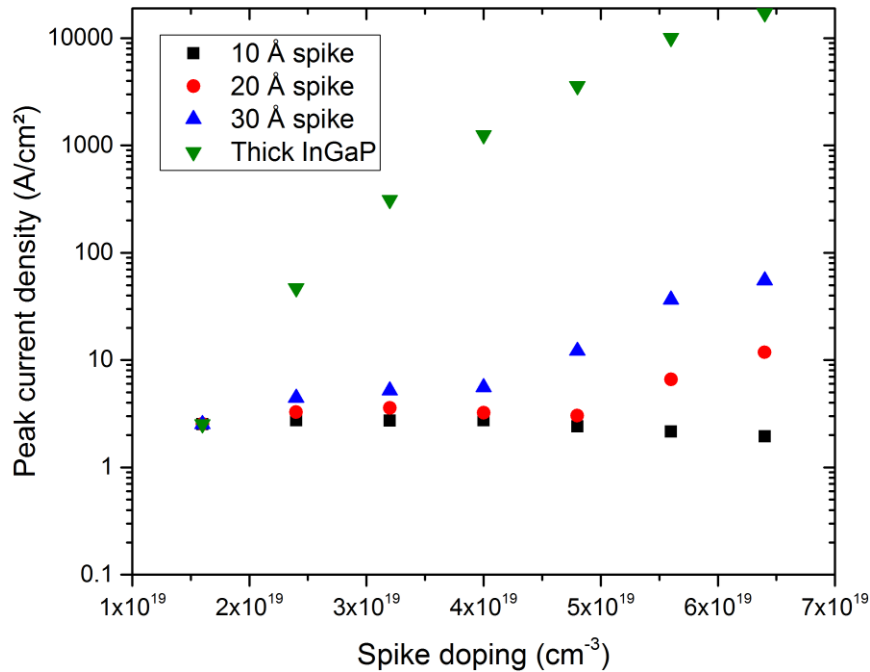


Figure 7.9: Peak current density versus spike doping for various thicknesses of the spike layer in InGaP

Figure 9 shows the peak tunneling current as a function of the spike doping for a 30 Å GaAs thickness where the thickness of the spiked region is considered to be 10, 20 and 30 Å thick. Similar results are shown for a thick, highly doped InGaP layer, although it cannot exist in actual devices since tellurium doped InGaP has not been reported with such large effective carrier concentrations. For each spike thickness, J_{pk} is fairly constant at low doping levels. For the 20 Å and 30 Å thick

spikes, J_{pk} does not increase until the spike doping reaches a particular threshold, $4.0 \times 10^{19} \text{ cm}^{-3}$ for the 30 Å spike and $5.0 \times 10^{19} \text{ cm}^{-3}$ for the 30 Å spike. In all cases J_{pk} does not exceed 100 A/cm^2 .

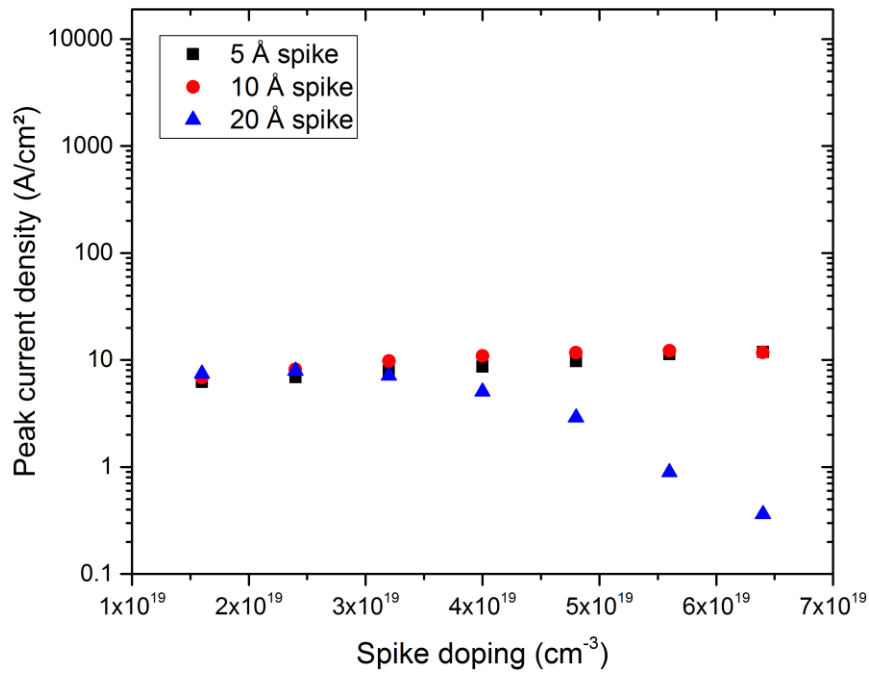


Figure 7.10: Peak current density versus spike doping for various thicknesses of spike doping in GaAs

The spike can also be considered to be in the GaAs layer instead of the InGaP. In this case the spike is taken to be 5 Å, 10 Å and 20 Å, as shown in figure 10. The presence of the spike in the GaAs is clearly has less of an impact on J_{pk} than when it was present in the InGaP. For the thickest spike layer, 20 Å, there is even a decrease in J_{pk} as the spike doping decreases. This result, along with the results of the doping spike in the InGaP suggests that the high doping region may give a larger J_{pk} when it is farther away from the pn junction.

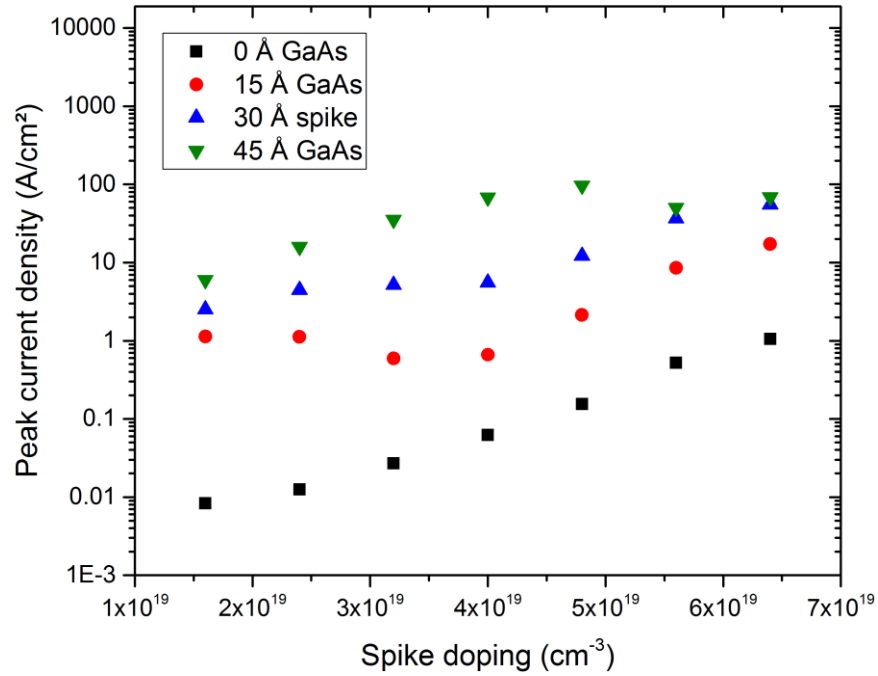


Figure 7.11: Peak current density versus spike doping for various GaAs thicknesses

To test this idea, Figure 11 shows the effect of GaAs thickness with a 30 Å spike in the InGaP for GaAs layers with a thickness of 0, 15, 30 and 45 Å. The thicker GaAs layers give a higher doping in the, which is consistent with previous results that show that the lower effective mass of GaAs helps increase the tunneling probability when the GaAs makes up a larger portion of the depletion region. There are some unusual features of fig. 11, most notably for the 45 Å GaAs layer, where J_{pk} slightly decreases as the spike doping increases from $4.8 \times 10^{19} \text{ cm}^{-3}$ to $5.6 \times 10^{19} \text{ cm}^{-3}$.

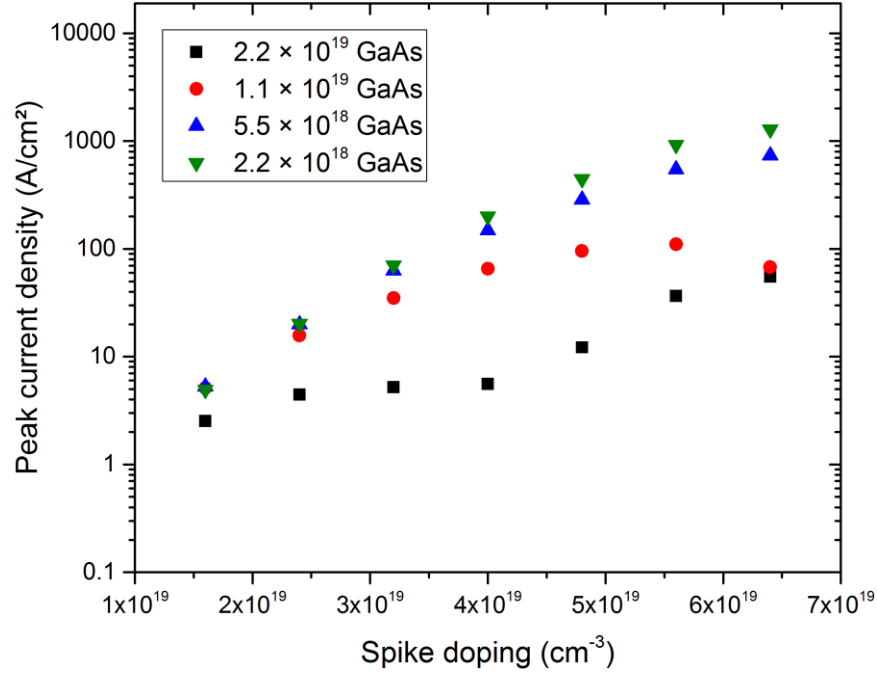


Figure 7.12: Peak current density versus spike doping for various doping levels in GaAs

In section 7.1 it was noted that the DETe flow required to achieve the highest doping was much higher for InGaP than it was for GaAs. Since the GaAs is at most 45 Å, the tellurium carryover is significant in the GaAs. This was confirmed by the high J_{pk} obtained in samples that had the DETe flow cut off at the beginning of the GaAs growth or even a few seconds earlier during the growth of the InGaP. It is possible that the doping in the GaAs is less than the $2.2 \times 10^{19} \text{ cm}^{-3}$ that was measured from calibration samples. Therefore, it is reasonable to consider the effect of GaAs doping on J_{pk} , which is shown for a 30 Å GaAs layer and a 30 Å InGaP spike in figure 12. There is an inverse relationship between the peak tunneling current and the GaAs doping level. With the effective doping in the GaAs below $1 \times 10^{19} \text{ cm}^{-3}$ and a spike doping in InGaP above $5 \times 10^{19} \text{ cm}^{-3}$, the magnitude of J_{pk} begins to approach the values found from experimental results. Figure 13 shows the J_{pk} for as a function of the GaAs doping for for a 30 Å $4.8 \times 10^{19} \text{ cm}^{-3}$ doped spike layer. The large increase in J_{pk} at low doping levels in the GaAs only occurs for the 30 and 45 Å GaAs layer but not for the 15 Å GaAs. This large jump in J_{pk} for GaAs thicker than 15 Å is consistent with the experimental results for actual devices.

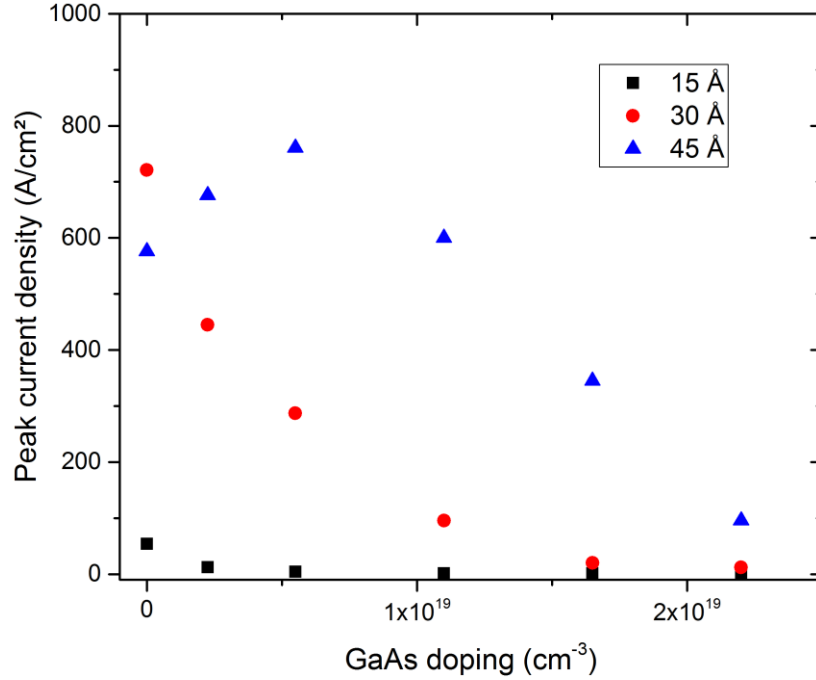


Figure 7.13: Peak current density versus GaAs doping for various GaAs thicknesses and a $4.8 \times 10^{19} \text{ cm}^{-3}$ InGaP doping spike.

The reason low doping the GaAs give a large J_{pk} can be seen in figure 14, which shows the conduction and valence band of the spike doped junction at zero bias with $N_{d,GaAs}$ of $1 \times 10^{18} \text{ cm}^{-3}$ and $2.2 \times 10^{19} \text{ cm}^{-3}$. When the GaAs doping is low more the band bending occurs in the highly doped InGaP region. As a result the tunneling width for electrons is much shorter due to the presence of the quantum well formed by the band offset between the GaAs and AlGaAs. When the GaAs doping is higher, this well is at a lower energy and does not have any impact on direct tunneling.

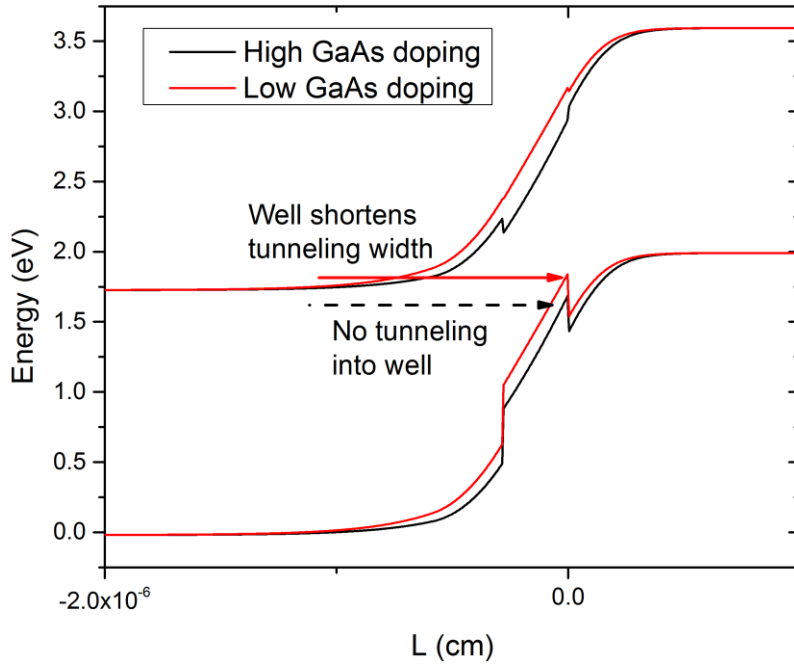


Figure 7.14: Band profile for InGaP/GaAs/AlGaAs TJ with low ($2.2 \times 10^{18} \text{ cm}^{-3}$) and high ($2.2 \times 10^{19} \text{ cm}^{-3}$) doping in GaAs

The effect of dopant diffusion on the spike doping structure is shown in figure 15, which gives the donor profile for before and after annealing at $650 \text{ }^\circ\text{C}$ for 30 minutes. There are two features of the annealed profile which can cause problems for the spike doping structure in particular: 1) Reduction of the peak doping in the spike from $4.8 \times 10^{19} \text{ cm}^{-3}$ down to $3.5 \times 10^{19} \text{ cm}^{-3}$. Figure 13 shows that this factor alone will cause J_{pk} to drop to a third of its value before annealing. 2) Diffusion of the tellurium into the GaAs which it has been shown should have a low effective doping. The effect of annealing on a structure with a 30 \AA $4.8 \times 10^{19} \text{ cm}^{-3}$ spike layer and a thick InGaP with the same doping is shown in figure 16. There is a much larger reduction in J_{pk} with annealing for the spike doping than for the bulk doping. This is analogous to GaAs/GaAs and GaAs/AlGaAs TJ structures, where the GaAs is grown thin in order to reduce losses from light absorption. In those structures outdiffusion limits how thin the GaAs can be grown, but the proposed spike doping structure is an unexpected result of the MOCVD growth process. Nevertheless, there may be a similar solution to the outdiffusion problem that has been used for the GaAs containing tunnel junctions: the use of barrier materials such as AlGaAs which have been shown to reduce the diffusion of many dopants. More work will be needed to see if these materials can be incorporated without interfering with the growth of the highly doped layers at the junction interface.

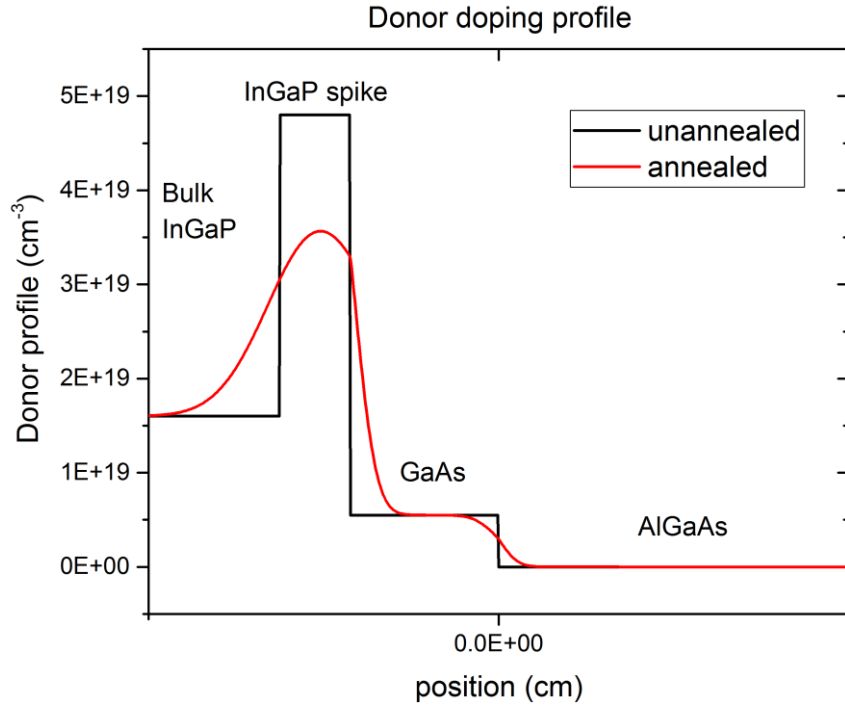


Figure 7.15: Donor doping profile before and after annealing at 650 °C for 30 minutes

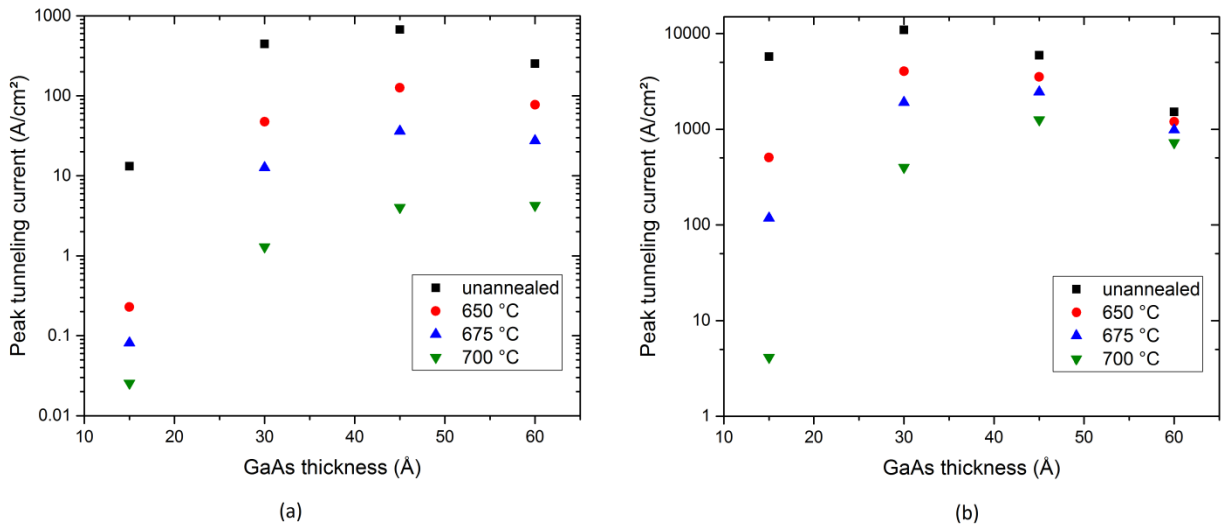


Figure 7.16: Peak tunneling current versus GaAs for annealed and unannealed TJ with (a) 30 \AA doping spike and (b) thick InGaP layers

7.4.5. Indium carryover from InGaP into GaAs

The spike doping model was able to account for the high J_{pk} observed in InGaP/GaAs/AlGaAs tunnel junctions. The main weakness of this model is that there is no physical evidence for doping level s

above $5 \times 10^{19} \text{ cm}^{-3}$ in InGaP that are required by the model to give values of $J_{pk} > 1000 \text{ A/cm}^2$. Delta doping of InGaP with Te has been found to give high sheet concentrations [28], but this requires a growth pause while DETe and phosphine flow for several seconds. This does not occur in any of the tunnel junction structures in this work; the GaAs is grown immediately after the InGaP by shutting off the flow of TMIIn and TBP and turning on the flow of TBAs.

EDS-STEM analysis of the $\text{In}_x\text{Ga}_{1-x}\text{As}/\text{GaAs}_{1-y}\text{P}_y$ superlattice found that there was a carryover of phosphorus from the GaAsP into subsequent layers [29]. The same analysis also showed a carryover of indium from the InGaAs. For these particular structures the phosphorus carryover had a larger effect on the PL emission peak since the fraction of phosphorus in the $\text{GaAs}_{1-y}\text{P}_y$ ($y=0.8$) was much higher than the fraction of indium in the InGaAs ($x=0.2$). It is likely that a similar effect is present in the InGaP/GaAs/AlGaAs TJ structures, where there is a significant carryover of both indium and phosphorus into the GaAs. The indium carryover is more likely to be significant in the TJ structure than in the superlattice as the fraction of indium in the InGaP is much higher than the InGaAs of the superlattice.

The band offset between GaAs and both the InGaP and AlGaAs is much smaller in the conduction band than in the valence band. As a result there is no well in the conduction band within the energy range for tunneling as there is in the valence band. If the GaAs were to be replaced with a lower band gap material, especially one with a larger conduction band offset between the InGaP and AlGaAs, then this conduction band well could reduce the tunneling width and give much larger peak tunneling currents. Also, since the n-type doping is lower than the p-type doping, the conduction band well has the potential to reduce the tunneling distance more than the valence band well. The majority of the band offset between GaAs and InGaAs is in the conduction band. Indium carryover is a potential source of a conduction band well.

Within the depletion region the conduction band of the GaAs has the lowest potential immediately adjacent to the InGaP, so an InGaAs layer only a few angstroms thick would be sufficient to reduce the tunneling width. To simplify the model, the indium carryover is treated as an InGaAs layer of constant composition. Since this layer is produced by the carryover of indium from the InGaP, it is unlikely that the composition of the indium relative to gallium will exceed that of lattice matched InGaP. As before, the InGaP will be considered to be doped $1.6 \times 10^{19} \text{ cm}^{-3}$ n-type and the AlGaAs doped $7.0 \times 10^{19} \text{ cm}^{-3}$. The behavior of tellurium doping in InGaAs is not known, so this layer will be considered to have the same doping as the GaAs. The direct tunneling model will be used to find J_{ok} .

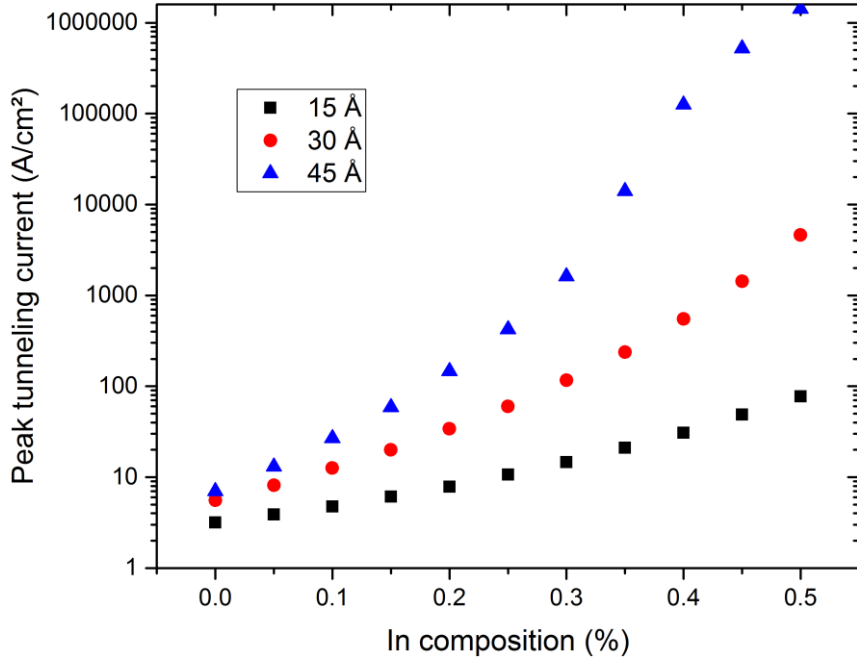


Figure 7.17: Peak tunneling current density versus indium composition for an InGaP/InGaAs/AlGaAs TJ for a 15, 30, and 45 Å InGaAs thickness.

Figure 17 shows the peak tunneling current for an InGaP/InGaAs/AlGaAs structure as a function of the indium fraction in InGaAs layers that are 15, 30 and 45 Å thick. In each case the InGaAs layer is the only material between the InGaP and AlGaAs and is doped n-type to $1.0 \times 10^{19} \text{ cm}^{-3}$. J_{pk} tends to increase as the InGaAs thickness increases which is due to two factors: 1) the effective mass of both electrons and holes is lower in InGaAs than in InGaP, so a thicker InGaAs region will increase the tunneling probability and 2) a thicker InGaAs layer will result in the InGaP/InGaAs interface being at a lower potential, increasing the effective depth of the conduction band well. While it is unlikely that the indium carryover is as extreme as represented here, it does indicate the limits of a particular GaAs thickness. Since the 15 Å layer has a maximum J_{pk} of 77 A/cm^2 even for an $\text{In}_{0.5}\text{Ga}_{0.5}\text{As}$ well, it is unlikely that this structure will be capable of producing the high J_{pk} required for tunnel junctions for high concentration solar cells. Both the 30 Å and 45 Å layers can give $J_{pk} > 1000 \text{ A/cm}^2$. This is consistent with the experimental results that show a large jump in the J_{pk} when the GaAs thickness goes from 15 Å to 30 Å.

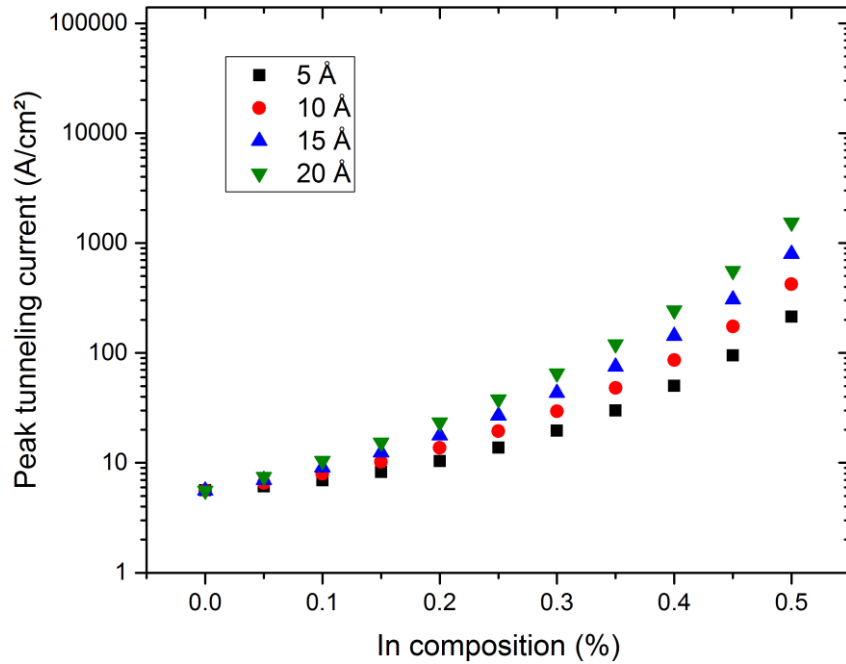


Figure 7.18: Peak tunneling current versus indium composition for an InGaP/GaAs/AlGaAs TJ with 30 Å GaAs. The indium carryover is modeled as a constant composition region at the InGaP/GaAs interface.

A more realistic scenario is that the InGaAs exists in a thin portion of the GaAs layer immediately after the InGaP. Figures 18 and 19 show the modeled J_{pk} as a function of InGaAs composition for a 5, 10, 15 and 20 Å InGaAs well within a 30 Å and 45 Å GaAs layer. The 15 Å GaAs is not included as it was shown that this thickness is insufficient to produce the necessary peak tunneling current densities. Unsurprisingly, J_{pk} is larger for the thicker InGaAs layers.

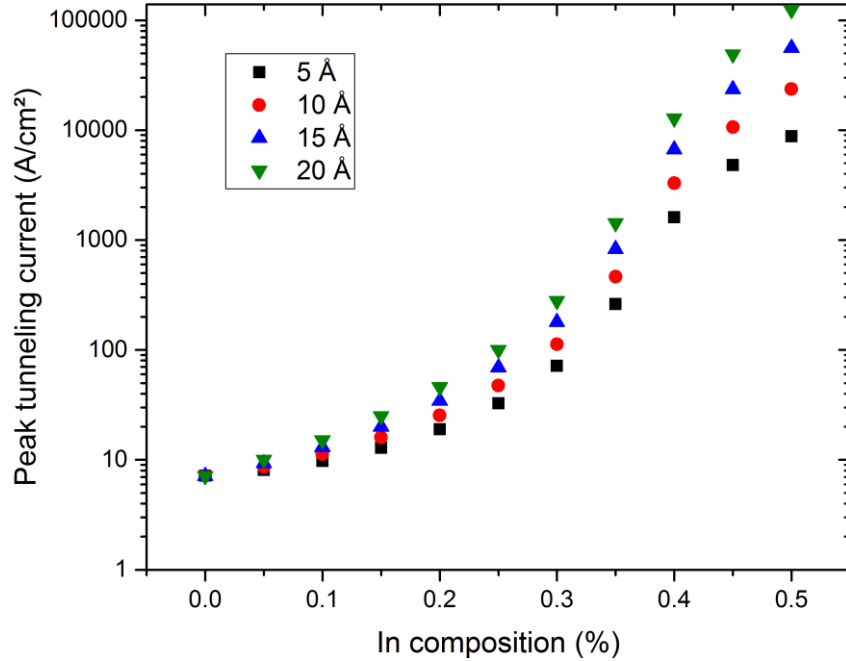


Figure 7.19: Peak tunneling current versus indium composition for an InGaP/GaAs/AlGaAs TJ with 45 Å GaAs. The indium carryover is modeled as a constant composition region at the InGaP/GaAs interface.

Another parameter of interest is the doping in the InGaAs/GaAs region. The spike doping model had the surprising result where J_{pk} was higher for lower doping in the GaAs. This was due to the valence band well reducing the tunneling width to a greater extent when the GaAs doping is lower. There may be a similar phenomenon for the conduction band wells. To test this, the InGaAs well was considered to be composed of 10 Å of $In_{0.4}Ga_{0.6}As$ for both a 30 Å and a 45 Å well. J_{pk} was found for a GaAs doping ranging from $2 \times 10^{18} \text{ cm}^{-3}$ to $3 \times 10^{19} \text{ cm}^{-3}$. It can be seen in figure 20 that there is a maximum J_{pk} for the 45 Å at $1.8 \times 10^{19} \text{ cm}^{-3}$ while J_{pk} for the 30 Å increases throughout the doping range. For doping densities above $3 \times 10^{19} \text{ cm}^{-3}$ the results for the two different GaAs thicknesses begin to approach one another. This indicates that there may be a high doping density in the GaAs for the actual devices that results in a similar J_{pk} .

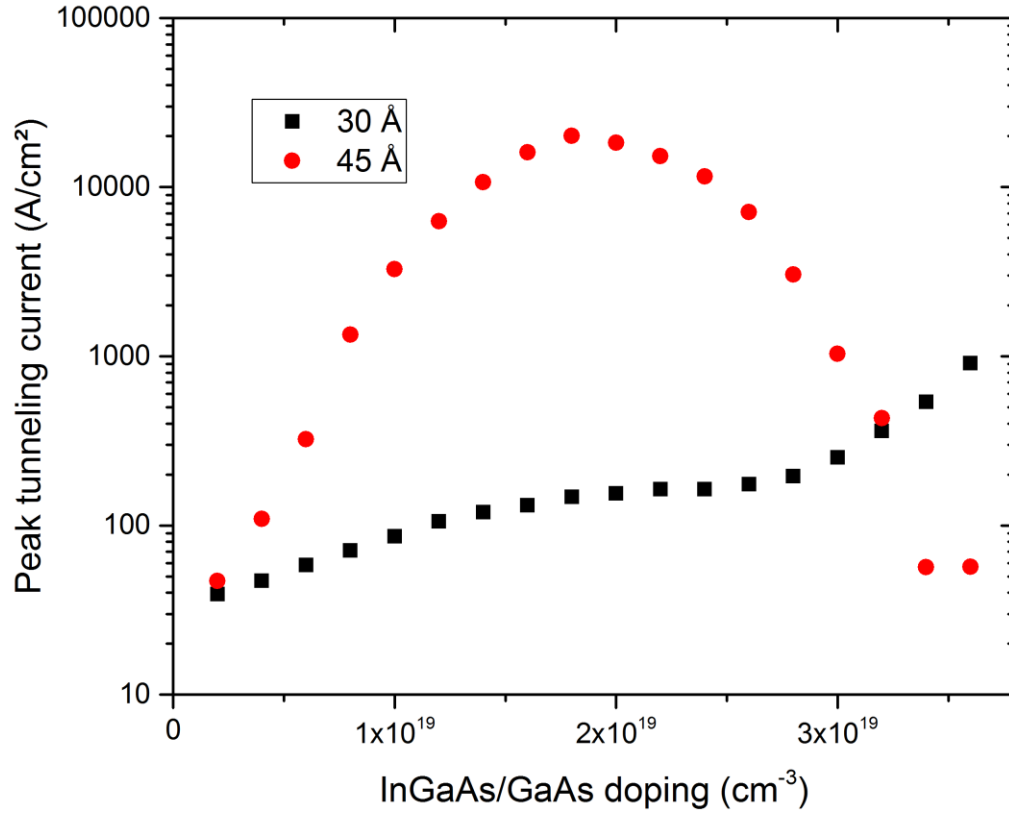


Figure 7.20: Peak tunneling current density versus doping density in the GaAs of a InGaP/GaAs/AlGaAs TJ with a 10 Å $\text{In}_{0.4}\text{Ga}_{0.6}\text{As}$ layer representing the indium carryover.

One drawback of the indium carryover is that it is expected to increase the absorption due to the lower bandgap of the InGaAs. For instance, the absorption coefficient of $\text{In}_{0.25}\text{Ga}_{0.75}\text{As}$ is about twice that of GaAs at 700 nm. However since the indium is expected to only be in the first few monolayers of the GaAs, this additional absorption is likely to be minor source of efficiency loss in the solar cell.

REFERENCES

Chapter 1

1. International Energy Agency, *Key World Energy Statistics*, <https://www.iea.org/publications/freepublications/publication/key-world-energy-statistics-2014.html>, 2014
2. V. Smil, *General Energetics: Energy in the Biosphere and Civilization*, Wiley, 1991.
3. World Energy Council, *World Energy Resources: 2013 Survey*, <http://www.worldenergy.org/publications/2013/world-energy-resources-2013-survey/>, October 2013.
4. A. Ignaciuk, F. Vöhringer, A. Ruijs and E.C. van Ierland, “Competition between biomass and food production in the presence of energy policies: a partial equilibrium analysis”, *Energy Policy*, 34:1127, 2004.
5. U. S. Energy Information Administration, “Levelized Cost and Levelized Avoided Cost of New Generation Resources in the Annual Energy Outlook 2014”, http://www.eia.gov/forecasts/aeo/electricity_generation.cfm, May 2014
6. S. Jacobsson and A. Johnson, “The diffusion of renewable energy technology: an analytical framework and key issues for research”, *Energy Policy*, 28:625, 2000.
7. B. Schlamadinger and G. Marland, “Net effect of forest harvest on CO₂ emissions to the atmosphere: a sensitivity analysis on the influence of time”, *Tellus*, 51B:314, 1999
8. G.G. Stevenson, “The Production, Distribution and Consumption of Fuelwood in Haiti”, *The Journal of Developing Areas*, 24:59, 1989.
9. C.N. Lane, ed., *Acid Rain: overview and abstracts*, Nova Science Publishers, 2003.
10. Intergovernmental Panel on Climate Change, *Climate Change 2013 – The Physical Science Basis*, Cambridge Press, 2014.
11. Environmental Protection Agency, “The Clean Air Act in a Nutshell: How It Works”, http://www.safetybok.org/the_clean_air_act_in_a_nutshell_how_it_works/, March 2013.
12. United States Geological Survey, “Byproduct Mineral Commodities Used for the Production of Photovoltaic Cells”, <http://pubs.usgs.gov/circ/1365/>, December 2010.
13. Organization of Petroleum Exporting Countries, “OPEC Statute”, http://www.opec.org/opec_web/en/publications/345.htm, January 1961.
14. S. Shafiee and E. Topal, “When will fossil fuel reserves be diminished?”, *Energy Policy*, 37:181, 2009.
15. Environmental Protection Agency, “Air Pollution Control Technology Fact Sheet: Flue Gas Desulfurization”, <http://www.epa.gov/ttnatc1/products.html>, July 2003.
16. S. Chu, “The Science of Photons to Fuel”, *AIP Conference Proceedings*, 1044:266, 2008.

17. International Energy Agency, “CO2 Emissions from Fuel Combustion Highlights 2013”, <http://www.iea.org/publications/freepublications/publication/co2-emissions-from-fuel-combustion-highlights-2013.html>, 2013.
18. World Nuclear Association, “Heat values of various fuels”, <http://www.world-nuclear.org/info/facts-and-figures/heat-values-of-various-fuels/>, March 2010.
19. World Nuclear Association “Nuclear share figures, 2004-2014”, <http://www.world-nuclear.org/info/facts-and-figures/nuclear-generation-by-country/>, May 2015.
20. International Atomic Energy Agency, “Uranium: Resources, Production and Demand”, <https://www.iaea.org/OurWork/ST/NE/NEFW/Technical-Areas/NFC/uranium-production-cycle-redbook.html>, September 2014.
21. B.L. Cohen, “Breeder reactors: A renewable energy source”, *Am. J. Phys.*, 51:1, 1983.
22. World Energy Council, “2007 Survey of Energy Resources”, http://ny.whlib.ac.cn/pdf/Survey_of_Energy_Resources_2007.pdf, 2007
23. M. Khanna, J. Scheffran and D. Zilberman, eds. *Handbook of Bioenergy Economics and Policy*, Springer, 2010.
24. C.L. Archer and M.Z. Jacobson, “Evaluation of Global Wind Power,” *Journal of Geophysical Research: Atmospheres*, 110:D12, 2005.
25. A.M. Bradshaw, T. Hamacher and U. Fischer, “Is nuclear fusion a sustainable energy form?”, *Fusion Engineering and Design*, 86:2770, 2011.
26. A.M. Gorlov *Tidal energy. In: Encyclopedia of ocean sciences*, Oxford: Academic Press; 2001.
27. IEEE Spectrum, “World’s Largest Solar Thermal Plant Syncs to the Grid”, <http://spectrum.ieee.org/energywise/energy/renewables/worlds-largest-solar-thermal-plant-syncs-to-the-grid>, September 2013.
28. M.A. Green, K. Emery, Y. Hishikawa, W. Warta and E.D. Dunlop, “Solar cell efficiency tables (version 45)”, *Progress in Photovoltaics: Research and Applications*, 23:1, 2015.

Chapter 2

1. ASTM International, “Standard Solar Constant and Zero Air Mass Solar Spectral Irradiance Tables”, http://compass.astm.org/EDIT/html_annot.cgi?E490, 2014
2. ASTM International, “Standard Tables for Reference Solar Spectral Irradiances: Direct Normal and Hemispherical on 37° Tilted Surface”, http://compass.astm.org/EDIT/html_annot.cgi?G173, 2012.
3. W Pauli, “Über den Zusammenhang des Abschlusses der Elektronengruppen im Atom mit der Komplexstruktur der Spektren” *Zeitschrift für Physik*, 31:765, 1925.
4. S. M. Sze and K. K. Ng, *Physics of Semiconductor Devices*, Wiley, 2007.

5. S. Adachi, *Properties of Semiconductor Alloys: Group-IV, III-V and II-VI Semiconductors*, Wiley, 2009.
6. P. A. M. Dirac, "Principles of Quantum Mechanics", *Proceedings of the Royal Society, Series A*, 112:661, 1926.
7. C. Kittel, *Introduction to Solid State Physics*, Wiley, 2005.
8. G. L. Bir and G. E. Pikus, *Symmetry and Strain-Induced Effects in Semiconductors*, Wiley, 1974.
9. W. Shockley, *Electrons and Holes in Semiconductors*, Van Nostrand, 1950.
10. M. A. Green, "Self-consistent optical parameters of intrinsic silicon at 300 K including temperature coefficients", *Solar Energy Materials & Solar Cells*, 92:1305, 2008.
11. S. Adachi, *The Handbook on Optical Constants of Semiconductors*, World Scientific, 2012.
12. W. Shockley, "The Theory of p-n Junctions in Semiconductors and p-n Junction Transistors", *Bell Systems Technical Journal*, 28:435, 1949.
13. J. Nelson, *The Physics of Solar Cells*, Imperial College Press, 2003.
14. S. Fonash, *Solar Cell Device Physics*, Elsevier, 2010.
15. M. A. Green, *Solar Cells: Operating Principles, Technology, and System Applications*, Prentice-Hall, 1982.
16. M.A. Green, K. Emery, Y. Hishikawa, W. Warta and E.D. Dunlop, "Solar cell efficiency tables (version 45)", *Progress in Photovoltaics: Research and Applications*, 23:1, 2015.
17. W. Shockley and H. J. Queisser, "Detailed Balance Limit of Efficiency of p-n Junction Solar Cells", *Journal of Applied Physics*, 32:510, 1961.
18. C. H. Wu and R. Williams, "Limiting Efficiencies for Multiple Energy-gap Quantum Devices", *Journal of Applied Physics*, 54:6721, 1983.
19. W. van Roosbroeck and W. Shockley, "Photon-Radiative Recombination of Electrons and Holes in Germanium", *Physical Review*, 94:1558, 1954.
20. E. Yablonovitch, O. D. Miller and S. R. Kurtz, "The opto-electronic physics that broke the efficiency limit in solar cells", *38th IEEE Photovoltaics Specialists Conference*, Austin, TX 2012.
21. H. C. Hamaker, "Computer modeling study of the effects of inhomogeneous doping and/or composition in GaAs solar-cell devices", *Journal of Applied Physics*, 58:2344, 1985.
22. E. Yablonovitch and T. J. Gmitter, "A contactless minority lifetime probe of heterostructures, surfaces, interfaces and bulk wafers", *Solid-State Electronics*, 35:261, 1992.
23. H. J. Hovel, *Semiconductors and Semimetals, vol. 2: Solar Cells*, Academic Press, 1976.

24. D. K. Schroder and D. L. Meier, "Solar Cell Contact Resistance – A Review", *IEEE Transactions on Electron Devices*, 13:637, 1984.

Chapter 3

1. M. C. Scharber and N. S. Sariciftci, "Efficiency of bulk-heterojunction organic solar cells", *Progress in Polymer Science*, 38:1929, 2013.
2. B. Mitchell, G. Peharz, G. Siefert, M. Peters, T. Gandy, J. C. Goldschmidt, J. Benick, S. W. Glunz, A. W. Bett and F. Dimroth, "Four-junction spectral beam-splitting photovoltaic receiver with high optical efficiency", *Progress in Photovoltaics: Research and Applications*, 19:61, 2010.
3. S. M. Bedair, M. F. Lamorte and J. R. Hauser, "A two-junction cascade solar-cell structure", *Applied Physics Letters*, 34:38, 1979.
4. E. A. Fitzgerald, "Dislocations in strained-layer epitaxy: theory, experiment, and applications", *Material Science Reports*, 7:87, 1991.
5. J. C. P. Chang, J. Chen, J. M. Fernandez, H. H. Wieder and K. L. Kavanagh, "Strain relaxation of compositionally graded $\text{In}_x\text{Ga}_{1-x}\text{As}$ buffer layers for modulation-doped $\text{In}_{0.3}\text{Ga}_{0.7}\text{As}/\text{In}_{0.29}\text{Al}_{0.71}\text{As}$ heterostructures", *Applied Physics Letters*, 60:1129, 1992.
6. F. Dimroth, M. Grave, P. Beutel, U. Fiedeler, C. Karcher, T. N. D. Tibbits, E. Oliva, G. Siefert, M. Schachtner, A. Wakkeli, A. W. Bett, R. Krause, M. Piccin, N. Blanc, C. Drazek, E. Guiot, B. Ghyselen, T. Salvetat, A. Tauzin, T. Signamarcheix, A. Dobrich, T. Hannappel and K. Schwarzburg, "Wafer bonded four-junction GaInP/GaA//GaInAsP/GaInAs concentrator solar cells with 44.7% efficiency", *Progress in Photovoltaics: Research and Applications*, 22:277, 2014.
7. I. Vergaftman, J. R. Moyer and L. R. Ram-Mohan, "Band parameters for III-V compound semiconductors and their alloys", *Journal of Applied Physics*, 89:5815, 2001.
8. L. Esaki, "New Phenomenon in Narrow Germanium p-n Junctions", *Physical Review*, 109:603, 1958.
9. A. Martí and G. L. Araújo, "Limiting efficiencies for photovoltaic energy conversion in multigap systems", *Solar Energy Materials and Solar Cells*, 43:203, 1996.
10. H. Cotal, C. Fetzer, J. Boisvert, G. Kinsey, R. King, P. Herbert, H. Yoon and N. Karam, "III-V multijunction solar cells for concentrating photovoltaics", *Energy and Environmental Science*, 2:174, 2009.
11. H. L. Cotal, D. R. Lillington, J. H. Ermer, R. R. King, N. H. Karam, S. R. Kurtz, D. J. Friedman, J. M. Olson, J. S. Ward, A. Duda, K. A. Emery and T. Moriarty, "Triple-junction solar cell efficiencies above 32%: the promise and challenges of their application in high-concentration-ratio PV systems", *28th IEEE Photovoltaics Specialists Conference*, Anchorage, AK, 2000.
12. R. R. King, R. A. Sherif, D. C. Law, J. T. Yen, M. Haddad, C. M. Fetzer, K. M. Edmondson, G. S. Kinsey, H. Yoon, M. Joshi, S. Mesropian, H. L. Cotal, D. D. Krut, J. H. Ermer, and N.

- H. Karam, "New horizons in III-V multijunction terrestrial concentrator cell research", *21st European Photovoltaic Solar Energy Conference and Exhibition*, Dresden, Germany, 2006.
13. J. W. Matthews and A. E. Blakeslee, "Defects in epitaxial multilayers: I. Misfit dislocations", *Journal of Crystal Growth*, 27:118, 1974.
 14. W. Guter, J. Schöne, S. P. Philipps, M. Steiner, G. Siefer, A. Wekkeli, E. Welsler, E. Oliva, A. W. Bett and F. Dimroth, "Current-matched triple-junction solar cell reaching 41.1% conversion efficiency under concentrated sunlight", *Applied Physics Letters*, 94:223504, 2009.
 15. R. R. King, A. Boca, W. Hong, X.-Q. Liu, D. Bhusari, D. Larrabee, K. M. Edmondson, D. C. Law, C. M. Fetzer, S. Mesropian, and N. H. Karam, "Band-gap-engineered architectures for high-efficiency multijunction concentrator solar cells", *24th European Photovoltaic Solar Energy Conference and Exhibition*, Hamburg, Germany, 2009.
 16. M. Wiemer, V. Sabnis and H. Yuen, "43.5% efficient lattice matched solar cells", *Proceedings of SPIE 8108, High and Low Concentrator Systems for Solar Electric Applications VI*, 810804, 2011.
 17. Fraunhofer ISE, *New world record for solar cell efficiency at 46%*, <http://www.ise.fraunhofer.de/en/press-and-media/press-releases/press-releases-2014/new-world-record-for-solar-cell-efficiency-at-46-percent>, December 2014.
 18. R. R. King, C. M. Fetzer, D. C. Law, K. M. Edmondson, H. Yoon, G. S. Kinsey, D.D. Krut, J.H. Ermer, P. Herbert, B. T. Cavicchi and N. H. Karam, "Advanced III-V multijunction cells for space", *4th World Conference on Photovoltaic Energy Conversion*, Waikoloa, HI, 2006.
 19. A. Luque and V. Andreev, *Concentrator Photovoltaics*, Springer, 2007.
 20. L. Esaki and R. Tsu, "Superlattice and Negative Differential Conductivity in Semiconductors", *IBM Journal of Research and Development*, 14:61, 1970.
 21. A. Larsson, P. A. Andrekson, S. T. Eng and A. Yariv, "Tunable Superlattice p-i-n Photodetectors: Characteristics, Theory and Applications", *IEEE Journal of Quantum Electronics*, 24:787, 1988.
 22. P. Harrison, *Quantum wells, wires and dots: theoretical and computational physics*, Wiley, 2009.
 23. T. Katsuyama, S. M. Bedair, N. C. Giles, R. P. Burns and J. F. Schetzina, "Growth and characterization of InGaAs/GaAsP strained layer superlattices", *Journal of Applied Physics*, 62:498, 1987.
 24. N. J. Eikin-Daukes, K. Keawaguchi and J. Zhang, "Strain-Balanced Criteria for Multiple Quantum Well Structures and Its Signature in X-ray Rocking Curves", *Crystal Growth & Design*, 2:287, 2002.
 25. J. Nelson, I. Ballard, K. Barnham, J. P. Connolly, J. S. Roberts and M. Pate, "Effect of quantum well location on single quantum well p-i-n photodiode dark currents", *Journal of Applied Physics*, 86:5898, 1999.

26. L. Fraas and L. Partain, eds., *Solar Cells and Their Applications*, Wiley, 2010.
27. S. M. Sze and K. K. Ng, *Physics of Semiconductor Devices*, Wiley, 2007.
28. W. Guter and A. W. Bett, "I-V Characterization of Tunnel Diodes and Multijunction Solar Cells", *IEEE Transactions on Electron Devices*, 53:2216, 2006.
29. H. Sugiura, C. Amano, A. Yamamoto and M. Yamaguchi, "Double Heterostructure GaAs Tunnel Junction for a AlGaAs/GaAs Tandem Solar Cell", *Japanese Journal of Applied Physics*, 27:269, 1988.
30. T. Takamoto, M. Yumaguchi, E. Ikeda, T. Agui, H. Kurita and M. Al-Jassim, "Mechanism of Zn and Si diffusion from a highly doped tunnel junction for InGaP/GaAs tandem solar cells", *Journal of Applied Physics*, 85:1481, 1999.
31. H. K. Kang, S.-H. Park, D. H. Jun, C. Z. Kim, K. M. Song, W. Park, C. G. Ko and H. Kim, "Te doping in the GaAs tunnel junctions for GaInP/GaAs tandem solar cells", *Semiconductor Science and Technology*, 26:075009, 2011.
32. T. F. Keuch, M. A. Tischler, P. J. Wang, G. Scilla, R. Potemski and F. Cardone, "Controlled carbon doping of GaAs by metalorganic vapor phase epitaxy", *Applied Physics Letters*, 53:1317, 1988.

Chapter 4

1. G. B. Stringfellow, *Organometallic Vapor-phase Epitaxy: Theory and Practice*, Academic Press, 1999.
2. S. Nakamura, M. Senoh, N. Iwasa and S. Nagahama, "High-Brightness InGaN Blue, Green and Yellow Light-Emitting Diodes with Quantum Well Structures", *Japanese Journal of Applied Physics*, 34:L797, 1995.
3. S. M. Bedair, M. F. Lamorte and J. R. Hauser, "A two-junction cascade solar-cell structure", *Applied Physics Letters*, 34:38, 1979.
4. L. Fu, P. Lever, K. Sears, H. H. Tan and C. Jagadish, "In_{0.5}Ga_{0.5}As/GaAs quantum dot infrared photodetectors grown by metal-organic chemical vapor deposition", *IEEE Electron Device Letters*, 26:628, 2005.
5. D. A. McQuarrie and J. D. Simon, *Physical Chemistry, A Molecular Approach*, University Science Books, 1997.
6. M. Razeghi, *The MOCVD Challenge, Volume 2*, IOP Publishing, 1995.
7. E. S. Johnson and G. E. Legg, "Critical misorientation morphology in AlGaAs and GaAs grown by atmospheric-pressure MOCVD on misoriented substrates", *Journal of Crystal Growth*, 88:53, 1988.
8. S. M. Sze and K. K. Ng, *Physics of Semiconductor Devices*, Wiley, 2007.
9. L. J. van der Pauw, "A method of measuring specific resistivity and Hall effect of discs of arbitrary shape", *Philips Research Reports*, 13:1, 1958.

10. W. H. Bragg and W. L. Bragg, "The Reflection of X-rays by Crystals", *Proceedings of the Royal Society of London, Series A*, 88:428, 1913.
11. V. Swarminathan and A. T. Macrander, *Materials Aspects of GaAs and InP Based Structures*, Prentice Hall, 1991.

Chapter 5

1. P. Harrison, *Quantum wells, wires and dots: theoretical and computational physics*, Wiley, 2009.
2. D. Park, *Introduction to the Quantum Theory*, Dover Publications, 1992.
3. B. R. Nag, *Physics of Quantum Well Devices*, Kluwer Academic Publishers, 2001.
4. C. Kittel, *Introduction to Solid State Physics*, Wiley, 1996.
5. I. Vergaftman, J. R. Moyer and L. R. Ram-Mohan, "Band parameters for III-V compound semiconductors and their alloys", *Journal of Applied Physics*, 89:5815, 2001.
6. R. de L. Kronig and W. G. Penney, "Quantum Mechanics of Electrons in Crystal Lattices", *Proceedings of the Royal Society A*, 130:499, 1931.
7. H. Asai and K. Oe, "Energy band-gap shift with elastic strain in $\text{Ga}_x\text{In}_{1-x}\text{P}$ epitaxial layers on (001) GaAs substrates", *Journal of Applied Physics*, 54:2052, 1983.
8. S. Adachi, "Material parameters of $\text{In}_{1-x}\text{Ga}_x\text{As}_y\text{P}_{1-y}$ and related binaries", *Journal of Applied Physics*, 53:8775, 1982.
9. C. G. van de Walle, "Band lineups and deformation potentials in the model-solid theory", *Physical Review B*, 39:1871, 1989.
10. P. Yuh and K. L. Wang, "Formalism of the Kronig-Penney model for superlattices of variable basis", *Physical Review B*, 38:13307, 1988.
11. O. Vallée and M. Soares, eds. *Airy Functions and applications to physics*, Imperial College Press, 2010.
12. G. Bastard, E. E. Mendez, L. L. Chang and L. Esaki, "Variational calculations on a quantum well in an electric field", *Physical Review B*, 28:3241, 1983.
13. R. People and J. C. Bean, "Calculation of critical layer thickness versus lattice mismatch for $\text{Ge}_x\text{Si}_{1-x}/\text{Si}$ strained-layer heterostructures", *Applied Physics Letters*, 47:322, 1985.
14. J. W. Matthews and A. E. Blakeslee, "Defects in epitaxial multilayers: I. Misfit dislocations", *Journal of Crystal Growth*, 27:118, 1974.
15. N. J Eikin-Daukes, K. Keawaguchi and J. Zhang, "Strain-Balanced Criteria for Multiple Quantum Well Structures and Its Signature in X-ray Rocking Curves", *Crystal Growth & Design*, 2:287, 2002.

16. S. Wei and A. Zunger, "Calculated natural band offsets of all II-VI and III-V semiconductors: Chemical trends and the role of cation d orbitals", *Applied Physics Letters*, 72:2011, 1998.

Chapter 6

1. G. C. Osbourn, "Strained-layer superlattices from lattice mismatched materials", *Journal of Applied Physics*, 53:1586, 1982.
2. H. Schneider and K. V. Klitzing, "Thermionic emission and Gaussian transport of holes in a GaAs/Al_xGa_{1-x}As multiple-quantum-well structure", *Physical Review B*, 38:6160, 1988.
3. A. M. Fox, D. A. B. Miller, G. Livescu, J. E. Cunningham, and W. Y. Jan, "Quantum well carrier sweep out: relation to electroabsorption and exciton saturation", *IEEE Journal of Quantum Electronics*, 27: 2281, 1991.
4. H. J. Hovel, *Semiconductors and Semimetals, vol. 2: Solar Cells*, Academic Press, 1976.
5. M. R. Brozel and G. E. Stillman, eds., *Properties of Gallium Arsenide, 3rd ed.* G. E. Institution of Electrical Engineers, 1996.
6. G. Bastard, *Wave mechanics applied to semiconductor heterostructures*, Wiley, 1991.
7. C. Weisbuch, R. Dingle, A. C. Gossard and W. Wiegmann, "Optical characterization of interface disorder in GaAs-Ga_{1-x}Al_xAs multi-quantum well structures", *Solid State Communications*, 38:709, 1981.
8. S. Wei and A. Zunger, "Calculated natural band offsets of all II-VI and III-V semiconductors: Chemical trends and the role of cation d orbitals", *Applied Physics Letters*, 72:2011, 1998.
9. J. Nelson, M. Paxman, K. W. J. Barnham, J. S. Roberts, and C. Button, "Steady-state carrier escape from single quantum wells", *IEEE Journal of Quantum Electronics*, 29:1460, 1993.
10. R. R. King, C. M. Fetzer, K. M. Edmondson, D. C. Law, P. C. Colter, H. L. Cotal, R. A. Sherif, H. Yoon, T. Isshiki, D. D. Krut, G. S. Kinsey, J. H. Ermer, S. Kurtz, T. Moriarty, J. Kiehl, K. Emery, W. K. Metzger, R. K. Ahrenkiel and N. H. Karam, "Metamorphic III-V Materials, Sublattice Disorder, and Multijunction Solar Cell Approaches with Over 37% Efficiency", *19th European Photovoltaic Solar Energy Conference and Exhibition*, Paris, June 2004

Chapter 7

1. I. Garcia, I Rey-Stolle, B. Galiana and C. Algora, "Analysis of tellurium as n-type dopant in GaInP:Doping, diffusion, memory effect and surfactant properties", *Journal of Crystal Growth*, 298:794, 2007.
2. J. B. Mullin, B. W. Straughn, C. M. H. Driscoll and A. F. W. Willoughby, "Lattice superdilation phenomena in doped GaAs", 47:2584, 1976.
3. T. J. de Lyon, J. M. Woodall, M. S. Goorsky and P. D. Kirchner, "Lattice contraction due to carbon doping of GaAs grown by metalorganic molecular beam epitaxy", *Applied Physics Letters*, 56:1040, 1990.

4. L. Fraas and L. Partain, eds., *Solar Cells and Their Applications*, Wiley, 2010.
5. I. Vergaftman, J. R. Moyer and L. R. Ram-Mohan, “Band parameters for III-V compound semiconductors and their alloys”, *Journal of Applied Physics*, 89:5815, 2001 (Also Ch. 3 no. 8)
6. H. Sugiura, C. Amano, A. Yamamoto and M. Yamaguchi, “Double Heterostructure GaAs Tunnel Junction for a AlGaAs/GaAs Tandem Solar Cell”, *Japanese Journal of Applied Physics*, 27:269, 1988.
7. Performance analysis of AlGaAs/GaAs tunnel junctions for ultra-high concentration photovoltaics”, *Journal of Physics D: Applied Physics*, 45:045101, 2012.
8. N. Kojima, M. Okamoto, S. J. Taylor, M. Yang, T. Takamoto, M. Yamaguchi, K. Takahashi and T. Unno, “Analysis of impurity diffusion from tunnel diodes an optimization for operation in tandem cells”, *Solar Energy Materials and Solar Cells*, 50:237, 1998.
9. T. Takamoto, E. Ikeda, H. Kurita, and M. Ohmori, “High efficiency InGaP solar cells for InGaP tandem cell application”, *Proceedings of the First World Conference on Photovoltaic Energy Conversion*, 1729, New York, 1994.
10. E. O. Kane, “Theory of Tunneling”, *Journal of Applied Physics*, 32:83, 1961.
11. J. R. Hauser, Z. Carlin and S. M. Bedair, “Modeling of tunnel junctions for high efficiency solar cells”, *Applied Physics Letters*, 97:042111, 2010.
12. A. W. Walker, O. Thériault, M. M. Wilkins, J. F. Wheeldon and K. Hinzer, “Tunnel-Junction-Limited Multijunction Solar Cell Performance Over Concentration”, *IEEE Journal of Selected Topics in Quantum Electronics*, 19:4000508, 2013.
13. M. Baudrit and C. Algora, “Tunnel Diode Modeling, Including Nonlocal Trap-Assisted Tunneling: A Focus on III-V Multijunction Solar Cell Simulation”, *IEEE Transactions on Electron Devices*, 57:2564, 2010.
14. L. Esaki, “New Phenomenon in Narrow Germanium p-n Junctions”, *Physical Review*, 109:603, 1958.
15. L. V. Keldysh, “Behavior of Non-Metallic Crystals in Strong Electric Fields”, *Soviet Physics, Journal of Experimental and Theoretical Physics*, 6:763, 1958.
16. S. S. Li, *Semiconductor Physical Electronics*, Plenum, New York, 1993.
17. H. P. D. Lanyon and R. A. Tuft, “Bandgap narrowing in heavily doped silicon”, *1978 International Electron Devices Meeting*, 24:316, 1978.
18. S. M. Sze and K. K. Ng, *Physics of Semiconductor Devices*, Wiley, 2007.
19. J. S. Blakemore, “Approximations for Fermi-Dirac integrals, especially the function $\mathcal{F}_{1/2}(\eta)$ used to describe electron density in a semiconductor”, *Solid-State Electronics*, 25:1067, 1982.

20. K. Jandieri, S. D. Baranovskii, O. Rubel, W. Stolz and F. Gebhard, "Resonant electron tunneling through defects in GaAs tunnel diodes", *Journal of Applied Physics*, 104:094506, 2008.
21. K. Jandieri, S. D. Baranovskii, O. Rubel, W. Stolz and F. Gebhard, "Resonant tunneling as a dominant transport mechanism in n-GaAs/p-GaAs tunnel diodes", *Applied Physics Letters*, 92:243504, 2008.
22. D. L. Williamson, K. Kowalchik, A. Rocher and P. Gibart, "Nature of defects in heavily Te-doped GaAs", *Revue de Physique Appliquée*, 18:475, 1983.
23. J. Gebauer, E. R. Weber, N. D. Jäger, K. Urban and Ph. Ebert, "Determination of the charge carrier compensation mechanism in Te-doped GaAs by scanning tunneling microscopy", *Applied Physics Letters*, 82:2059, 2003.
24. D. V. Lang and C. H. Henry, "Nonradiative Recombination at Deep Levels in GaAs and GaP by Lattice-Relaxation Multiphonon Emission", *Physical Review Letters*, 25:1525, 1975.
25. R. Sankaran, "Tellurium doping of vapor phase epitaxial GaAs", *Journal of Crystal Growth*, 50:859, 1980.
26. D. J. Fisher, *Diffusion in GaAs and other III-V Semiconductors*, Trans Tech Publications, 1998.
27. S. H. Lee, C. Y. Fetzer, G. B. Stringfellow, D. H. Lee and T. Y. Seong, "Te doping of GaInP: Ordering and step structure", *Journal of Applied Physics*, 85:3590, 1999.
28. R. Kúdela, J. Šoltýs, A. Vincze and J. Novák, "Tellurium delta-doped InGaP layers grown by metalorganic vapour phase epitaxy", *Physica Status Solidi – Rapid Research Letters*, 7:443, 2013.
29. J. P. Samberg, H. M. Alipour, G. K. Bradshaw, C. Z. Carlin, P. C. Colter, J. M. LeBeau, N. A. El-Masry and S. M. Bedair, "Interface properties of Ga(As,P)/(In,Ga)As strained multiple quantum well structures", *Applied Physics Letters*, 103:071605, 2013.